Hideki Ogihara

Lithium Titanate Ceramic System as Electronic and Li-ion Mixed Conductors for Cathode Matrix in Lithium-Sulfur Battery

Dissertation

BOSCH
Technik fürs Leben

Lithium Titanate Ceramic System as Electronic and Li-ion Mixed Conductors for Cathode Matrix in Lithium-Sulfur Battery

Zur Erlangung des akademischen Grades

eines

Doktors der Ingenieurwissenschaften

von der Fakultät für Maschinenbau des

Karlsruher Institut für Technologie (KIT)

genehmigte

Dissertation

Von

M. Sc. Hideki Ogihara

aus Tokyo, JAPAN

Tag der mündlichen Prüfung: 30. Mai 2012

Hauptreferent: Prof. Dr. rer. nat. M. J. Hoffmann

Mitberichter: Prof. Dr. rer. nat. H. Ehrenberg

Zusammenfassung

Lithium-Titanat-Spinell $Li_{4/3}Ti_{5/3}O_4$, Ramsdellit $Li_2Ti_3O_7$, und Spinell - Kochsalz abgeleitetes $Li_{4/3+x}Ti_{5/3}O_4$ ($0 \leq x \leq 1$) wurden untersucht, um ein gemischt-leitendes (d.h. Li-Ionen und Elektronen) keramisches Material als Kathoden-Matrix für eine Festköper-Lithium-Schwefel-Batterie zu entwickeln. Die Lithium-Ionen- und die elektronische Leitfähigkeit sollte durch Optimierung der Verarbeitungs-Atmosphäre, Dotierung von aliovalenten Ionen auf entweder Li- oder Ti- Plätzen, und Li-Insertion in Spinell $Li_{4/3}Ti_{5/3}O_4$ verbessert werden.

In beiden, Spinell $Li_{4/3}Ti_{5/3}O_4$ und Ramsdellit $Li_2Ti_3O_7$, erhöhte die Verarbeitung in kontrollierter reduzierender Atmosphäre die elektronische Leitfähigkeit deutlich. Dies ist wesentlich bewirkt durch Ti^{3+} oder/und an Sauerstoff-Leerstellen gebundene freie Elektronen, wie sie im Prozess in reduzierender Atmosphäre entstehen. Li-Insertion in Spinell $Li_{4/3}Ti_{5/3}O_4$ führte auch zu einer Zunahme der elektronischen Leitfähigkeit durch die vom eingefügten Li bewirke Bildung von Ti^{3+}.

In Bezug auf die Li-Ionen-Leitfähigkeit kann eine Dotierung von Spinell $Li_{4/3}Ti_{5/3}O_4$ und Ramsdellit $Li_2Ti_3O_7$ die Gitterkonstante wie gewünscht erhöhen, ohne aber die Li-Ionen-Leitfähigkeit zu verbessern. Es wurde qualitativ bestätigt, dass Li-Insertion in Spinell $Li_{4/3}Ti_{5/3}O_4$ die Li-Ionen-Leitfähigkeit erhöht.

Fe-dotierter Spinell $Li_{4/3}Ti_{5/3}O_4$ soll mit seinem 2-stufigen Spannungs-Verhalten bei der Li-Insertion die Lokalreaktion im Leerlaufzustand von $Li_{4/3+x}Ti_{5/3}O_4$ mit Schwefel begrenzen. Bei Li-Insertion in den Fe-dotierten Spinell $Li_{4/3}Ti_{5/3}O_4$ erhöhte sich die Gesamt-Leitfähigkeit. Die Auftrennung der Leitfähigkeit in Li-Ionen- und elektronische Beiträge würde die Optimierung von Fe-Dotierung- und Li-Insertions-Menge erlauben, um damit das gewünschte keramische Material mit ausreichender Li-Ionen- und elektronischer Leitfähigkeit für die Kathode in einer Li-S Batterie zu realisieren.

Acknowledgements

TABLE OF CONTENTS

Chapter 1: Introduction

1.1 Motivation

1.1.1 Insufficient cycle stability of lithium-sulfur battery

A lithium-sulfur (Li-S) battery has been extensively investigated as an alternative to the conventional lithium ion (Li-ion) batteries. The Li-S battery has a superior theoretical capacity to the conventional Li-ion batteries and may provide up to 600 Wh/kg on a cell level. A current Li-S battery typically consists of Li metal as an anode, a separator filled with a liquid electrolyte, and a mixture of sulfur, carbon, and a binder as a cathode. This type of cell can provide a good capacity during initial cycles, but the cycle stability of the cell is not sufficient to compete with the other conventional Li-ion batteries. One of the reasons for the insufficient cycle stability is the degradation of the cathode matrix during the cycles. Therefore a stable cathode structure needs to be developed to improve the cycle stability of the battery.

1.1.2 Lithium titanate as a framework of the stable cathode structure

The stable cathode structure in Li-S batteries may be realized with a ceramic material as a framework of the cathode matrix. Carbon and the binder in the conventional cathode are replaced by a mixed conducting (i.e. electronic and Li-ion conducting) ceramic with good structural stability filled with sulfur. A lithium titanate system was investigated in this study for the purpose. The commercial use of spinel $Li_{4/3}Ti_{5/3}O_4$ and ramsdellite $Li_2Ti_3O_7$ as an anode in some conventional Li-ion batteries implies that the lithium titanates may possess good electronic and Li-ion conductivities and good structural stability.

1.2 Objectives

The objectives of this study on the lithium titanate system are as follows:
- To increase electronic and Li-ion conductivities towards a target value to be able to implement the material in the cathode matrix of the Li-S battery.
- To acquire a better understanding of electronic and Li-ion conduction mechanisms
- To investigate whether it is possible to implement the material into the Li-S battery environment without creating any problems. If there are problems, solutions need to be addressed

Material development (i.e. bulk properties) of the ceramic for the cathode purpose is the focus of this study.

1.3 Organization of the thesis

Here, the organization of the following chapters is briefly explained.

Chapter 2 provides a background to this study. A literature review on Li-ion and Li-S batteries and the lithium titanate system, target properties, and strategies to achieve the target properties are included.

Chapter 3 reviews the details of the material processing. The experimental technique and approaches used to characterize structural and electrical properties are also described.

Chapters 4 and 5 present the experimental results and discussion on the results, respectively. The structural and electrical properties of the lithium titanate ceramics are emphasized. The chapters are divided into the structures; spinel $Li_{4/3}Ti_{5/3}O_4$, ramsdellite $Li_2Ti_3O_7$, and spinel - rock salt derived $Li_{4/3+x}Ti_{5/3}O_4$. Discussion on the relationship between these 3 compounds is also provided. The Fe doped $Li_{4/3}Ti_{5/3}O_4$ is presented as a separate section for the sake of Fe doping, which is different from the other dopants.

Chapter 6 summarizes the important findings of scientific and technological perspectives.

Chapter 2: Background

2.1 Li-ion batteries

2.1.1 Conventional Li-ion batteries

Li-ion batteries have been intensively developed over the last several decades and nowadays employed in many electric products such as laptops, cell phones, or portable power tools [Whi04][Arm08][Tar01]. Figure 2.1 is the schematic of a Li-ion battery with a current technology in industry. The anode typically consists of graphite and the cathode consists of a Li intercalation material such as $LiCoO_2$. The 2 electrodes are connected through a liquid electrolyte, typically $LiPF_6$ in nonaqueous solvents [Whi04] [Scr10].
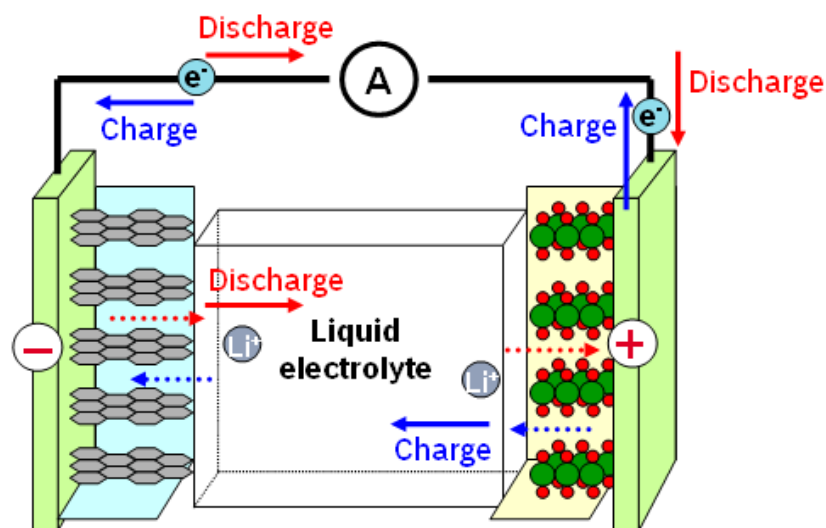
Figure 2.1. A schematic showing a typical conventional Li-ion battery [Goo07]

When the battery is discharged, a current is produced by Li-ions travelling from the anode to the cathode through the electrolyte and electrons travelling through an external circuit, which serves as electricity for electric products. In contrast, when the battery is charged, Li-ions travel from the cathode to the anode through the electrolyte and electrons through the external circuit.

These Li-ion batteries with the current technology have many advantages in terms of specific energy, energy density, and cycle stability over the other rechargeable batteries such as Ni-Cd or Ni-MH batteries [Arm08][Yos09]. However, the use of Li-ion batteries for electric vehicles has been limited [Goo11].

One of the limitations of the currently existing Li-ion batteries for the use in electric vehicles is the driving range of the electric vehicles. There already exist electric

vehicles from several auto manufactures in market (e.g. Mitsubishi i MiEV, Nissan Leaf), but the driving range is limited to 100-150 km before the battery needs to be charged [Mit11][Nis11]. The driving range of 100-150 km is not long enough for many users; the driving range is much shorter than that of gasoline based vehicles, which is > 500 km. One exception is the vehicle from Tesla, Roadster, with a driving range up to 300 km [Tes11], but the battery is too heavy and the price of the vehicle is not affordable for every consumer.

2.1.2 Li-S battery

One way to increase the driving range of electric vehicles with relatively light battery weight is to increase the specific energy of the battery; specific energy is defined by the energy which a battery of unit weight can supply. Li-S battery has been investigated intensively as a possible solution for the longer driving range [Akr04][Che03/1][Che03/2].

Figure 2.2 shows the specific energy and energy density of Li-S battery and other types of rechargeable batteries. Although the maximum specific energy which can be achieved with the currently commercial Li-ion batteries is about 200 Wh/Kg on a cell level, Li-S battery is expected to have a specific energy of up to 600 Wh/kg on a cell level. Sion Power, one of the leading companies for Li-S battery in the field, has already achieved a specific energy of 350 Wh/kg and expects to achieve a specific energy over 600 Wh/kg in the near future [Sio11].
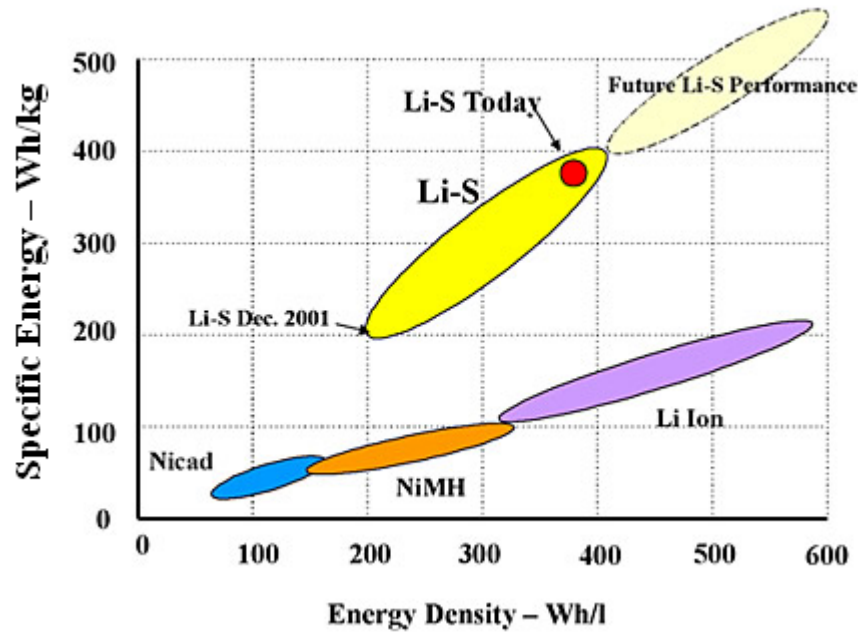
Figure 2.2. Specific energy and energy density of Li-S battery and other types of rechargeable batteries. The values are based on a cell level [Sio11]

A current standard Li-S battery consists of Li metal anode, a liquid electrolyte, and a cathode made of sulfur and carbon held together by a binder [Akr04]. Carbon is added to enhance electronic conductivity, since sulfur is electronically insulating.

When the battery is discharged, Li and S react to form Li_2S through the following reaction.

$$2Li^+ + 2e^- + \frac{1}{8}S_8 \rightleftharpoons Li_2S \qquad (2.1)$$
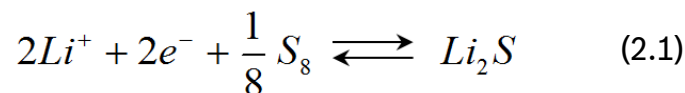
The reaction is known to occur through various polysulfides; Li_2S_8, Li_2S_6, Li_2S_4, Li_2S_3, and Li_2S_2 [Ark4].

Figure 2.3 shows a typical discharge profile of a Li-S cell. The profile can be divided into two regions; the first region with the voltage of about 2.5 down to 2.1 V and the second region with the constant voltage of about 2.1 V. It is understood in literature that the first region is involved with reaction of the polysulfides which are soluble in the electrolyte (e.g. Li_2S_4 and Li_2S_3), and the second region with the polysulfides which are insoluble in the electrolyte (i.e. Li_2S_2 and/or Li_2S) [Mik04] [Che03/1].
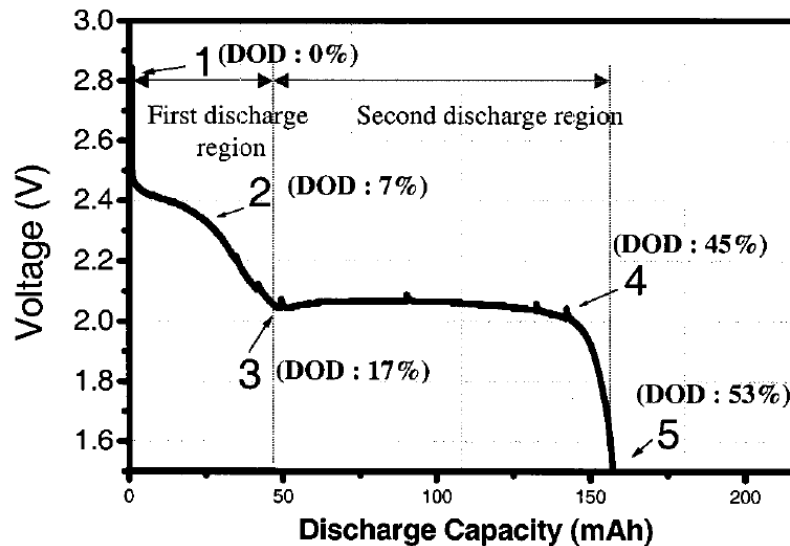
Figure 2.3. Typical discharge profile of a Li-S cell. DOD stands for depth of discharge and the values in % are against the theoretical capacity of the cathode [Che03/1]

The Li-S battery is promising for the higher specific energy, but its battery cycle stability is in doubt. The degradation in specific energy over cycles is observed [Che03/2]. To the best of the knowledge, no Li-S battery with the cycle capability of more than 500 cycles without the significant degradation in specific energy exists so far [Sio10]. The current cycle capability is not sufficient for electric vehicles which are used on a daily basis.

Here are the possible causes for the low cycle stability.

1. Li dendrites grow into the electrolyte, which may lead to a local short circuit in the battery.

2. Li polysulfides are dissolved into the liquid electrolyte. This may lead to a loss of active S from the cathode, when the shuttle mechanism is occurring [Akr04].

3. Reaction between Li metal anode and the electrolyte, which may lead to the degradation of the electrolyte.

4. Structural degradation between S/Li_2S and carbon in the cathode may occur during cycles. Unlike Li intercalation materials in the conventional Li-ion batteries, the reaction of Li with S to form Li_2S, or the reaction in the other direction, is a conversion reaction (i.e. the formation of a completely new compound). S/Li_2S expands and contracts significantly during the reactions, which may lead to a loss of contact between S/Li_2S and carbon.

2.1.3 All solid state Li-S battery

The problems with the low cycle stability in the current Li-S batteries mentioned in the previous section may be solved by realizing an all solid state Li-S battery [Eis09] [Eis10]. Figure 2.4 shows the schematic of the all solid state Li-S battery. The liquid electrolyte is replaced by a solid ceramic electrolyte, and the sulfur-carbon cathode matrix is replaced by a ceramic filled with sulfur. The ceramic in the cathode is utilized as a rigid framework for the cathode matrix.
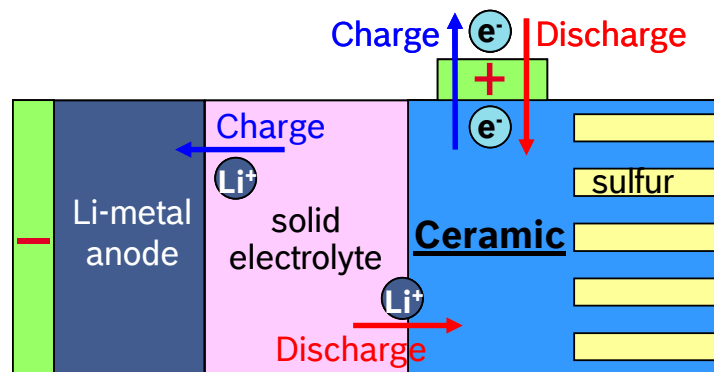
Figure 2.4. A schematic of an all solid state Li-S battery with a ceramic based cathode matrix

The solid electrolyte may solve the first 3 problems explained in the last section. The ceramic cathode structure may solve the last problem with the structural degradation in the cathode matrix during cycles. The cathode is based on a rigid hierarchically branched structure made of a mixed electronic and Li-ion conducting ceramic. The mixed conductor is required in the structure to be able to transport Li-ions from the electrolyte to sulfur and at the same time electrons from the current collector to sulfur during discharge, and to transport them in the other direction during charge. With this cathode configuration, there would be no morphology change on cycling and sulfur would stay in the same place in a controlled manner.

For the cathode matrix purpose, a ceramic material with the following properties needs to be developed.

1. High electronic conductivity with a target value of 5×10^{-2} S/cm at room temperature.

2. High Li-ion conductivity with a target value of 5×10^{-2} S/cm at room temperature.

3. High structural stability, so that there is no structural degradation during cycles.

4. If the material is electrochemically active, the electrochemical potential against Li/Li$^+$ of the material should be lower than that of sulfur. Otherwise, when Li-ion comes into the material, Li-ion would stay in the material, not being transported to sulfur.

The target value of 5 x 10^{-2} S/cm was determined based on the calculation for the specific energy of 600 Wh/kg as a cell level with rate of 2C for a specified geometry [Eis09] [Eis10]; 2C rate means that a battery is charged or discharged 2 times in 1 hour.

2.2 Electrically conducting ceramics

An electric current flows in a material when there are mobile charge carriers (e.g. electrons or ions) in the material and an electric field is applied to the material. The charge carriers are accelerated by the applied electric field, but not infinitely due to the collisions or interactions of the carriers [Mou03]. The velocity is saturated at some point with average drift velocity, V$_d$,

$$V_d = \frac{qE\tau}{m} \qquad (2.2)$$

where, q and m are a charge and a mass of the carrier, respectively, E is an applied electric field, and τ is the average relaxation time between collisions [Kin76]. A current flows in proportion to the drift velocity. The current density, J, in the material containing charge carriers with a density of n and a charge of q, is expressed by [Mou03],

$$J = nqV_d \qquad (2.3)$$

Ohm's law states,

$$J = \sigma E \qquad (2.4)$$

where σ is conductivity. By comparing the equations 2.3 and 2.4, the conductivity is given by,

$$\sigma = \frac{nqV_d}{E} \qquad (2.5)$$

Mobility, μ, can be defined as the following when the drift velocity is proportional to the applied electric field [Mou03],

$$V_d = \mu E \qquad (2.6)$$

By combining the equations 2.5 and 2.6, the conductivity is derived:

$$\sigma = nq\mu \qquad\qquad (2.7)$$

Equation 2.7 suggests that a higher carrier density and a higher mobility of charge carriers are essential for a higher conductivity. Electric conduction in ceramic materials can be either electronic or ionic, or a mixture of them in mixed conductors, which are described in detail in the following sections.

2.2.1 Electronic conduction

When electronic properties of materials are described, a simple band theory is often employed. With the band theory, electroceramic materials can be divided into 3 broad categories with respect to their electrical conduction behavior; namely, metals, semiconductors, and insulators [Mou03]. Figure 2.5 shows the difference for the conduction mechanisms with a simple electron band model.

(a)   (b)   (c)
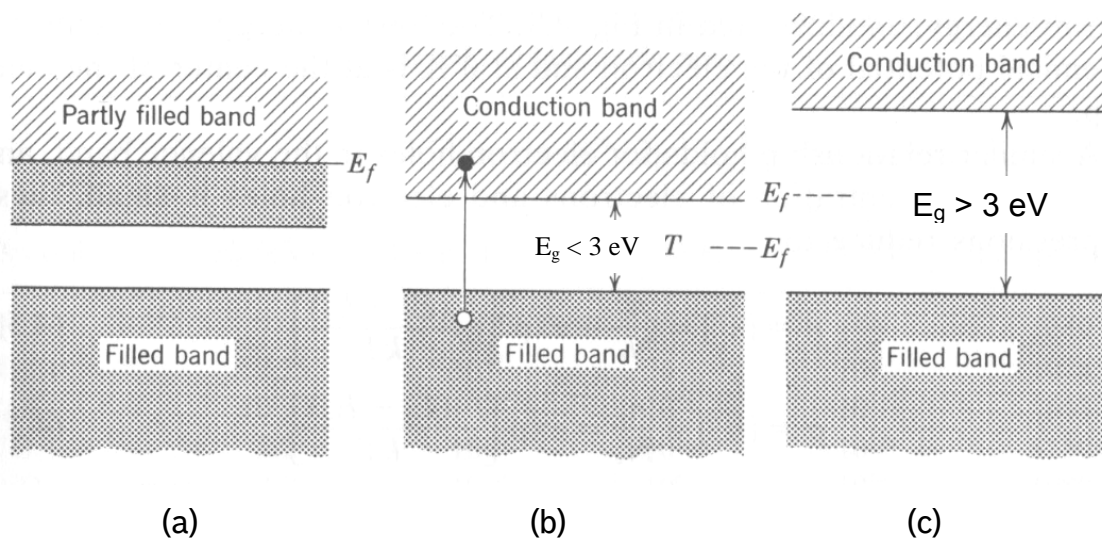
Figure 2.5. Schematic electron band structures for (a) metals, (b) semiconductors, and (c) insulators [Kin76]

In metals, an electron with the highest energy lies in a partially filled band and excited states are continuously available. The energy of the highest filled level in the ground state at 0 K is defined as the Fermi energy, E_f [Kit05]. On the other hand, semiconductors and insulators have a gap between the electron with the highest energy and the next available state. At 0 K, the valence band is completely filled, and the conduction band is empty. In this case, E_f lies between the bands and it is at $E_g/2$ for semiconductors and insulators. The energy difference between the valence and conduction bands is called the band gap. Insulators and semiconductors are

distinguished by the magnitude of the band gap, E_g. If E_g is relatively small, materials are classified as semiconductors since thermal energy tends to be large enough to excite a population of electrons from the valence band to the conduction band, as shown in Figure 2.5 (b). If E_g is relatively large, materials are called insulators since thermal energy is insufficient to promote many electrons to the conduction band [Kin76]. 2-3 eV is often used as the boundary between semiconductors and insulators, but no strict definition has been made.

The electronic conductivity in metal decreases with increasing temperature. This decrease is caused by interactions between thermally activated electrons and phonons [Mou03], which results in the decrease in the mobility of electrons, while the carrier density remains. In semiconductors or insulators, the electronic conductivity increases with increasing temperature. More and more electrons are thermally activated to the conduction band at higher temperatures. The increase in the carrier density dominates the conductivity, since the temperature dependence of the density is much more significant than that of the mobility [Mou03].

The temperature dependence on the conductivity in semiconductors or insulators is often described by Arrhenius model [Mou03]. Arrhenius model assumes that a thermally activated process governs the electronic conductivity. This yields a temperature dependent conductivity expressed by:

$$\sigma = \sigma_0 \exp(-\frac{E_a}{k_B T}) \qquad (2.8)$$

where σ is the measured conductivity, σ_0 is a temperature independent constant, E_a is the activation energy, k_B is Boltzmann's constant, and T is temperature in K. This "experimental" activation energy, E_a, is equivalent to the half of E_g [Mou03].

The band gap in semiconductors can be modified by doping aliovalent ions. n-type and p-type semiconductors refer to the material doped with the ions with a higher charge (eg. P^{5+} on Si^{4+} site) and with a lower charge than the ions in the host lattice (eg. Al^{3+} on Si^{4+} site), respectively [Mou03].

The n-type doping, for example P^{5+} on Si^{4+} site, supplies extra electrons in the material through the following defect expressed with Kröger-Vink notation (see [Krö56][Krö64] for the complete description of Kröger-Vink notation),

$$\left[P_{Si}^{\bullet}\right] = \left[e'\right] \qquad (2.9)$$

A P^{5+} ion on a Si^{4+} site creates an effectively positive charge. The effectively positive charge is compensated by an electron. This extra electron creates another energy level near the conduction band, which is called as donor states, as shown in Figure 2.6.
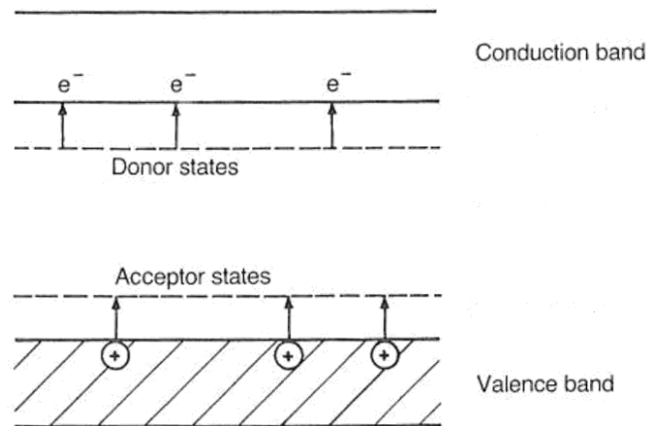
Figure 2.6. A schematic showing the change in the band structure by n- and p-type doping [Mou03]

The extra electrons in the donor states are promoted to the conduction band with much less thermal energy than intrinsic jumps from the valence to conduction band. This results in the increase in electronic conductivity at low temperatures, compared with the undoped material. This low temperature range with the conductivity increase is called "extrinsic range." At higher temperatures, the intrinsic reaction dominates the conduction and no obvious effect from the n-type doping is observed. The high temperature range is called "intrinsic range." There exists another intermediate range called "exhaustion range." At temperatures in this range, all extrinsic reactions are over (i.e. no more electrons in the donor states) but the temperature is not high enough for the intrinsic reactions. So the number of electric carrier stays same here. The slight decrease with increasing temperature is normally observed in the exhaustion range due to the decrease in mobility with increasing temperature [Sol03]

The p-type dopants (e.g. Al^{3+} on Si^{4+} site) have one less electron than the host ions, which creates holes in the material through the following defect,

$$\left[Al_{Si}' \right] = \left[h^\bullet \right] \qquad (2.10)$$

A Al^{3+} ion on a Si^{4+} site creates an effectively negative charge. The effectively negative charge is compensated by a hole. This extra hole creates another energy

level near the valence band, which is called as acceptor states, as shown in Figure 2.6. When electrons in the valence band are thermally activated to the accepter states, a partially empty valence band is introduced, resulting in the increase in conductivity.

In ceramic materials, oxygen vacancies also modify the band gap [Mou03]. Processing materials in reducing atmosphere often introduces oxygen vacancies in ceramic materials [Smy00]. For example for a metal oxide MO, where M is a metal ion,

$$M_M + O_O \xrightarrow{\quad reducing \quad atmosphere \quad} M_M + 2\,e^{'} + V_O^{\bullet\bullet} + \frac{1}{2} O_2(g) \qquad (2.11)$$
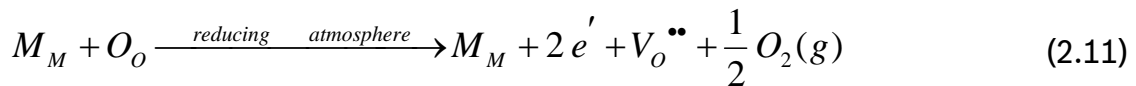
oxygen vacancies are created by oxygen leaving from the material as a gas phase. Each oxygen vacancy results in 2 extra electrons in the material to maintain electrical neutrality. Similar to the n-type doping, the extra electrons introduce another energy level in the band diagram near the conduction band and the conductivity increase in the extrinsic range is observed.

The band theory introduced in the last paragraphs is not appropriate to describe some electronic conducting materials containing multivalent ions. Electronic conductions are sometimes described well by electron hopping mechanism [Mou03] [Kin76]. Electron hopping, also called as polaron conduction, occurs between the atoms with multiple valence states, which are located on crystallographically equivalent lattice sites. Therefore, the electron hopping is often observed in the materials with transition metals. Polaron consists of electronic carrier and its polarization field [Kin76]. Mobility of electron or hole hopping from a site to another site is thermally activated, resulting in the similar Arrhenius behavior as discussed for the band conduction model.

The conductivity increases similarly with increasing temperature in the materials with the 2 different conduction mechanisms, namely the band conduction and electron hopping, except the exhaustion range for the band conduction. The mechanisms for the increase, however, are different. The distinction between the band conduction and the electron hopping is that the number of electronic carriers is thermally activated in the band conduction, whereas the mobility of electrons (or holes) is thermally activated in the electron hopping [Adl74][Kin76].

2.2.2 Ionic conduction

Electronic conduction dominates in many materials, but there are also materials in which ionic conduction dominates. Diffusion of ions in a material can be described by a simple model as shown in Figure 2.7. Ions are trapped in potential wells in solids. Potential barriers with the energy, E_m, are built at intermediate positions, since ions must squeeze through openings in the material to diffuse to other sites. For an ion to be able to diffuse, the well next to the ion needs to be empty, which costs the energy, E_D, to create the defect-site. Activation energy, E_a, for ionic conduction in a material with Schottky defect (i.e. a pair of unoccupied cation and anion sites [Kin76]) is expressed by [Nak05],

$$E_a = \frac{E_D}{2} + E_m \qquad (2.12)$$
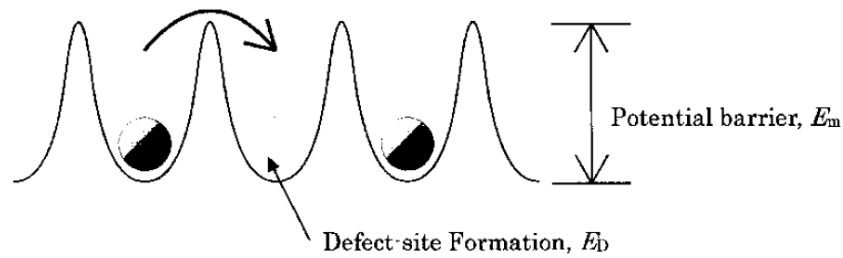
Figure 2.7. A schematic showing activation energy for ionic conduction [Nak05]

Diffusion of ions is thermally activated and expressed in the following equation; more ions have sufficient energy to overcome the potential barrier at higher temperatures [Kin76],

$$D = D_0 \, \exp(-\frac{E_a}{k_B T}) \qquad (2.13)$$

where D is the diffusion coefficient and D_0 is temperature independent constant. This diffusion coefficient is linked with the ionic conductivity, σ, through Nernst-Einstein equation [Mou03],

$$\frac{\sigma}{D} = \frac{nq}{kT} \qquad (2.14)$$

Combining equations 2.13 and 14, the following equation is obtained,

$$\sigma = \frac{B}{T} \exp(-\frac{E_a}{k_B T}) \qquad (2.15)$$

where B is temperature independent constant. Equation 2.15 looks similar to equation 2.8 for electronic conduction, but there is a distinction. The distinction is that σ in equation 2.15 for ionic conduction is proportional to $1/T \times \exp(-1/T)$, whereas σ in equation 2.8 for electronic conduction is proportional to only $\exp(-1/T)$.

In order to develop a material with high Li-ion conduction, the activation energy, E_a, needs to be minimized (Equation 2.15). Equation 2.12 implies that, for the purpose, it is important to lower the potential barrier, E_m or/and the defect formation energy, E_D. Often in materials with high ionic conduction, the defects formation energy is minimized by extrinsic defects, for example by doping [Nak05]. The potential barrier would be minimized when there is large open space for ions to move and the ions are not strongly bounded to their lattice.

2.2.3 Mixed conductors

There are materials classified as mixed conductors, which are good electronic conductors as well as good ionic conductors. Transference number is often employed to describe the contribution of each electric carrier to the total electric conduction [Hug02]. For a simple case with electrons and one type of ions, the transference numbers for ionic conduction, t_i, and for electronic conduction, t_e, are expressed as,

$$t_i = \frac{i_i}{i_i + i_e} \qquad (2.16)$$

$$t_e = \frac{i_e}{i_i + i_e} \qquad (2.17)$$

where, i_i and i_e are the partial currents for the ions and electrons, respectively. For the purpose in this study, the desired transference number is 0.5 for both electronic and Li-ion conductions.

2.3 Lithium titanates

2.3.1 Phases in a lithium titanate system

Figure 2.8 is the phase diagram of $Li_2O\text{-}TiO_2$ system. There are 4 binary compounds in the system, namely Li_4TiO_4, Li_2TiO_3, $Li_{4/3}Ti_{5/3}O_4$, and $Li_2Ti_3O_7$ [Izq80]. $Li_{4/3}Ti_{5/3}O_4$ and $Li_2Ti_3O_7$ were focused in this study, since Li_4TiO_4 and Li_2TiO_3 have been reported to be poor Li-ion conductors [Vit02][Vij09][Dis95].
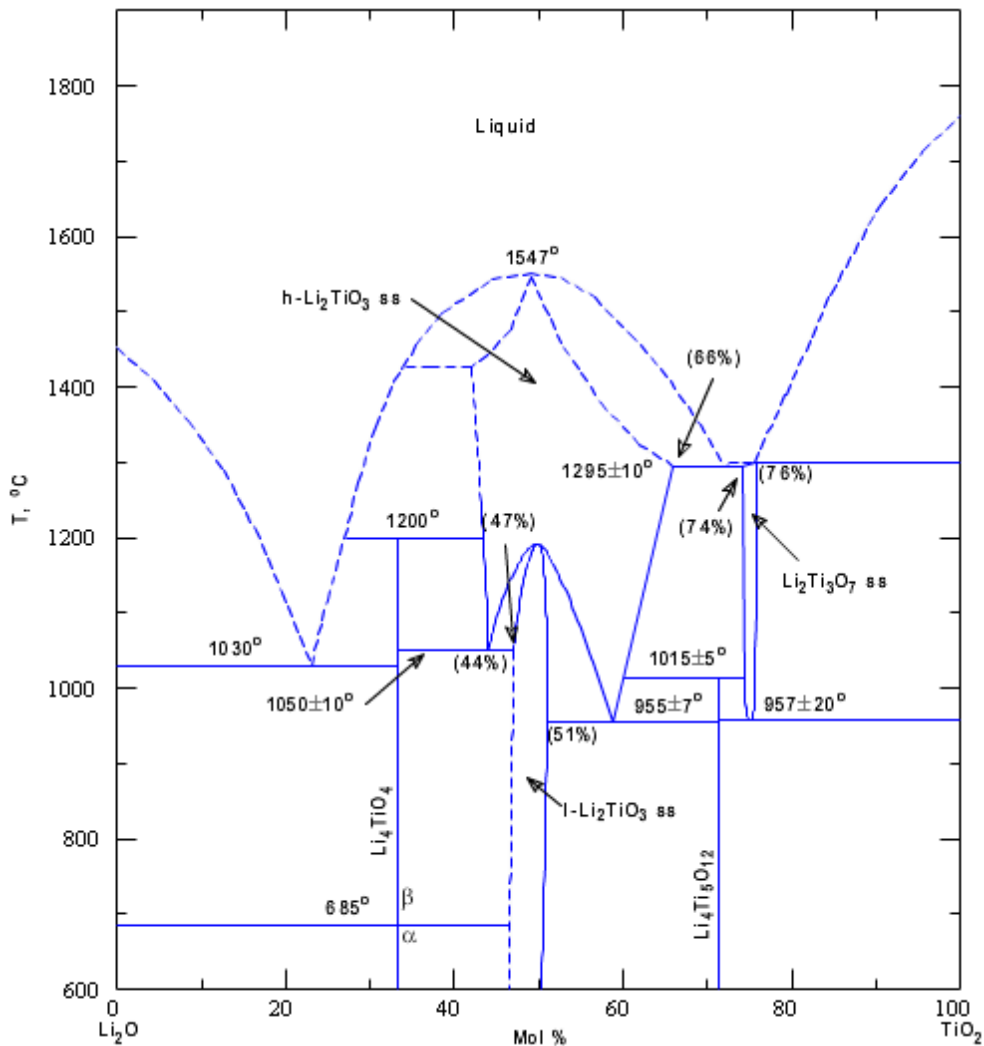
Figure 2.8. Phase diagram of $Li_2O\text{-}TiO_2$ [Izq80]

Spinel $Li_{4/3}Ti_{5/3}O_4$ has been used as an anode material for Li-ion batteries in industry [Kos08], which suggests that the material may be suitable for the stable cathode structure in the Li-S battery. Ramsdellite $Li_2Ti_3O_7$ has been less studied in literature than the spinel $Li_{4/3}Ti_{5/3}O_4$, but also investigated as an electrode material for Li-ion batteries [Arr97][Gov97]. Ramsdellite $Li_2Ti_3O_7$ possesses tunnels filled only with Li ions (described in detail in section 2.3.3), which may be an optimal conduction

_____

path for higher Li-ion conductivity. The two phases are close in composition, but their structures and electronic properties are significantly different. These two phases, spinel $Li_{4/3}Ti_{5/3}O_4$ and ramsdellite $Li_2Ti_3O_7$, have been intensively investigated in this study.

Figure 2.8 is a binary phase diagram of Li_2O and TiO_2, where all Ti ions have valencies of 4^+. It has been shown in literature that it is also possible to prepare lithium titanate compounds with Ti^{3+} ions [Gov98][Ste93][Joh76]. Figure 2.9 is a ternary diagram of Li_2O, TiO_2, and Ti_2O_3. Li can be inserted into spinel $Li_{4/3}Ti_{5/3}O_4$ and ramsdellite $Li_2Ti_3O_7$ up to $Li_{7/3}Ti_{5/3}O_4$ and $Li_{4.24}Ti_3O_7$, respectively [Sch99][Arr97]. $Li_{1+x}Ti_2O_4$ ($0 \le x \le 1$) may be a good Li-ion conductor, but $Li_{4/3+x}Ti_{5/3}O_4$ ($0 \le x \le 1$) contains more Li atoms, which may improve Li-ion conductivity further. Therefore, Li insertion into spinel $Li_{4/3}Ti_{5/3}O_4$ was investigated in this study.   Li insertion into ramsdellite $Li_2Ti_3O_7$ is also of interest, but no investigation was conducted.
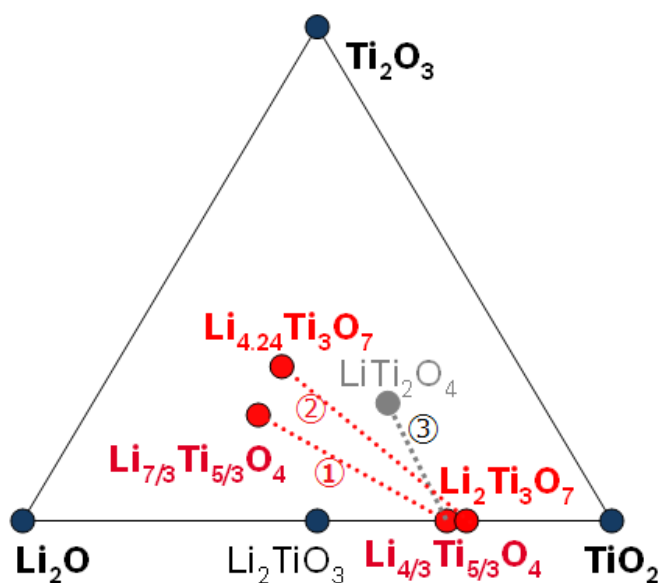
Figure 2.9. Compositional relationships of Li_2O - TiO_2 - Ti_2O_3. The red dotted lines, line 1 and 2, are for Li insertion into spinel $Li_{4/3}Ti_{5/3}O_4$ and ramsdellite $Li_2Ti_3O_7$, respectively. The gray dotted line, line 3, is for the compositions with different ratios of Li and Ti while keeping the spinel structure

Thus, the structures which were investigated in this study:
- $Li_{4/3}Ti_{5/3}O_4$
- $Li_{4/3+x}Ti_{5/3}O_4$ ($0 \le x \le 1$)
- $Li_2Ti_3O_7$

2.3.2 Lithium titanate spinel $Li_{4/3}Ti_{5/3}O_4$

Spinel refers to the mineral with the chemical formula, $MgAl_2O_4$. General chemical formula of oxides with spinel structure is AB_2O_4 [Sic99]. $Li_{4/3}Ti_{5/3}O_4$ can be written as $Li(Li_{1/6}Ti_{5/6})_2O_4$ in the general spinel formula. Figure 2.10 shows schematics of spinel $Li_{4/3}Ti_{5/3}O_4$. 75% of Li ions are tetrahedrally coordinated to oxygen and 25 % of Li ions and all of Ti ions are octahedrally coordinated to oxygen. The tetrahedra and the octahedra are arranged alternatively, which results in a cubic structure. The structure belongs to a space group of Fd-3m with the lattice parameter a = 8.35950 Å [Sch99].

(a)   (b)

● Tetrahedrally coordinated Li
● Octahedrally coordinated Ti and Li
● ○ O
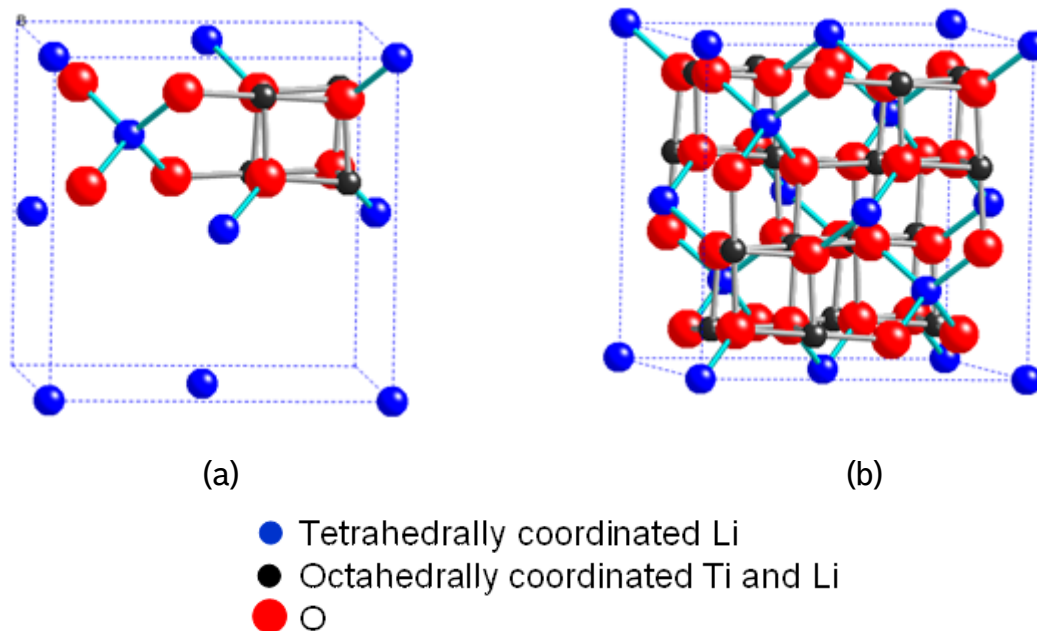
Figure 2.10. Schematics of spinel $Li_{4/3}Ti_{5/3}O_4$ showing (a) only one tetrahedral block and one octahedral block (b) one complete conventional cubic unit cell

Spinel $Li_{4/3}Ti_{5/3}O_4$ is an electronical insulator with electronic conductivity, $\sigma_{electronic}$ < 10^{-9} S/cm at room temperature [Che01][Wol08]. Mg doping has been shown to be effective to increase electronic conductivity up to 10^{-2} S/cm [Che01]. Also, other doping elements such as Cr and V increased rate capability which may indicate that electronic conductivity increases with the doping [Yi10]. At the same time, processing the material in reducing atmosphere without doping also resulted in better electronic conductivity up to 10^{-5} S/cm [Wol06]. It is not clear in literature if the doping or processing in reducing atmosphere contributes to increase electronic conductivity.

Spinel $Li_{4/3}Ti_{5/3}O_4$ possesses Li-ion conductivity of ~ 10^{-7} S/cm [Wol08][Hua04]. Li-ion conductivity is not as high as the target value of 5 x 10^{-2} S/cm. Improving Li-ion conductivity is essential for this material to be useful for the purpose in the Li-S battery.

2.3.3 Lithium titanate ramsdellite $Li_2Ti_3O_7$

Ramsdellite refers to the mineral γ-MnO_2 [Mor79]. Ramsdellite $Li_2Ti_3O_7$ can be written as $Li_{2.29}Ti_{3.43}O_8$, which represents a unit cell. The structure belongs to a space group of Pbnm with lattice parameters; a = 5.016, b = 9.543, and c = 2.945 Å [Mor79]. Figure 2.11 shows schematics of ramsdellite $Li_2Ti_3O_7$. There is a framework consisting of octahedra and spaces between them. The configuration of cations in the structure has been proposed in two different ways. One possibility is $(Li_{1.72})_c(Ti_{3.43}Li_{0.57})_fO_8$, where all titanium ions and 25% of lithium ions are octahedrally coordinated to oxygen, and the remaining lithium ions are distributed between these octahedra; f and c refer to framework and channel, respectively [Arr97]. The other is $(Li_{2.29})_c(Ti_{3.43}Vacancy_{0.57})_fO_8$, where all titanium ions are octahedrally coordinated to oxygen and all Li ions are distributed between the octahedra including cation vacancies. The former has been accepted by majority in literature, but the latter has been recently suggested as a correct configuration from diffraction and spectroscopic study [Ore09]. In either case, the octahedra are connected through edge and corner sharing in the way that a channel filled with Li-ions is formed along c-axis. The Li channels along c axis may be ideal paths for high Li-ion conduction.

(a)   (b)

● Octahedrally coordinated Ti (possibly also Li)
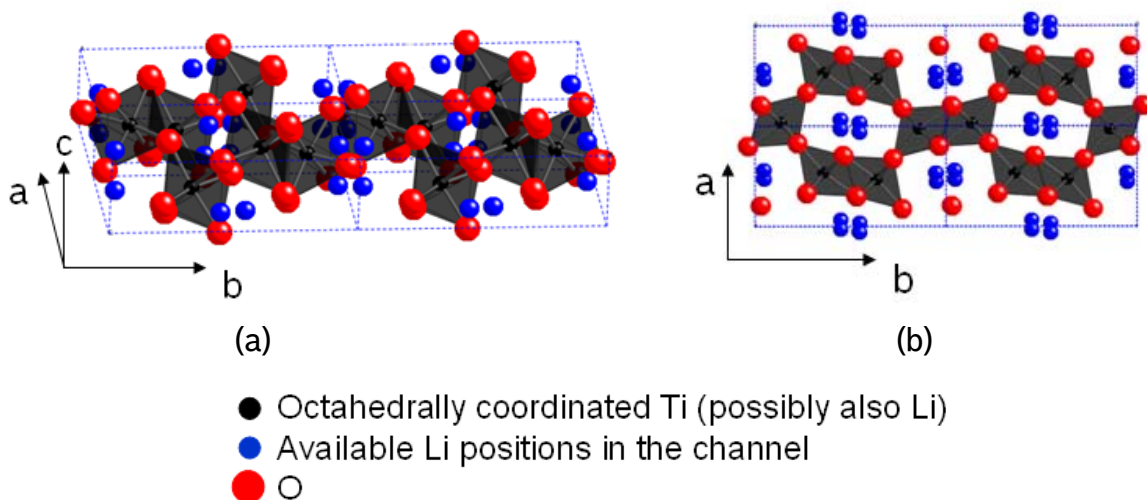● Available Li positions in the channel
● O

Figure 2.11. Schematics of ramsdellite unit cells. (a) 3-D view (b) top view along c-axis. Each unit cell is divided by dash lines

Li can be inserted into ramsdellite $Li_2Ti_3O_7$ up to x =2.24 for $Li_{2+x}Ti_3O_7$ [Arr97]. It has been reported that during the Li insertion and extraction (i.e. $Li_{2+x}Ti_3O_7$ with $0 \leq x \leq 2.24$), the volume change of the material is less than 2% [Arr00], and that electrochemical potential against Li/Li^+ during the Li insertion is about 1.5-2V [Arr97]. These properties in ramsdellite $Li_2Ti_3O_7$ satisfies 2 of the requirements for the cathode matrix purpose in the Li-S battery.

Ramsdellite $Li_2Ti_3O_7$ is an electronical insulator [Boy79], but doping or processing in reducing atmosphere may result in a better electronic conductivity, as observed in spinel $Li_{4/3}Ti_{5/3}O_4$. Ramsdellite $Li_2Ti_3O_7$ exhibits Li-ion conductivity of 1×10^{-6} S/cm as polycrystalline at room temperature [Boy79]. The conductivity is not so close to the target value of 5×10^{-2} S/cm, but higher than that in spinel $Li_{4/3}Ti_{5/3}O_4$. Moreover, the Li channel along c-axis may lead to a good Li-ion conduction. Therefore, ramsdellite $Li_2Ti_3O_7$ was also intensively investigated.

2.3.4 Lithium titanate spinel - rock salt derived $Li_{4/3+x}Ti_{5/3}O_4$ $(0 \leq x \leq 1)$

As shown in the ternary diagram (Figure 2.9), Li insertion into spinel $Li_{4/3}Ti_{5/3}O_4$ leads to the structural change to rock salt derived $Li_{7/3}Ti_{5/3}O_4$. Figure 2.12 is a schematic of rock salt derived structure with spinel structure for a comparison. The structural change is associated with the change in Li-ion coordination. Li-ions with tetrahedral coordination in spinel $Li_{4/3}Ti_{5/3}O_4$ change to have octahedral coordination during the insertion to accommodate the extra Li. The rock salt derived structure belongs to a space group of Fd-3m with lattice parameter a = 8.3538 Å [Sch99]. The structure resembles rock salt structure in the sense that all cations are octahedrally coordinated and anions are almost closely packed, but the structure belongs to the same space group as spinel $Li_{4/3}Ti_{5/3}O_4$. Therefore the structure has been named as "rock salt derived" [Köh09].

<center>(a)   (b)</center>

● Tetrahedrally coordinated Li in spinel $Li_{4/3}Ti_{5/3}O_4$
● Octahedrally coordinated Li in rocksalt derived $Li_{7/3}Ti_{5/3}O_4$
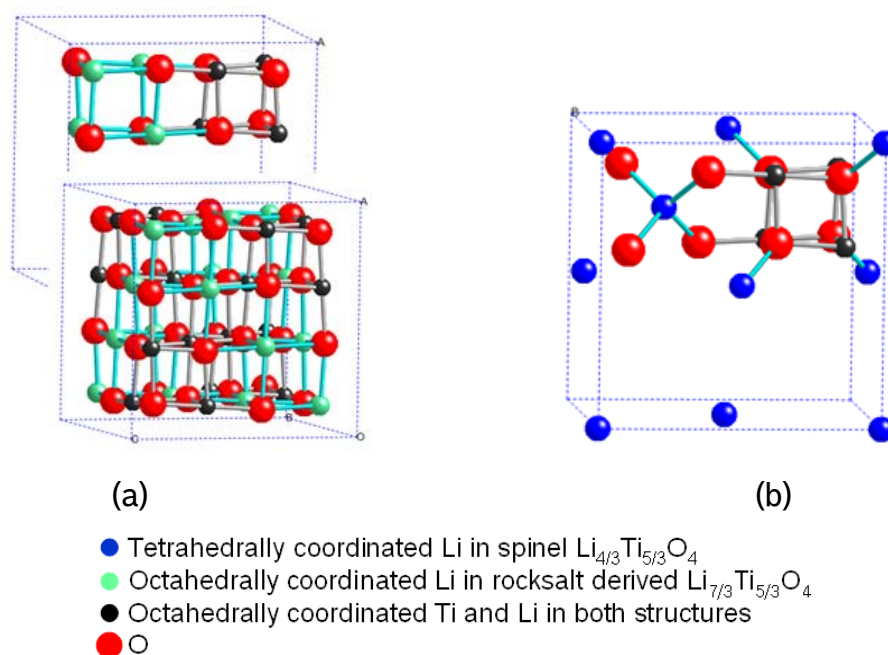● Octahedrally coordinated Ti and Li in both structures
● O

Figure 2.12.   schematics of (a) rock salt derived $Li_{7/3}Ti_{5/3}O_4$ with (b) one tetrahedral block and one octahedral block in spinel $Li_{4/3}Ti_{5/3}O_4$ for comparison

The change in volume during the Li insertion from spinel $Li_{4/3}Ti_{5/3}O_4$ to rock salt derived $Li_{7/3}Ti_{5/3}O_4$ is extremely small, < 0.5 % [Ohz95][Sch99]. This small change in the structure makes this $Li_{4/3+x}Ti_{5/3}O_4$ attractive as an electrode material in Li-ion batteries for higher cycle stability. The feature would be ideal for the stable cathode structure in the Li-S battery. The Li insertion into spinel $Li_{4/3}Ti_{5/3}O_4$ is associated with a flat voltage profile at ~ 1.5 V vs. Li/Li^+ [Sch99]. The flat voltage profile suggests that the Li insertion proceeds through the 2 phases, spinel $Li_{4/3}Ti_{5/3}O_4$ and rock salt derived $Li_{7/3}Ti_{5/3}O_4$ [Sch99]. When Li is inserted into spinel $Li_{4/3}Ti_{5/3}O_4$, there are less and less spinel $Li_{4/3}Ti_{5/3}O_4$ phase and more and more rock salt derived $Li_{7/3}Ti_{5/3}O_4$ phase, until all phase becomes rock salt derived $Li_{7/3}Ti_{5/3}O_4$ phase with complete Li insertion of 1 Li atom into spinel $Li_{4/3}Ti_{5/3}O_4$. However, it is also suggested by a diffraction study that the single phase, $Li_{4/3+x}Ti_{5/3}O_4$ is stable at room temperature [Wag06]. The clear segregation into the 2 phases can be observed only below 100 K. It is concluded that the 2 phases are metastable at room temperature and induced kinetically by a fast Li insertion [Wag06].

This Li insertion into spinel $Li_{4/3}Ti_{5/3}O_4$ may increase Li-ion conductivity. Lithium nuclear magnetic resonance (Li-NMR) study by Wilkening shows that a jump rate increases in 5 orders of magnitude with Li insertion of ~0.6 Li into spinel $Li_{4/3}Ti_{5/3}O_4$ [Wil07/1][Wil07/2]. Li-NMR detects local movement of Li-ions, which may or may not

be related to Li-ion conduction. When Li-ion moves back and forth between 2 local sites, the jump rate can be high, but these local jumps do not contribute to Li-ion conductivity. For Li-ion conduction, Li-ions must be transported macroscopically in the material.   Li-ion conductivity is proportional to the jump rate only when the Li-ion movement is macroscopic. It should also be noted that the measurement techniques employed for the measurement on the 2 samples were different; ^{7}Li spin-alignment echo NMR for spinel $Li_{4/3}Ti_{5/3}O_4$ and ^{7}Li spin-lattice relaxation NMR for Li inserted $Li_{4/3+0.6}Ti_{5/3}O_4$ [Wil07/1][Wil07/2]. The 2 numbers, therefore, may not correspond to each other exactly. With the assumption that the 2 numbers are comparable and the jump rate was proportional to Li-ion conductivity, Li-ion conductivity for the Li inserted sample can be estimated as ~ 10^{-2} S/cm, which is close to the target value. This Li insertion into spinel $Li_{4/3}Ti_{5/3}O_4$ was investigated to confirm if the increase in the jump rate with Li insertion reported by the Li-NMR study also leads the increase in Li-ion conductivity or not. Also, the change in electronic conductivity with the Li insertion was studied.

2.4 Strategies to improve electronic and Li-ion conductivities

The material to be developed in this study needs to satisfy the 4 requirements (see section 2.1.3).   With spinel $Li_{4/3}Ti_{5/3}O_4$, ramsdellite $Li_2Ti_3O_7$, and rock salt derived $Li_{7/3}Ti_{5/3}O_4$, the structural stability and the electrochemical potential of the materials would meet the requirements. Now the challenge is to improve electronic and Li-ion conductivities towards the target value of 5 x 10^{-2} S/cm.

The followings are the strategies how to improve conductivities in spinel $Li_{4/3}Ti_{5/3}O_4$ and ramsdellite $Li_2Ti_3O_7$.

- To increase electronic conductivity, introduce Ti^{3+} for Ti^{3+}/Ti^{4+} mixed valance states.

- To increase Li-ion conductivity, expand lattice spacing to create larger spaces for Li-ions to be transported in the structure.

Both may be achieved by,

1. Processing materials in reducing atmosphere:

In reducing atmosphere, Ti^{3+} ions may be introduced through oxygen vacancies. Introduction of Ti^{3+} ions may also lead to the lattice expansion since the ionic radius of Ti^{3+} ions is bigger than that of Ti^{4+} ions; the ionic radii for Ti^{3+} and Ti^{4+} ions in octahedral coordination are 0.67 and 0.605 Å, respectively [Sha76]. To confirm this

assumption, processing materials in air or combinations of H_2 and Ar atmosphere was tested.

2. Doping aliovalent ions on either Li or Ti site

The extra electron introduced by the dopant (e.g. Mg^{2+} for Li^{1+} or Nb^{5+} for Ti^{4+}) may be compensated by the change in valency of Ti ions from 4^+ to 3^+. Larger ionic radii of dopants and the introduction of Ti^{3+} may lead to the lattice expansion. To confirm this assumption, Mg^{2+}, Cu^{2+}, Ca^{2+}, Nb^{5+}, Ta^{5+}, and Zr^{4+} were doped.

Another way which may improve the conductivities is to insert Li into spinel $Li_{4/3}Ti_{5/3}O_4$ towards rock salt derived $Li_{7/3}Ti_{5/3}O_4$. To confirm this, Li insertion into undoped spinel $Li_{4/3}Ti_{5/3}O_4$ was tested.

2.5 Fe doped spinel $Li_{4/3}Ti_{5/3}O_4$: A solution to the self discharge problem

When the $Li_{4/3+x}Ti_{5/3}O_4$ (x > 0) ceramic is assumed to possess the properties required for the cathode matrix purpose in the Li-S battery by the Li insertion and the material is employed for the purpose, there is a problem during an open circuit with this $Li_{4/3+x}Ti_{5/3}O_4$ ceramic cathode matrix: The S cathode with the $Li_{4/3+x}Ti_{5/3}O_4$ (x > 0) would suffer from self discharge,

$$Li_{4/3+x}Ti_{5/3}O_4 + 0.5x \ S \rightarrow Li_{4/3}Ti_{5/3}O_4 + 0.5x \ Li_2S \qquad (2.18)$$
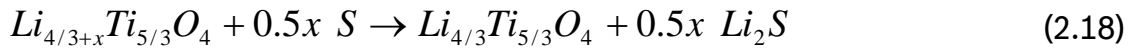
This reaction occurs since the electrochemical potential against Li/Li^+ of sulfur (~ 2.1 V for the solid reaction range) [Che03/1] is higher than that of $Li_{4/3+x}Ti_{5/3}O_4$ (~ 1.5 V) [Sch99]. The self discharge within the cathode leads to a loss of capacity and significantly inferior battery performance due to the spinel $Li_{4/3}Ti_{5/3}O_4$ phase possessing lower electrical conductivities.

Fe doped spinel $Li_{4/3}Ti_{5/3}O_4$ may solve the problem [Ogi12]. The Fe doped spinel $Li_{4/3}Ti_{5/3}O_4$ has been studied intensively by Scharner [Sch97/1][Sch97/2]. Figure 2.13 shows the phase diagram of $Li_{4/3-y/3}Fe_yTi_{5/3-2y/3}O_4$ (0 ≤ y ≤ 2.5). Depending on the Fe amount, the structures belong to either a space group of Fd-3m or $P4_332$. Fd-3m is the spinel structure as explained in section 2.3.2. The structure with $P4_332$ is distinct from Fd-3m in terms of the ordering of the ions in the octahedral sites; the octahedrally coordinated ions are disordered in spinel Fd-3m and ordered in $P4_332$. The ordered octahedrally coordinated ions lower the symmetry of the structure further from Fd-3m.
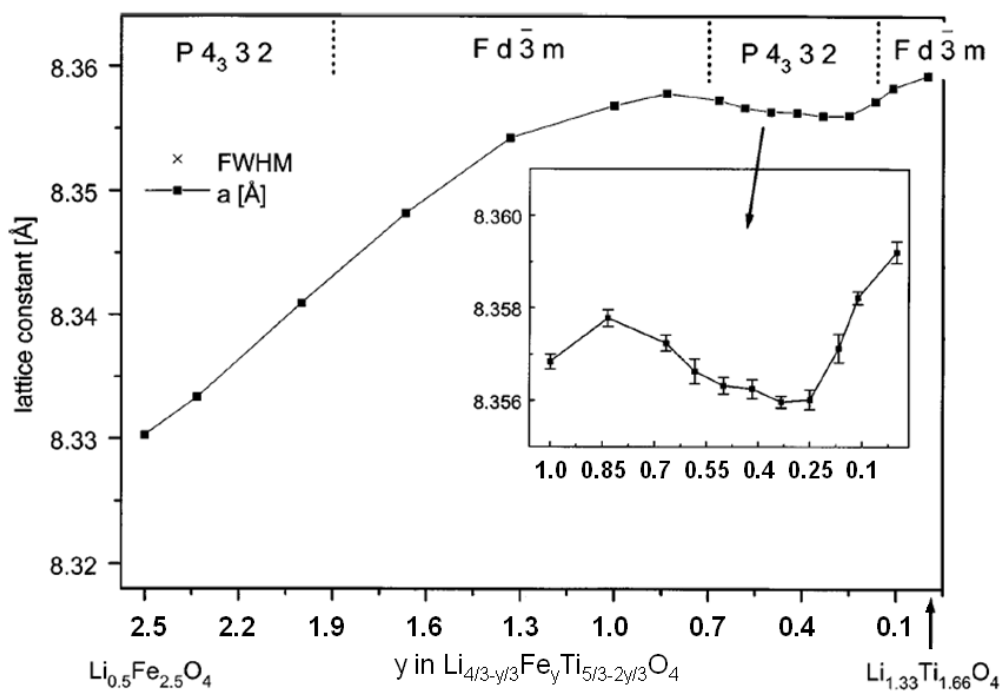
Figure 2.13. Phase diagram of $Li_{4/3-y/3}Fe_yTi_{5/3-2y/3}O_4$ ($0 \leq y \leq 2.5$) [Sch97]. x axis is rescaled for the chemical formula described in this study.

A two step voltage behavior, ~2.3 V (for $x < x_c$) and 1.5 V (for $x > x_c$) against Li/Li^+, is observed during Li insertion into the Fe doped $Li_{4/3}Ti_{5/3}O_4$ [Sch97/1]. Figure 2.14 is one example for the material, $y = 0.16$ for $Li_{4/3-y/3}Fe_yTi_{5/3-2y/3}O_4$. In this case, x_c is observed at $x \sim 0.15$-0.20, but x_c changes with the amount of Fe, y. It is understood that the higher voltage range corresponds to the change from Fe^{3+} to Fe^{2+} and the range with ~1.5 V corresponds to the change from Ti^{4+} to Ti^{3+} [Sch97/1]. If this assignment is correct, $x_c = y$ should also be true. For compositions in the 2,3 V range, no self-discharge according to equation 2.18 would occur since the potential for the formation of Li_2S is only 2,0 V. All further inserted Li from the anode would react with S to form Li_2S. In this way the cathode matrix composition is stabilized at $x=x_c$.
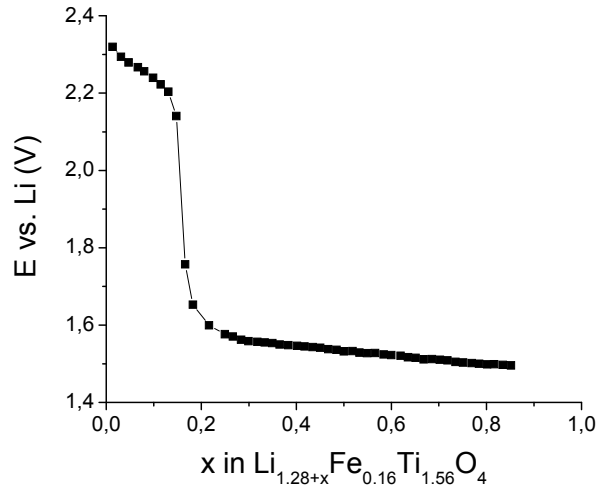
Figure 2.14. Voltage profile for the Li insertion into the Fe doped sample with y = 0.16 for $Li_{4/3-y/3}Fe_yTi_{5/3-2y/3}O_4$ [Sch97/1]

Interestingly, the Li-ion diffusivity is at its maximum around $x = x_c$ as shown in Figure 2.15 [Sch97/1]. Thereby, the Fe doped $Li_{4/3+x}Ti_{5/3}O_4$ may guarantee electrochemical stability and best rate performance due to the stable $Li_{4/3+x}Ti_{5/3}O_4$ with $x = x_c$, which provides the high Li-ion conductivity during Li-S battery operation. Electronic conductivity at the composition $x = x_c$ is not known in literature. It is interesting to confirm how electronic conductivity changes with Li insertion into the Fe doped spinel $Li_{4/3}Ti_{5/3}O_4$.
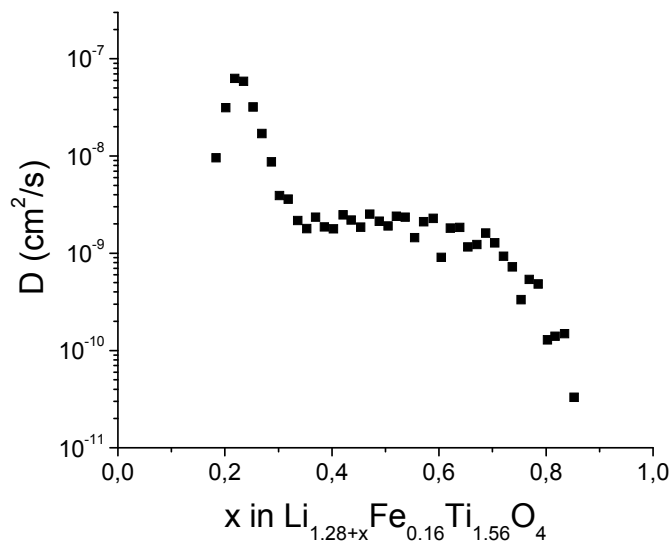

Figure 2.15. Li-ion Diffusivity as a function of the amount of Li insertion, x, into the Fe doped sample with y = 0.16 for $Li_{4/3-y/3}Fe_yTi_{5/3-2y/3}O_4$ [Sch97/1]

Chapter 3: Experimental procedure

3.1 Sample preparation

Ceramic samples were prepared by conventional solid state ceramic processing. Powders were batched to the required stoichiometries and were then milled and heat treated to form the desired phases. The powders were formed into solid, dense, polycrystalline materials; pellet pressing was employed to prepare green ceramic bodies, followed by sintering. Li insertion into the powder or pellets was performed either electrochemically in Swagelok® cells or chemically in butyllithium or by direct contact with Li metal foil.

3.1.1 Ceramic process

3.1.1.1 Powder preparation

Lithium titanate powder was prepared from reagent grade powders of lithium carbonate (Li_2CO_3, 99.0%, Alfa Aesar) and titanium oxide (TiO_2, 99.0%, Tronox). For compositions with dopants Mg, Cu, Nb, Ta, Zr, and Fe, magnesium oxide (MgO, 99.0%, E.H.Tilge), cupper oxide (CuO, 99.7%, Alfa Aesar), niobium pentoxide (Nb_2O_5, 99.9%, HC Stark), tantalum pentoxide (Ta_2O_5, 99.9%, HC Stark), zirconium oxide (ZrO_2, 97%, 2% HfO_2, Saint-Gobain), iron oxide (Fe_2O_3, 99.0%, Merck) were employed.

Figure 3.1 is the flow chart for the powder preparation. Raw materials were batched for the desired composition stoichiometrically, and mixed in isopropanol with the amount of 50 vol% of the powder batch. 3 wt% excess Li_2CO_3 was added to compensate Li loss during heat treatment. The solution was then planetary ball milled with stabilized zirconia media (spherical with 3 mm diameter, Tosoh) for 2 hours with 150 rpm (Retsch PM400). After drying the suspension by rotary evaporator at 70 ^{o}C, the powder mixture was calcined either in air or in the mixture of 10 vol% H_2 and 90 vol% Ar for 10 hours at 800 ^{o}C. The estimated P_{O2} for the calcination process in reducing atmosphere was 10^{-15} atm. The change in color of the sample was observed during calcination. Figure 3.2 shows the powder before and after calcination. The powder before calcination was white, but grey for the Cu doped sample and reddish for the Fe doped sample. The white powder did not change the color, but the Cu doped and Fe doped sample changed to brownish color during calcination in air. All the powder processed in reducing atmosphere turned into blue.

After checking for the formation of the desired phase by using X-ray diffraction (see Section 3.2 for measurement conditions), the powder calcined in air was again planetary ball milled with the media and dried as described. This time, the milling was for 5 hours with 250 rpm to crush agglomerates from the calcination process into finer powders. After drying, the powder was sieved through a mesh screen with 180 μm openings. The powder calcined in reducing atmosphere was not planetary ball milled, since isopropanol reacted with the powder and the powder became whiter. Instead, the powder calcined in reducing atmosphere was milled by hand.

Batch raw materials stoichiometrically
with 3 wt% excess Li_2CO_3:
Raw materials: Li_2CO_3, TiO_2
(For doping, MgO, CuO, CaO, Nb_2O_5, Ta_2O_5, ZrO_2, Fe_2O_3)

50 vol% of isopropanol

Planetary ball mill for 2 hr with 150 rpm

Dry with rotary evaporator at 70 ^{o}C

Grind powder by hand

Calcine in air

Calcine in
10% H2 90% Ar

X-ray diffraction
for phase
determination

50 vol% of
isopropanol

Planetary ball mill for 5 hr
with 250 rpm and dried

Grind powder
by hand

**In air or
10% H$_2$ 90% Ar**

Calcination profile

Figure 3.1. Flow chart for the powder preparation with the profile for calcination
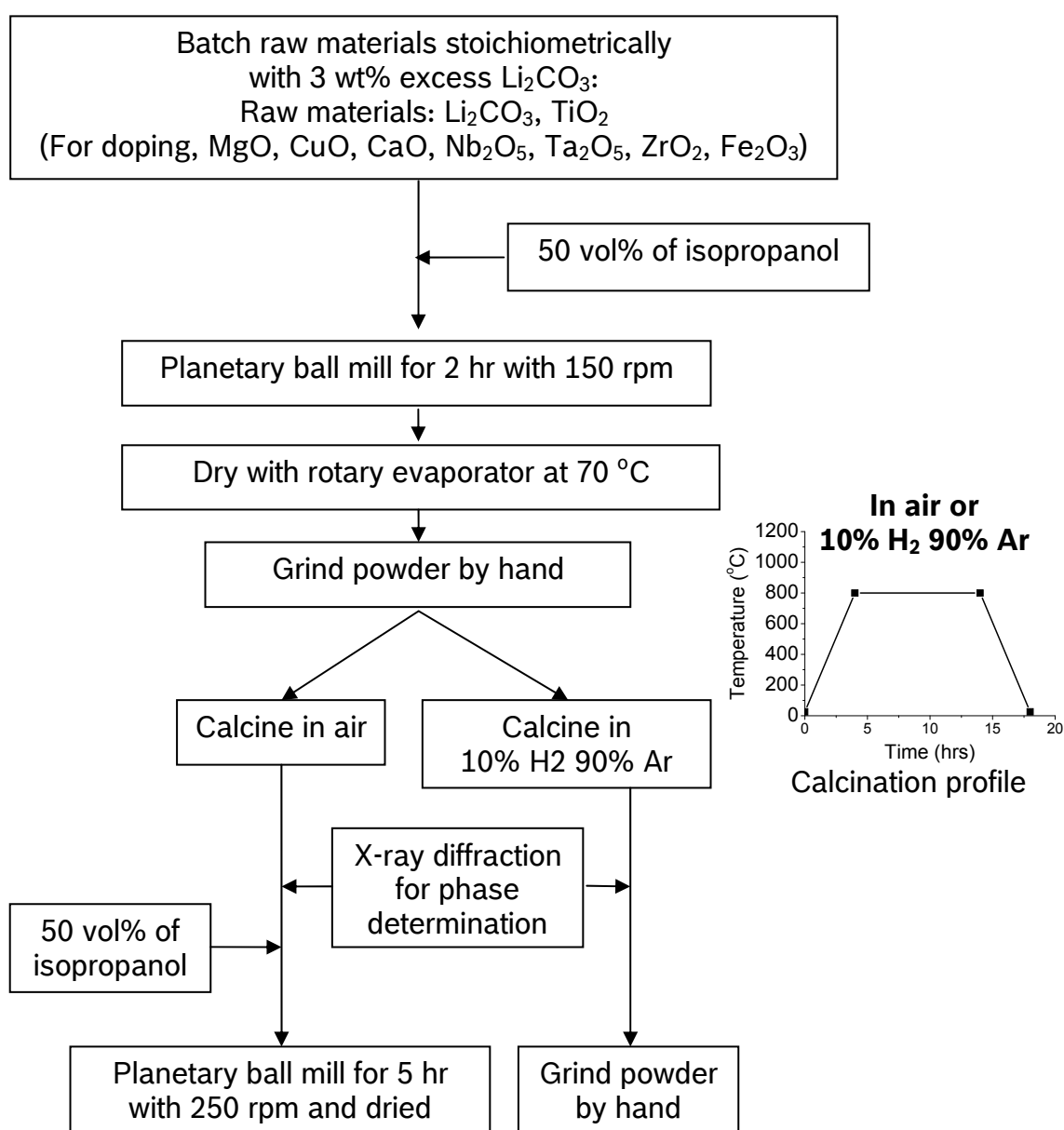
<table>
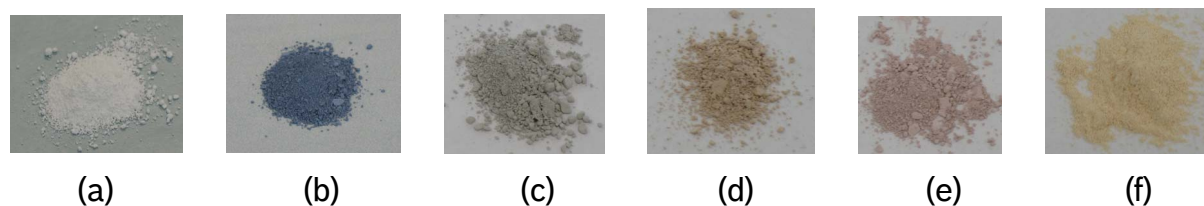<tr><td>(a)</td><td>(b)</td><td>(c)</td><td>(d)</td><td>(e)</td><td>(f)</td></tr>
</table>

Figure 3.2. Pictures of powder before and after calcination: After calcination in (a) air and (b) reducing atmosphere. Cu doped sample, x = 0.1 for $Li_{4/3-x}Cu_xTi_{5/3}O_4$ (c) before and (d) after calcination in air. Fe doped sample x = 0.115 for $Li_{4/3-y/3}Fe_yTi_{5/3-2y/3}O_4$ (e) before and (f) after calcination in air

3.1.1.2 Pellet preparation

Figure 3.3 is the flow chart for pellet preparation. The calcined powder was uniaxially pressed at 300 bar to form disks with 13.6 mm in diameter and about 1 mm in thickness. Samples were then cold isostatically pressed at 2200 bar to increase the green density. The green densities of the pellets after uniaxial pressing and cold isostatic pressing were about 50 % and 60 % theoretical density, respectively. The pellets were subsequently sintered, typically at 950 ^{o}C for spinel and 1100 ^{o}C for ramsdellite for 10 hours. The pellets from the powder calcined in air were sintered in air and the pellets from the powder calcined in reducing atmosphere were sintered in 100% Ar, unless otherwise noted. The estimated P_{O2} for the sintering process in 100% Ar was 10^{-7} atm (Purity of Ar employed: 99.999%). The blue color from the calcination in reducing atmosphere and the brownish color from Cu and Fe doped samples calcined in air remained after sintering in Ar and in air, respectively, as shown in Figure 3.4. For ramsdellite $Li_2Ti_3O_7$ compositions, the samples were quickly cooled down to room temperature to retain the high temperature phase. The cooling rate higher than 500 ^{o}C/hour was confirmed to be sufficient to maintain the pure ramsdellite phase during cooling. Most of the pellets prepared in this way resulted in 85-98 % theoretical density. The samples processed in air were kept in air and the samples processed in reducing atmosphere were kept in a glove box filled with Ar, unless otherwise noted.
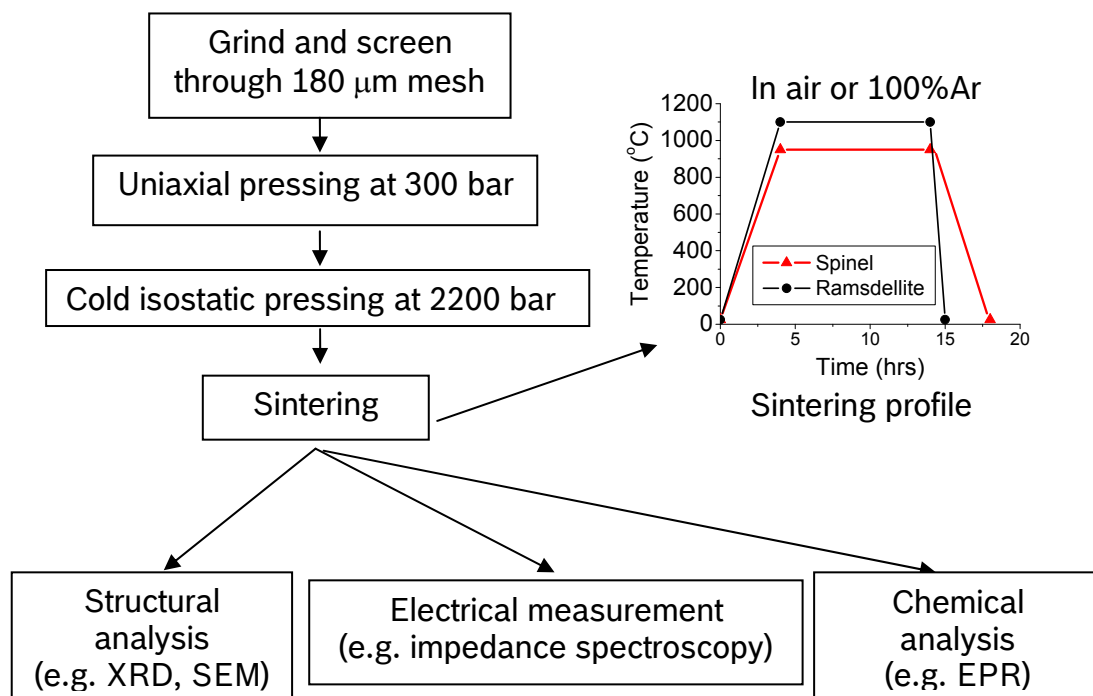
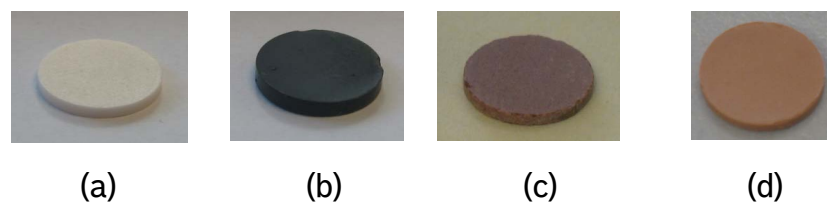Figure 3.3. Flow chart for pellet preparation with the profile for sintering

Figure 3.4. Pictures of pellets after sintering: (a) in air (b) in reducing atmosphere. Only Cu and Fe doped samples processed in air resulted in a different color; (c) Cu doped sample, x = 0.03 for $Li_{4/3-x}Cu_xTi_{5/3}O_4$ (d) Fe doped sample x = 0.115 for $Li_{4/3-y/3}Fe_yTi_{5/3-2y/3}O_4$

3.1.2 Li insertion

Li insertion into spinel $Li_{4/3}Ti_{5/3}O_4$ was performed either electrochemically in Swagelok® cells or chemically in butyllithium or by direct contact with Li metal foil. To avoid the decomposition of the material in air, all preparation steps were conducted in a glove box filled with Ar.

3.1.2.1 Electrochemical insertion

For the electrochemical Li insertion, Swagelok® test cells were assembled with Li metal as an anode and spinel $Li_{4/3}Ti_{5/3}O_4$ as a cathode with 200 µl of 1.0 M $LiPF_6$ in

EC-DEC-DMC (2:2:1 by volume), EC-DEC (1:1 by volume),or 1.0 M LiTFSI in DOL-DME (1:1 by volume) as liquid electrolyte and Celgard® as a separator.* The isostatically pressed pellets and the sintered pellets processed in air and reducing atmosphere were tested with gold sputtered electrode on one surface of the pellets to serve as a current collector.

3.1.2.2 Chemical insertion

For the chemical Li insertion, the sintered pellets were dipped in butyllithium, C_4H_9Li. The method has been shown to be able to effectively insert Li into spinel $Li_{4/3}Ti_{5/3}O_4$ since the chemical potential of butyllithium against Li/Li^+ is smaller than that of spinel $Li_{4/3}Ti_{5/3}O_4$ [Wag06]. The sintered pellets were dipped in a solution of an appropriate amount of butyllithium (15 wt% solution in n-hexane, Merck) and 10 ml of n-hexane (Merck). The solution with the pellets was stirred for 1-30 days at 50 °C.

Li insertion was also performed by contacting Li metal directly to the sintered spinel $Li_{4/3}Ti_{5/3}O_4$ samples. To maintain the good contact between the Li metal and the pellets, the pressure was applied by a spring in Swagelok® cells.

3.1.2.3 Direct synthesis of $Li_{4/3+x}Ti_{5/3}O_4$ (x > 0)

Direct synthesis of $Li_{4/3+x}Ti_{5/3}O_4$ (x > 0) was attempted from a stoichiometric powder mixture of Li_2CO_3, Ti_2O_3, TiO_2, but it failed to achieve the desired phases. The precise control of P_{O2} was not possible with the oven employed in the study. Only Ar and H_2 were available for the oven. The wall of the oven was made of carbon, which may have reduced the atmosphere further without control. Better control of P_{O2} may realize the desired $Li_{4/3+x}Ti_{5/3}O_4$ phase by direct synthesis, but such an attempt was not made in this study.

3.2 Structural characterization

X-ray diffraction (XRD) measurements were performed at room temperature for structural analysis of the calcined powder and the powder which was crushed and ground from sintered pellets, using a Bruker AXS D8 with Cu K_α radiation (40 kV, 50 mA, 0.02 °/step, 3 sec/step). XRD patterns were analyzed using Eva (Version 15,

---

* EC: Ethylene Carbonate, DEC: Diethyl Carbonate, DMC: Dimethyl Carbonate, DOL: Dioxolane, DME: Dimethoxy Ethane, LiTFSI: $LiN(CF_3SO_2)_2$

Bruker AXS). Phase distributions and lattice parameters were calculated using Topas (Version 3, Bruker AXS). Blue samples processed in reducing atmosphere are air sensitive, but measurements were performed in air for higher resolution for lattice parameter determination. No noticeable changes in XRD patterns were found during the measurement in air.

The Li inserted samples were found to be more sensitive in air than the blue samples processed in reducing atmosphere, so closed domes with a rubber O ring were employed. The use of the sample holders, however, resulted in a worse resolution. It was also found that the domes were not completely tight, which made analysis difficult.

3.3 Electrical characterization

3.3.1. Electronic conductivity

In order to measure electronic conductivity, the sintered pellets were polished to achieve parallel and smooth faces, and air-dry silver paste (Acheson, Electrodag SP-413) was painted on both faces of the pellets as electronically conducting and Li-ion blocking electrodes. Resistance was measured either by multimeter (Agilent U1241A) or impedance analyzer (Solartron SI 1260 and 1296) on the sintered pellets. Electronic conductivity was then calculated from the resistance value and the sample geometry. The impedance analyzer is equipped with an order-made furnace which enables the measurement from room temperature up to 700 ^{o}C in almost closed atmosphere environment. The measurement of the samples processed in reducing atmosphere was performed either in a glove box filled with Ar or in the order-made furnace with Ar flow of 50 liter/hour.

3.3.2 Li-ion conductivity

3.3.2.1 Impedance spectroscopy measurement

Li-ion conductivity was measured by impedance spectroscopy for the samples processed in air. Both surfaces of the sintered pellets were polished and gold was sputtered on the surfaces to serve as electrodes. Impedance measurement was performed typically with the AC amplitude of 0.1V from 10 MHz to 1Hz. Figure 3.5 shows a typical Cole-Cole plot obtained for the spinel $Li_{4/3}Ti_{5/3}O_4$ and ramsdellite $Li_2Ti_3O_7$ samples processed in air. According to Huggins, the diameter of the 1st

semicircle was taken as the resistance of the bulk material and the diameter of the 2nd circle was taken as a grain boundary resistance [Hug02].
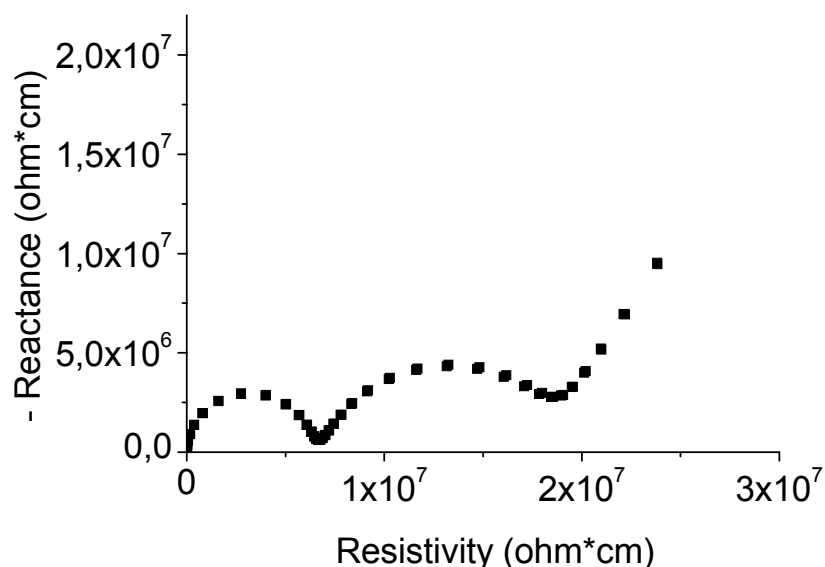

Figure 3.5. A Cole-Cole plot typically obtained for spinel $Li_{4/3}Ti_{5/3}O_4$ and ramsdellite $Li_2Ti_3O_7$ samples processed in air

For the samples processed in reducing atmosphere and the Li inserted samples, Li-ion conductivity could not be measured by impedance spectroscopy since the electronic contribution on total conductivity was far stronger than the ionic contribution.

3.3.2.2 LiPON sputtering

In order to block the electron movement within the samples, Li-ion conductivity measurement with lithium phosphorous oxynitride (LiPON) thin film as electronically blocking electrode was tested on the Li inserted samples. LiPON is an electronic insulator and Li-ion conductor, and has been investigated as a thin film solid electrolyte material in Li-ion battery [Ham06]. When LiPON layers are placed between Li metal and the $Li_{4/3+x}Ti_{5/3}O_4$, as shown in Figure 3.6, only Li-ion conductivity should be measured by applying direct current to this cell, since electrons can not travel through the cell because of the electronically insulating LiPON layers.
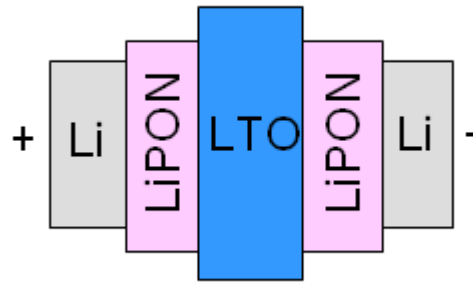
Figure 3.6. A Schematic of the cell set up for the Li-ion conductivity measurement with LiPON as electronically blocking electrodes. LTO stands for $Li_{4/3+x}Ti_{5/3}O_4$

Chapter 4: Results
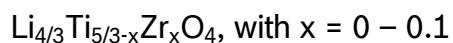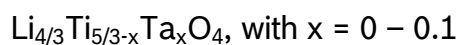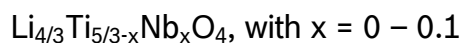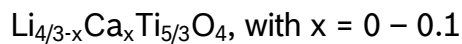
4.1 Spinel Li$_{4/3}$Ti$_{5/3}$O$_4$ ceramics

4.1.1 Compositions

For the spinel Li$_{4/3}$Ti$_{5/3}$O$_4$ system, the samples with the following nominal compositions were prepared. Li$_{4/3}$Ti$_{5/3}$O$_4$ was employed as the base ceramic. Mg, Cu, and Ca were doped to the base composition; the dopants were assumed to sit on the Li site. Nb, Ta, and Zr were also doped, but these dopants were assumed to sit on the Ti site.

Thus the compositions studied were:

Li$_{4/3-x}$Mg$_x$Ti$_{5/3}$O$_4$, with x = 0 − 0.2

Li$_{4/3-x}$Cu$_x$Ti$_{5/3}$O$_4$, with x = 0 − 0.1

Li$_{4/3-x}$Ca$_x$Ti$_{5/3}$O$_4$, with x = 0 − 0.1

Li$_{4/3}$Ti$_{5/3-x}$Nb$_x$O$_4$, with x = 0 − 0.1

Li$_{4/3}$Ti$_{5/3-x}$Ta$_x$O$_4$, with x = 0 − 0.1

Li$_{4/3}$Ti$_{5/3-x}$Zr$_x$O$_4$, with x = 0 − 0.1
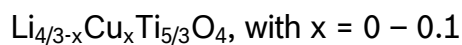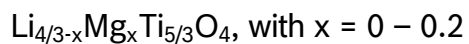
The dopants were chosen based on the ionic size and the valence of the ions, assuming that ions with the same valency or aliovalent ions with relatively similar ionic sizes would be preferred to incorporate into spinel Li$_{4/3}$Ti$_{5/3}$O$_4$ [Kin76]. The aliovalent ions were chosen to possibly introduce Ti^{3+} in the structure, as discussed in section 2.4. Ca, Nb, Ta, and Zr, having bigger ionic radii than the host ions, are doped for possible increase in the lattice size. Zr, which has the same valency as Ti ions in Li$_{4/3}$Ti$_{5/3}$O$_4$ (i.e. 4$^+$), was tested to investigate the influence of the ionic size only.

4.1.2 Structural characterization

To determine Li loss during heat treatment, undoped spinel Li$_{4/3}$Ti$_{5/3}$O$_4$ samples with 0, 1, 3, 5, and 10 wt% excess Li$_2$CO$_3$ were prepared in air. Figure 4.1 shows the XRD patterns of the undoped spinel Li$_{4/3}$Ti$_{5/3}$O$_4$ samples with the excess Li$_2$CO$_3$ after sintering. Although all of the compositions could be prepared in almost pure spinel phases, small second phase peaks were observed in some of the compositions. Figure 4.2 shows the phase distributions. Small peaks of rutile TiO$_2$ (ICSD #51941[FIZ11]) were observed for the 0 and 1 wt% excess Li$_2$CO$_3$ samples, and small Li$_2$TiO$_3$ peaks (ICSD #162215[FIZ11]) were observed for the 5 and 10 wt% excess Li$_2$CO$_3$ samples. The 3 wt% excess Li$_2$CO$_3$ sample resulted in a pure spinel

phase, fitting to the data in ISCD for spinel $Li_{4/3}Ti_{5/3}O_4$ (ICSD #160655[FIZ11]) perfectly. With this result, 3 wt% excess Li_2CO_3 was added to all other compositions to compensate the Li loss during sample preparation.
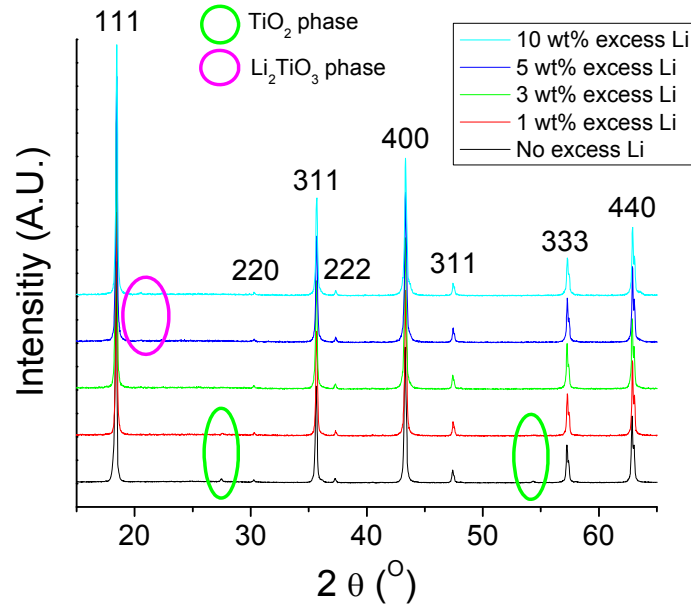

Figure 4.1. X-ray diffraction patterns of spinel $Li_{4/3}Ti_{5/3}O_4$ ceramics with different amount of excess Li_2CO_3. The indexing is based on cubic spinel unit cells

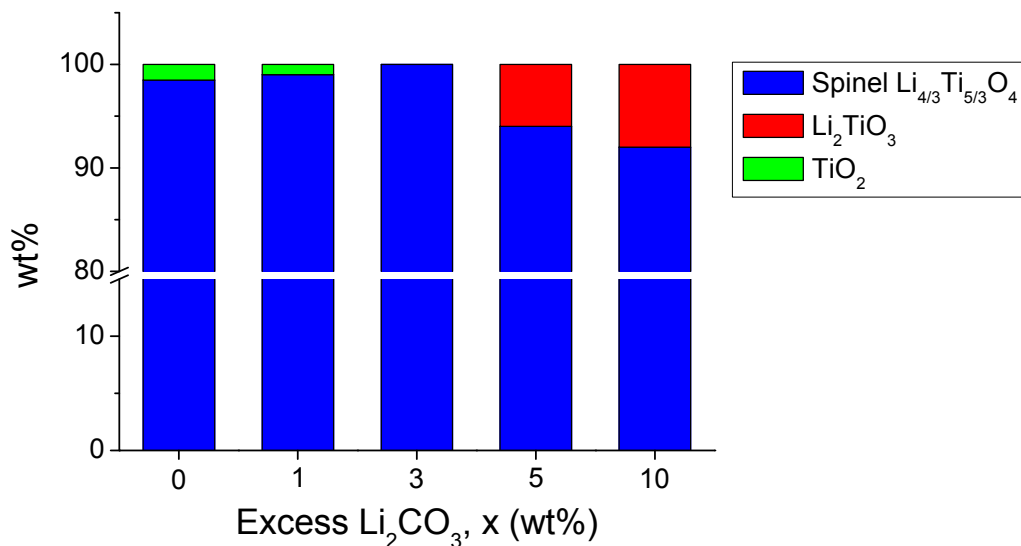Figure 4.2. Phase distributions in wt% for spinel $Li_{4/3}Ti_{5/3}O_4$ with different amount of excess Li_2CO_3. The amount of phases was calculated by Rietvelt analysis on X-ray diffraction data

_____

To investigate the difference in structures and properties by different processing atmospheres, samples were also processed in reducing atmospheres. Figure 4.3 shows the XRD pattern for the sample with 3 wt% excess Li$_2$CO$_3$ processed in reducing atmosphere, 10 % H$_2$ 90 % Ar for calcination and 100 % Ar for sintering, with the sample processed in air for comparison. Second phase peaks of Li$_2$TiO$_3$ were clearly observed in the sample processed in reducing atmosphere. Overlapping of peaks for Li$_2$TiO$_3$ and spinel Li$_{4/3}$Ti$_{5/3}$O$_4$ phases makes the precise quantitative phase analysis difficult, but Rietvelt analysis on the XRD data suggested that up to 7 wt% Li$_2$TiO$_3$ second phase was possible in the sample processed in reducing atmosphere. The lattice parameter was larger for the sample prepared in reducing atmosphere; 8.3639 (+/- 0.00003) Å in reducing atmosphere and 8.3611 (+/- 0.00002) Å in air.
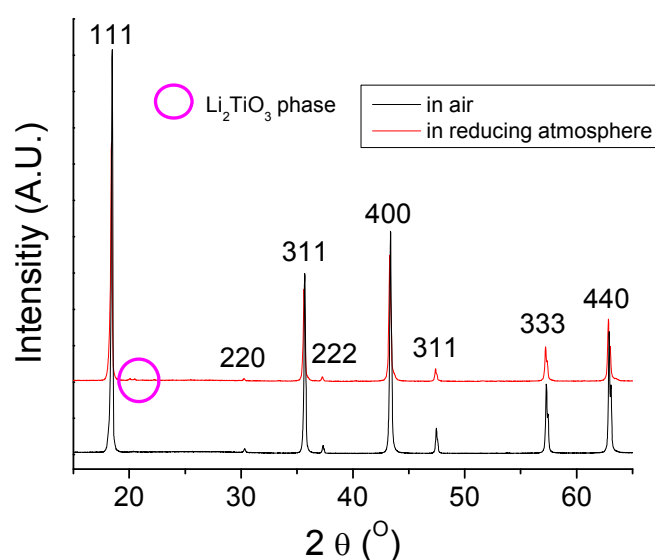
Figure 4.3. X-ray diffraction patterns of spinel Li$_{4/3}$Ti$_{5/3}$O$_4$ ceramics with 3 wt% excess Li$_2$CO$_3$ processed in air and reducing atmosphere (10 % H$_2$ 90 % Ar for calcination and 100 % Ar for sintering). The indexing is based on cubic spinel unit cells

Other combinations of air, Ar, and H$_2$ for different reducing atmospheres were also tested. For example, both calcination and sintering in 10 % H$_2$ 90 % Ar, or calcination in air and sintering in 10 % H$_2$ 90 % Ar resulted in significant peaks of non-spinel second phases. Since the pure spinel phase is of interest in this study, the process with 10 % H$_2$ 90 % Ar for calcination and 100 % Ar for sintering was

employed as a standard process in reducing atmosphere.

Table 4.1 shows the solubility of the dopants into spinel $Li_{4/3}Ti_{5/3}O_4$. Shannon ionic radii of the dopants are also listed in the table [Sha76]. Solubility was confirmed by checking XRD patterns if there was no second phases except TiO_2 or Li_2TiO_3. Most of the samples, except undoped spinel $Li_{4/3}Ti_{5/3}O_4$ processed in air, contained up to 7 wt% TiO_2 or Li_2TiO_3.

Table 4.1. Solubility of the dopants into spinel $Li_{4/3}Ti_{5/3}O_4$ ceramic. Shannon ionic radii of dopants, Li, and Ti ions are listed [Sha76]

Structure	Dopant	Chemical formula	Solubility confirmed x = (at least)	Shannon Ionic radius (Å)	
				tetrahedral	octahedral
Spinel	Mg^{2+}	$Li_{4/3-x}Mg_xTi_{5/3}O_4$	0.15	0.57	0.72
	Cu^{2+}	$Li_{4/3-x}Cu_xTi_{5/3}O_4$	0.1 (only in air)	0.57	0.73
	Ca^{2+}	$Li_{4/3-x}Ca_xTi_{5/3}O_4$	No solubility	-	1
	Nb^{5+}	$Li_{4/3}Ti_{5/3-x}Nb_xO_4$	0.03	0.48	0.64
	Ta^{5+}	$Li_{4/3}Ti_{5/3-x}Ta_xO_4$	0.01	-	0.64
	Zr^{4+}	$Li_{4/3}Ti_{5/3-x}Zr_xO_4$	0.01	0.59	0.72
Size of Li and Ti	Li^{1+}	-	-	0.59	0.76
	Ti^{4+}	-	-	0.42	0.605
	Ti^{3+}	-	-	-	0.67

Figure 4.4 and 4.5 show XRD patterns and phase distributions for the Mg doped samples, respectively. Most of the samples processed in air contained TiO_2 and all of the samples processed in reducing atmosphere contained Li_2TiO_3. Mg could be doped on the Li sites with relatively high doping amount, up to x = 0.15 for $Li_{4/3-x}Mg_xTi_{5/3}O_4$, without the introduction of the second phase, Mg_2TiO_5 (ICSD #51022[FIZ11]).

(a)

(b)
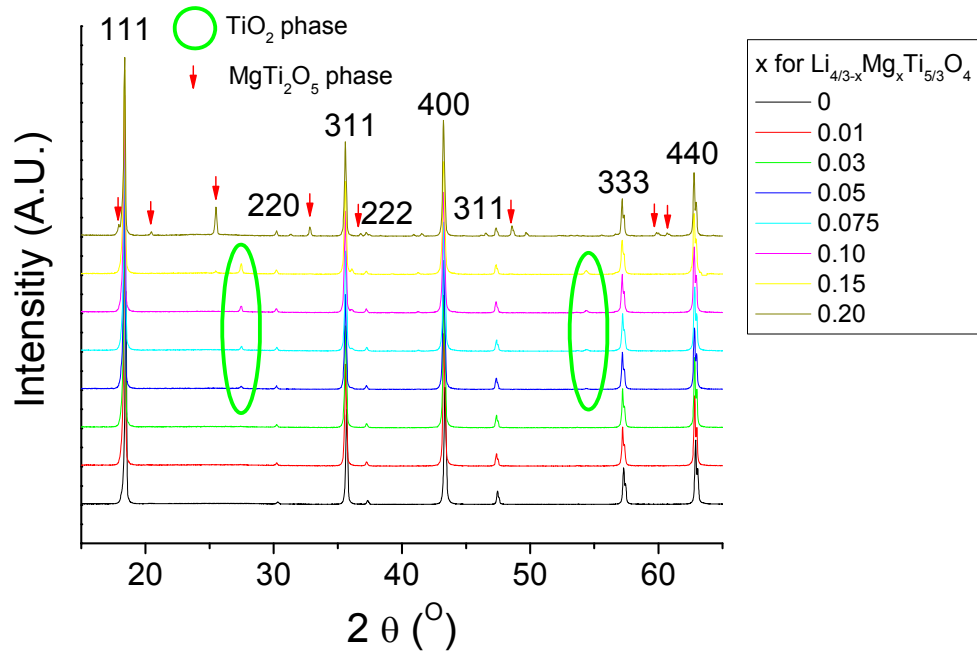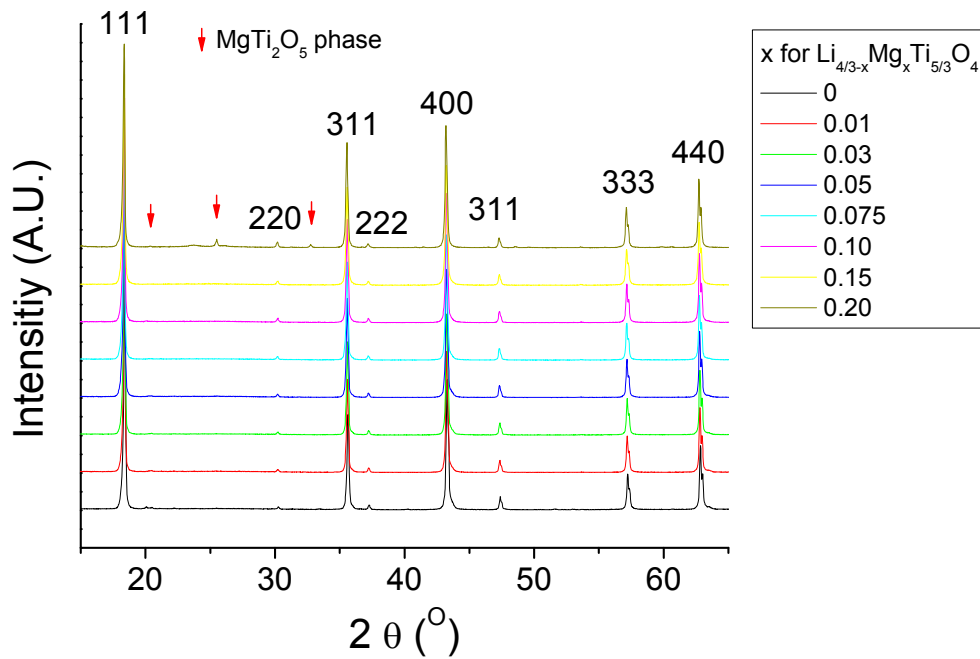
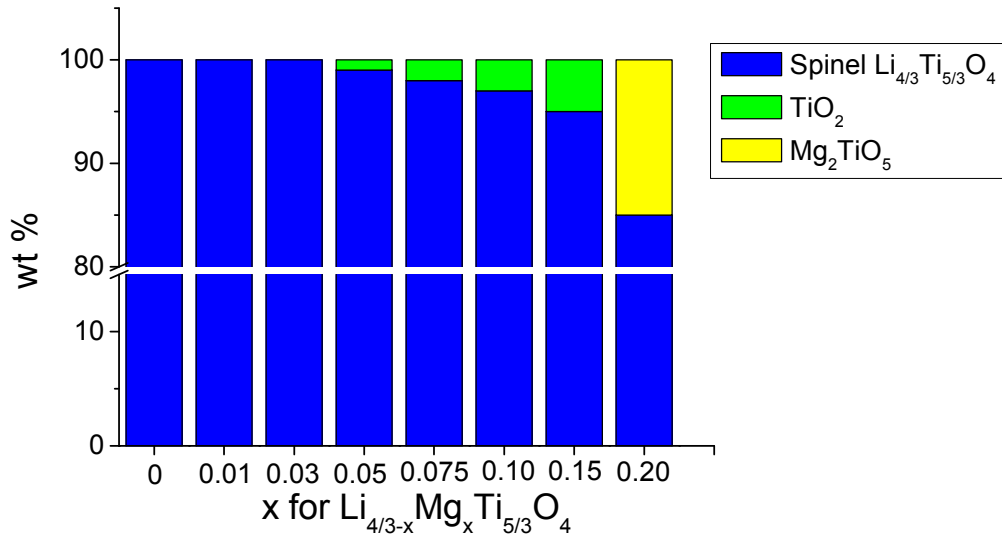Figure 4.4. X-ray diffraction patterns of Mg doped spinel Li$_{4/3-x}$Mg$_x$Ti$_{5/3}$O$_4$ ceramics processed in (a) air and (b) reducing atmosphere (10 % H$_2$ 90 % Ar for calcination and 100 % Ar for sintering). The indexing is based on cubic spinel unit cells

(a)
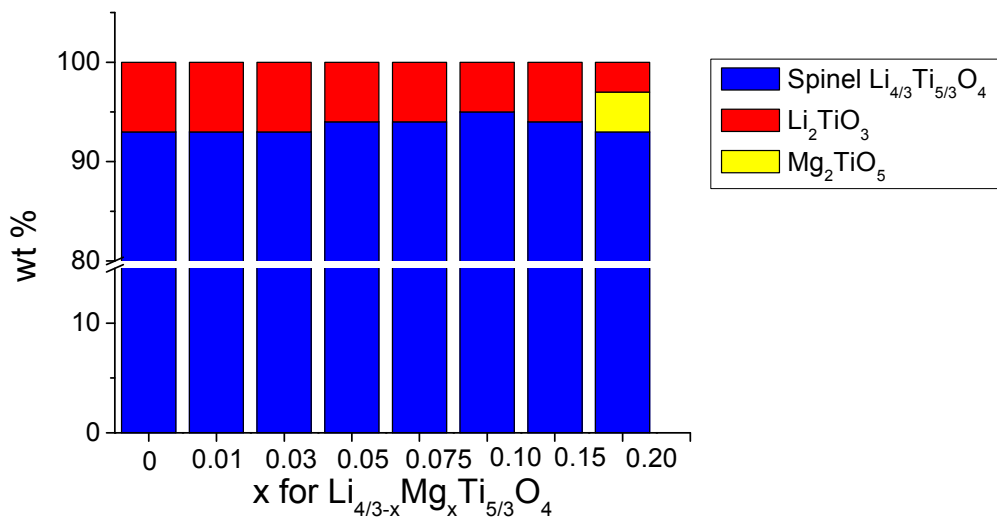
(b)

Figure 4.5. Phase distributions in wt% for Mg doped spinel $Li_{4/3-x}Mg_xTi_{5/3}O_4$ ceramics processed in (a) air and (b) reducing atmosphere (10 % H_2 90 % Ar for calcination and 100 % Ar for sintering). The amount of phases was calculated by Rietvelt analysis on X-ray diffraction data

To confirm if Mg ions sit on the tetrahedral or octahedral Li sites, (220) peak in the XRD pattern was carefully analyzed. The (220) peak is sensitive only to the ions in the tetrahedral sites in the spinel $Li_{4/3}Ti_{5/3}O_4$ [Che01]. Since the tetrahedral sites are occupied only by Li ions in the undoped spinel $Li_{4/3}Ti_{5/3}O_4$ and Li^+ ion has a much smaller scattering factor than the other ions [Cul01], comparing the size of the (220)

peak implies if the dopants are on the tetrahedral sites or not. Figure 4.6 shows the magnified XRD patterns of the (220) peak. The peak became larger with the increasing concentration of Mg from x = 0 up to 0.20, suggesting that there are more Mg ions sitting on the tetrahedral sites with the increasing dopant concentration of Mg. The increase was similar for the sample processed in air and reducing atmosphere. The small peak intensity of the (220) peaks was not sufficient for quantitative analysis.
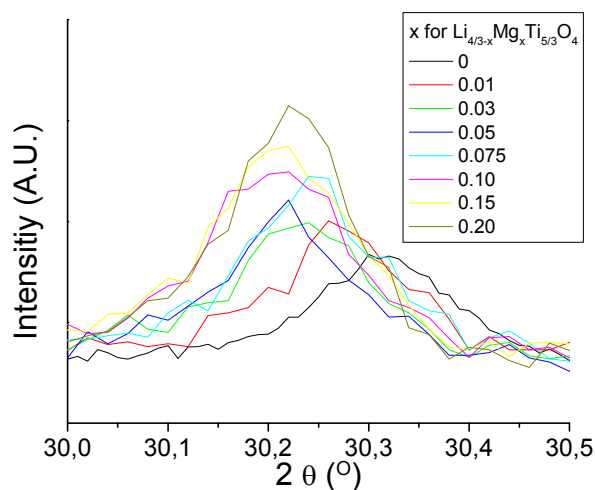
(a)
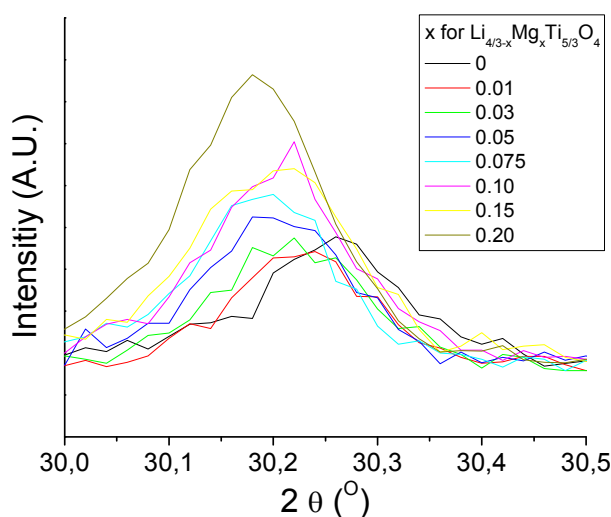
(b)

Figure 4.6. X-ray diffraction patterns around (220) peak on Mg doped spinel Li$_{4/3-x}$Mg$_x$Ti$_{5/3}$O$_4$ ceramics processed in (a) air and (b) reducing atmosphere (10 % H$_2$ 90 % Ar for calcination and 100 % Ar for sintering)

Cu showed the solubility of x = 0.1 for $Li_{4/3-x}Cu_xTi_{5/3}O_4$ when processed in air, but processing in reducing atmosphere resulted in elemental Cu as a second phase. Similar to the Mg doped samples, Cu ions on Li tetrahedral sites were observed from the (220) peak of the samples processed in air. However, no significant difference in the size of (220) peak was observed for the samples with and without Fe doping processed in reducing atmosphere. Nb, Ta, and Zr doping on Ti sites did not show large solubilities (up to x = 0.03) and Ca did not go into the structure at all.

Figure 4.7 (a) and (b) show lattice parameters as a function of the dopant concentration for the doped spinel $Li_{4/3}Ti_{5/3}O_4$ samples processed in air and in reducing atmosphere, respectively. The lattice parameters were calculated by Rietvelt analysis on the XRD patterns. The result shows that Mg, Cu, Nb, Ta, and Zr doping increased the lattice parameter of samples processed in both air and reducing atmosphere. The samples processed in reducing atmosphere resulted in larger lattice parameters than the samples processed in air as in the undoped spinel $Li_{4/3}Ti_{5/3}O_4$.
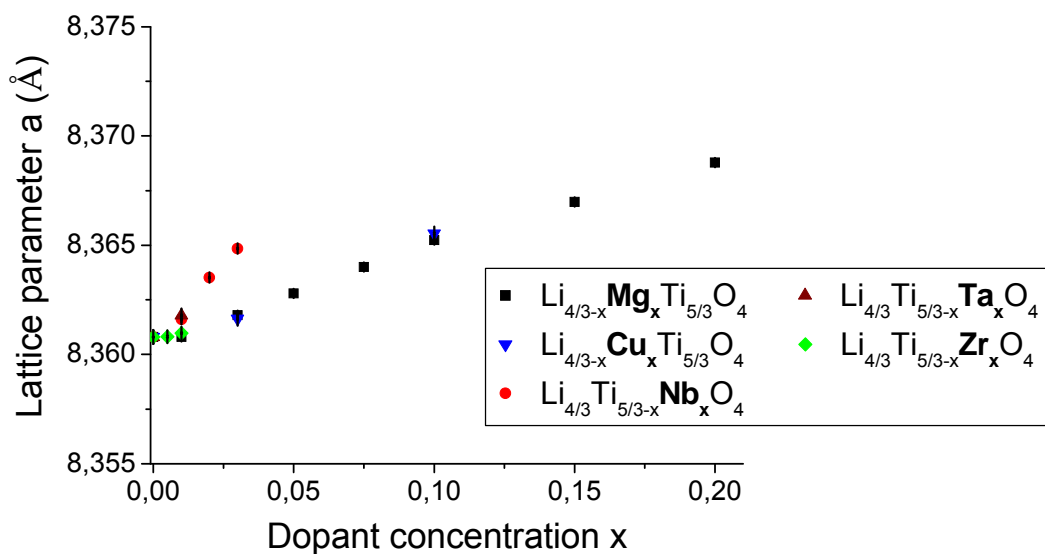
(a)
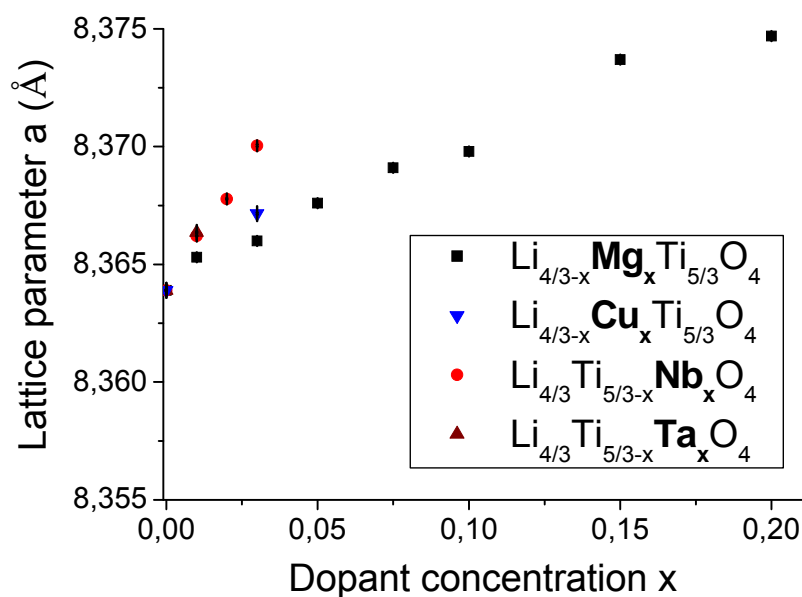
(b)

Figure 4.7. Lattice parameter as a function of dopant concentration for doped spinel $Li_{4/3}Ti_{5/3}O_4$ samples processed in (a) air and (b) reducing atmosphere (10 % H_2 90 % Ar for calcination and 100 % Ar for sintering). Lattice parameters were calculated by Rietvelt analysis on XRD data

4.1.3 Electric properties

4.1.3.1 Electronic conductivity

4.1.3.1.1 Undoped spinel $Li_{4/3}Ti_{5/3}O_4$

The sample processed in air resulted in white color and an electrically insulator with electronic conductivity < 10^{-9} S/cm. The resolution of the multimeter employed in this study was not sufficient to determine the electronic conductivity in the range accurately. The sample processed in reducing atmosphere revealed a blue color, as shown in Figure 3.4, and the higher electronic conductivity in the order of 10^{-2} S/cm.

Figure 4.8 shows the change in the electronic conductivity of the spinel $Li_{4/3}Ti_{5/3}O_4$ pellet processed in reducing atmosphere with time in air. Within the first few days, the electrical conductivity decreased significantly, down to 10^{-4} S/cm, and was saturated at about 10^{-5} S/cm after one month. After polishing the surface and re-electroding, the electronic conductivity was partially recovered to about 10^{-3} S/cm, shown as the red data point in Figure 4.8.
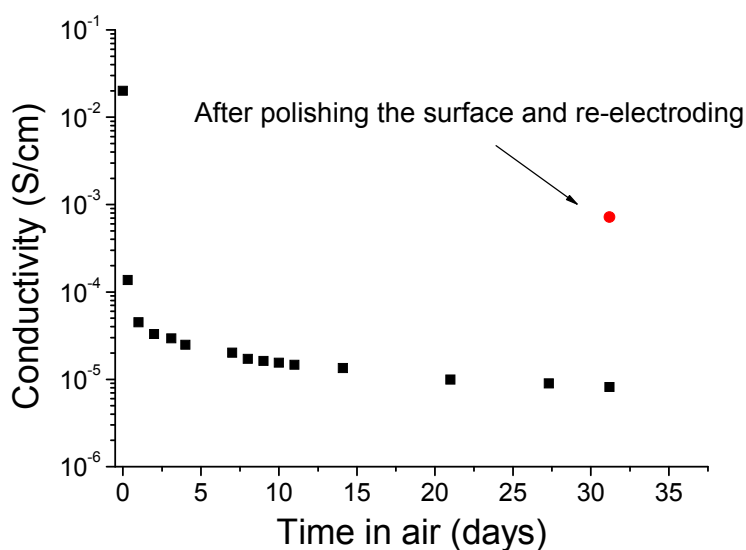
Figure 4.8. Electronic conductivity at room temperature as a function of time in air for the spinel $Li_{4/3}Ti_{5/3}O_4$ pellet processed in reducing atmosphere

In order to investigate the electronic conduction mechanism, activation energy for the electronic conduction of the spinel $Li_{4/3}Ti_{5/3}O_4$ sample processed in reducing atmosphere was measured. Figure 4.9 shows the electronic conductivity as a function of temperature for the spinel $Li_{4/3}Ti_{5/3}O_4$ samples processed in reducing atmosphere which had been in air for 0, 1, 2, 8, and 28 days before measurement.

The calculated activation energy for each sample is also shown in Figure 4.9.

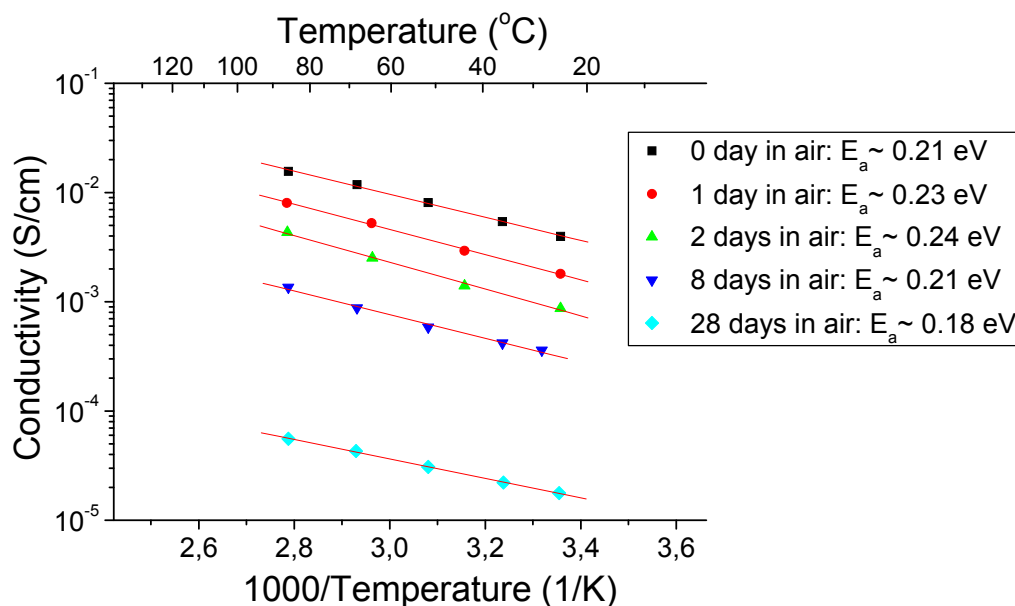Figure 4.9. Electronic conductivity as a function of temperature for spinel Li$_{4/3}$Ti$_{5/3}$O$_4$ processed in reducing atmosphere which had been in air for 0, 1, 2, 8, and 28 days. The solid lines are fitted to an Arrhenius model. Measurement was performed in Ar atmosphere

The conduction was confirmed to be thermally activated. Although the electronic conductivity was degraded with time in air, the activation energies for all samples with different durations in air were in the same range, about 0.2 eV.

4.1.3.1.2. Doped spinel Li$_{4/3}$Ti$_{5/3}$O$_4$

Figure 4.10 shows electronic conductivity of the spinel Li$_{4/3}$Ti$_{5/3}$O$_4$ samples doped with Mg, Cu, Nb, Ta, and Zr processed in air or reducing atmosphere.
When processed in air, only Cu doped samples increased the electric conductivity. Cu doping on spinel Li$_{4/3}$Ti$_{5/3}$O$_4$ resulted in the brownish color, shown in Figure 3.4 and increased the conductivity slightly, about 10^{-7} S/cm with x = 0.1 for Li$_{4/3-x}$Cu$_x$Ti$_{5/3}$O$_4$. The conductivity was measured by impedance spectroscopy, so the value may account for either electronic or Li-ion conductivity. The reason why this is considered to be electronic conductivity is discussed in section 5.1.2.1.

When processed in reducing atmosphere, the samples doped with Mg, Nb, Ta, and Zr showed no obvious increase in electronic conductivity compared with the

undoped spinel $Li_{4/3}Ti_{5/3}O_4$. However, Cu doped samples processed in reducing atmosphere increased electronic conductivity further above the target value, and exhibited always higher values than the undoped samples or the samples doped with the other elements.
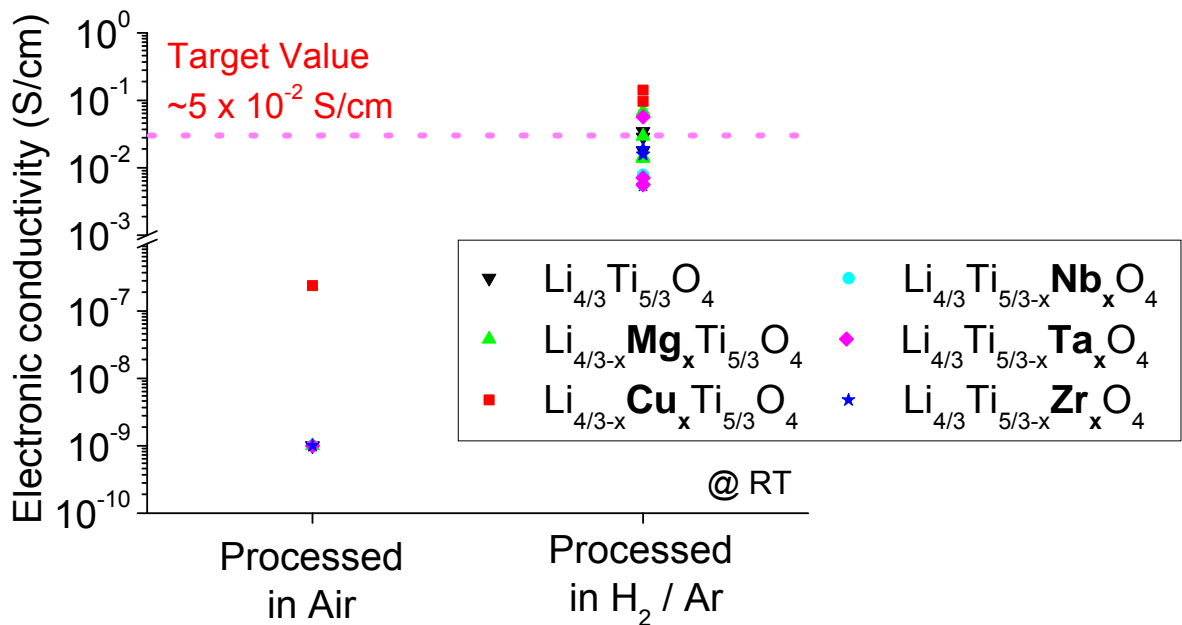
Figure 4.10. Electronic conductivity at room temperature for spinel $Li_{4/3}Ti_{5/3}O_4$ doped with Mg, Cu, Nb, Ta, and Zr processed in air or reducing atmosphere (10 % H_2 90 % Ar for calcination and 100 % Ar for sintering)

To understand the effect of Cu doping on electronic conductivity, the activation energy for the Cu doped sample processed in reducing atmosphere was calculated by measuring electronic conductivity at different temperatures with impedance spectroscopy. Figure 4.11 (a) and (b) show electronic conductivity as a function of temperature for the Cu doped spinel $Li_{4/3}Ti_{5/3}O_4$ and the Mg / Ta doped spinel $Li_{4/3}Ti_{5/3}O_4$ with the calculated activation energies, respectively. The activation energy for the Cu doped spinel, $Li_{4/3-0.03}Cu_{0.03}Ti_{5/3}O_4$, was significantly different from the other samples; the Cu doped sample ~ 0.089 eV and the others ~ 0.21 eV,

(a)

(b)
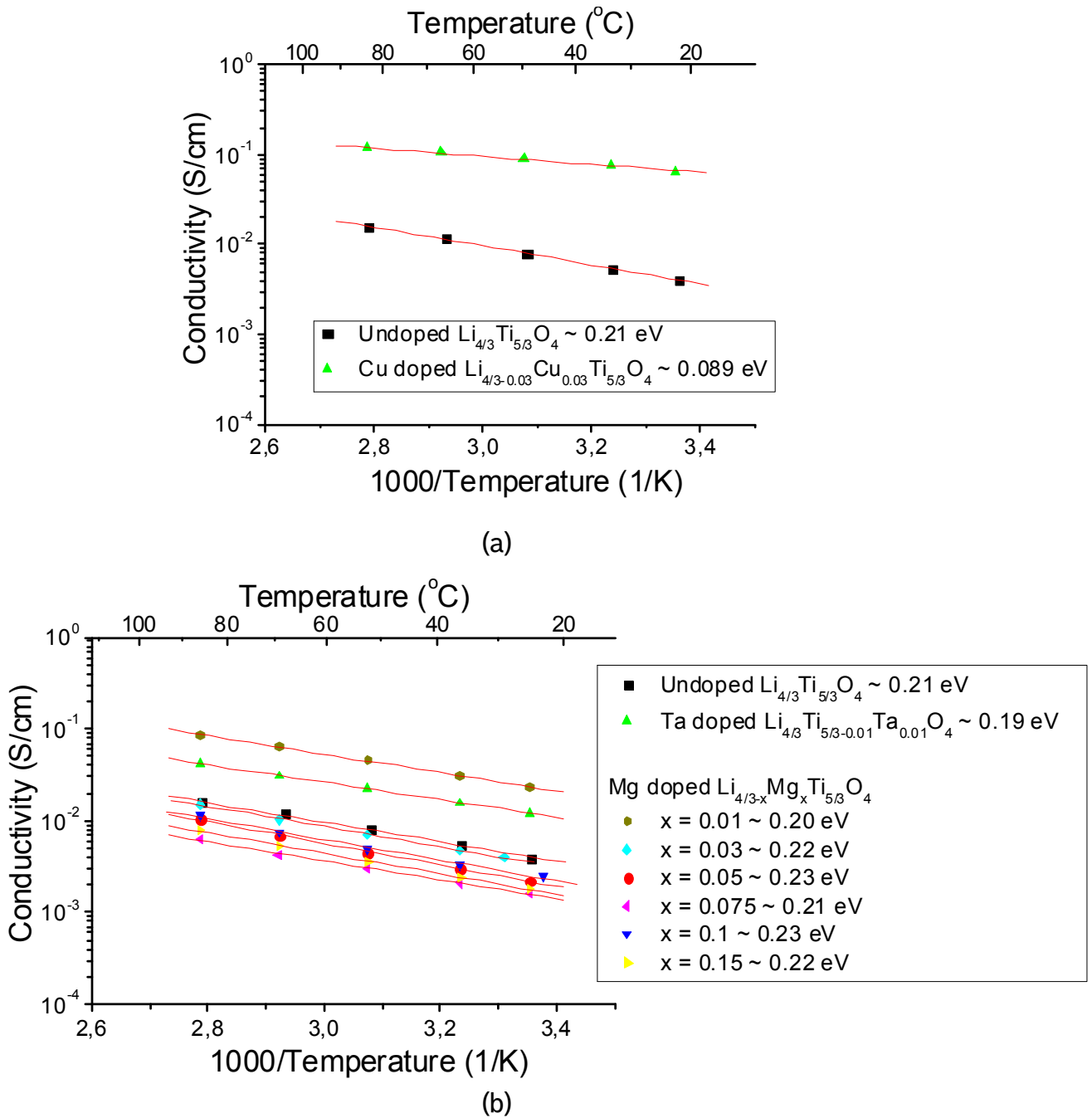
Figure 4.11. Electronic conductivity as a function of temperature for (a) Cu and (b) Ta/Mg doped spinel Li$_{4/3}$Ti$_{5/3}$O$_4$ samples processed in reducing atmosphere. The solid lines are fitted to an Arrhenius model. Measurements were performed in Ar atmosphere

To see the effect of dopant concentration on electronic conductivity, Mg doped samples with different dopant concentrations were investigated. Figure 4.12 and 4.13 show the electronic conductivity and activation energy as a function of Mg dopant concentration for Mg doped spinel $Li_{4/3}Ti_{5/3}O_4$ samples, respectively. For the samples processed in air, no change in electronic conductivity was observed within the resolution of the test setup. For the samples processed in reducing atmosphere, there was a scatter of electronic conductivities, but no obvious trend in the conductivity with Mg concentration was found. The activation energies for the samples processed in reducing atmosphere were ~ 0.22 eV for all the Mg doped samples, as shown in Figure 4.13.
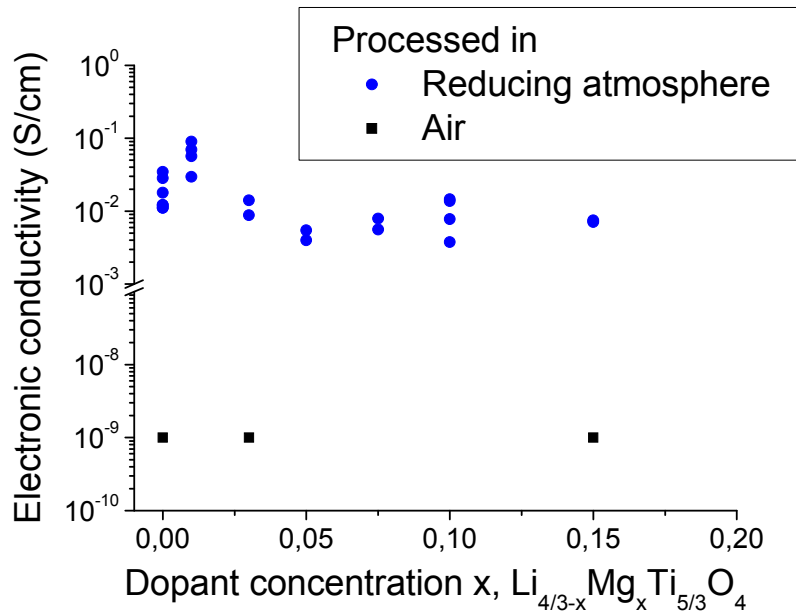
Figure 4.12. Electronic conductivity at room temperature as a function of Mg dopant concentration for Mg doped spinel $Li_{4/3}Ti_{5/3}O_4$ samples
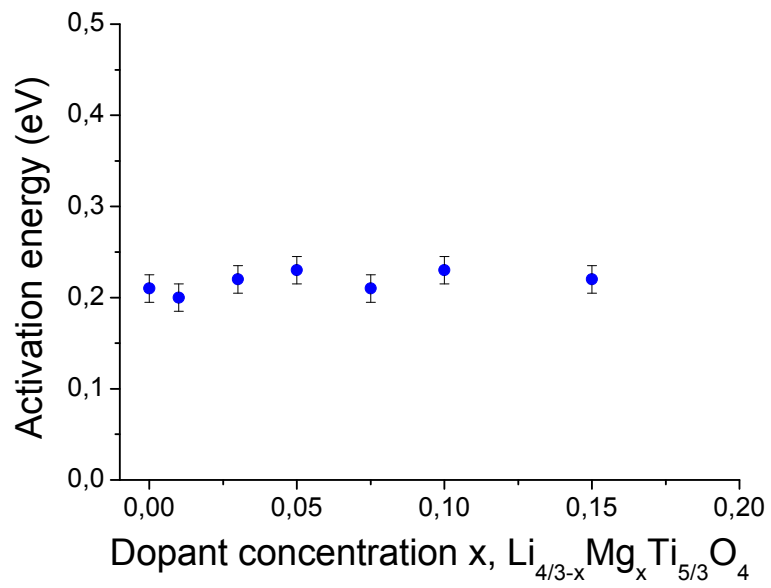
Figure 4.13. Activation energy as a function of Mg dopant concentration for Mg doped spinel $Li_{4/3}Ti_{5/3}O_4$ samples processed in reducing atmosphere

4.1.3.2 Li-ion conductivity

4.1.3.2.1 Undoped spinel $Li_{4/3}Ti_{5/3}O_4$

The pellet processed in air resulted in a Li-ion conductivity of $\sim 10^{-7}$ S/cm. Activation energy for Li-ion conduction was also calculated by measuring Li-ion conductivity at different temperatures with impedance spectroscopy and fitting the data to an Arrhenius model in the same manner described in the previous section for electronic conductivity.   Figure 4.14 shows the Li-ion conductivity multiplied by temperature as a function of temperature for the undoped spinel $Li_{4/3}Ti_{5/3}O_4$ with the calculated activation energy.
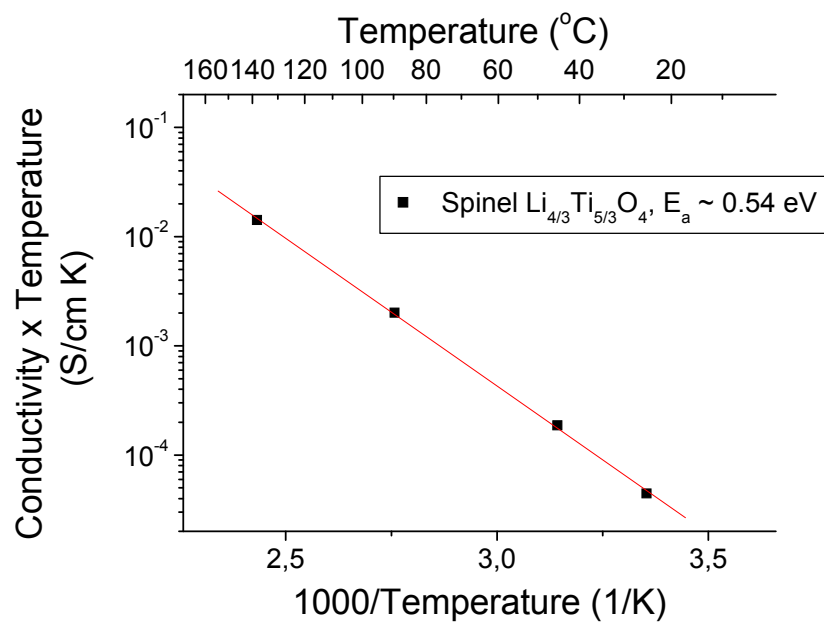

Figure 4.14. Li-ion conductivity multiplied by temperature as a function of temperature for undoped spinel $Li_{4/3}Ti_{5/3}O_4$. The solid lines are fitted to an Arrhenius model

Li-ion conductivity in the samples processed in reducing atmosphere is difficult to be measured.   The high electronic conductivity in the sample makes the Li-ion conductivity measurement impossible with impedance spectroscopy.   Measurement with electronically blocking electrodes would make it possible to measure Li-ion conductivity in mixed conducting materials.   Such measurements were not performed on the samples processed in reducing atmosphere, but performed on the samples with Li insertion (see section 4.3.4).

4.1.3.2.2 Doped spinel $Li_{4/3}Ti_{5/3}O_4$

Figure 4.15 shows Li-ion conductivity as a function of dopant concentration for the doped spinel $Li_{4/3}Ti_{5/3}O_4$ samples processed in air. The result shows that Li-ion conductivity did not increase with the dopants. The conductivity even decreased with Mg and Cu doping.
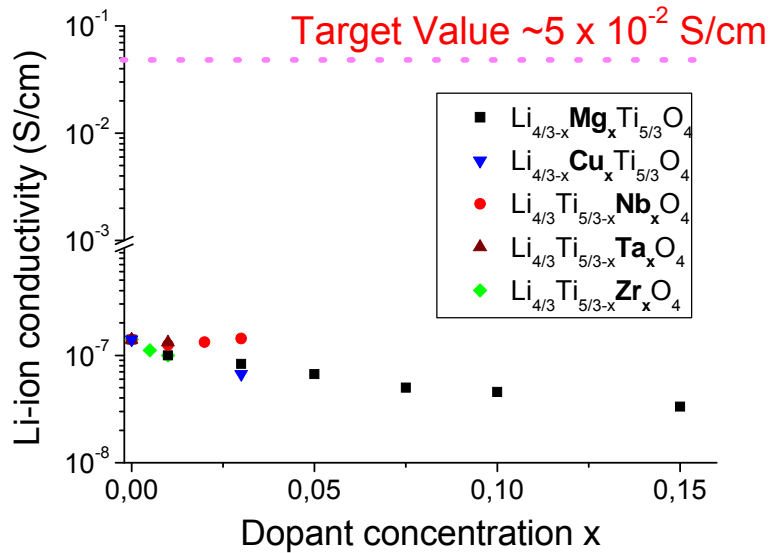
Figure 4.15. Li-ion conductivity at room temperature as a function of dopant concentration for doped spinel $Li_{4/3}Ti_{5/3}O_4$ samples processed in air

4.2 Ramsdellite $Li_2Ti_3O_7$ ceramics

4.2.1 Compositions

For the ramsdellite $Li_2Ti_3O_7$ system, the samples with the following nominal compositions were prepared. $Li_2Ti_3O_7$ was employed as the base ceramic. Mg and Cu were doped to the base composition; the dopants were assumed to sit on the Li site. Nb and Zr were also doped, but these dopants were assumed to sit on the Ti site.

Thus the compositions studied were:

$Li_{2-x}Mg_xTi_3O_7$, with x = 0 − 0.2

$Li_{2-x}Cu_xTi_3O_7$, with x = 0 − 0.2

$Li_2Ti_{3-x}Nb_xO_7$, with x = 0 − 0.2

$Li_2Ti_{3-x}Zr_xO_7$, with x = 0 − 0.2
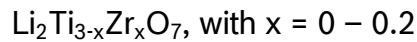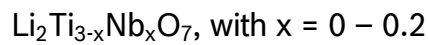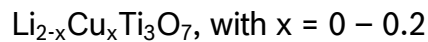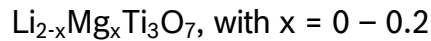
The dopants were chosen based on the ionic size and the valence of the ions, similarly as for the doped spinel $Li_{4/3}Ti_{5/3}O_4$ samples.

4.2.2 Structural characterization

Ramsdellite $Li_2Ti_3O_7$ was prepared with 3 wt% excess Li_2CO_3 as in the spinel $Li_{4/3}Ti_{5/3}O_4$ samples to compensate the Li loss during preparation. Figure 4.16 shows a XRD pattern for undoped $Li_2Ti_3O_7$ samples with 3 wt% excess Li_2CO_3 processed in air after sintering. The pattern fits perfectly to the data for ramsdellite $Li_2Ti_3O_7$ (ICSD #51229[FIZ11]).
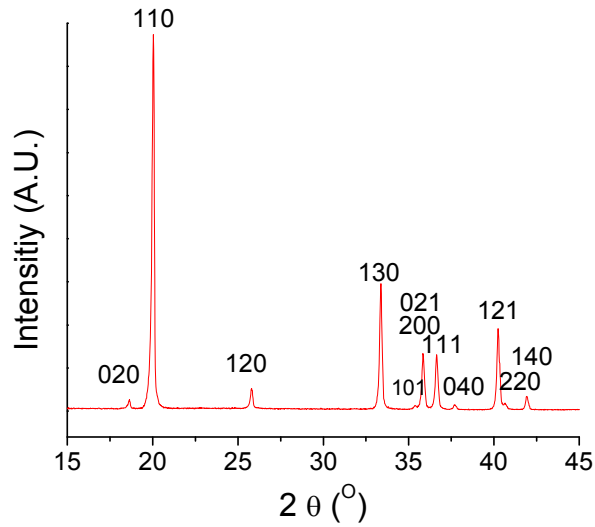
Figure 4.16. X-ray diffraction pattern of ramsdellite Li$_2$Ti$_3$O$_7$ ceramics with 3 wt% excess Li$_2$CO$_3$ processed in air. The indexing is based on orthorhombic ramsdellite unit cells

Unlike spinel Li$_{4/3}$Ti$_{5/3}$O$_4$, ramsdellite Li$_2$Ti$_3$O$_7$ has a narrow solid solution range in the Li$_2$O-TiO$_2$ phase diagram [Izq80]. To confirm the solid solution range and to check the structural and electrical properties with the different Li contents, the ramsdellite compositions with -0.1 < x < 0.1 for Li$_{2+x}$Ti$_3$O$_{7+x/2}$ were prepared in air. Figure 4.17 shows the phase distributions in wt%. The lattice parameters were also calculated by Rietvelt analysis on the XRD data. Figure 4.18 shows the unit cell volume as a function of x for Li$_{2+x}$Ti$_3$O$_{7+x/2}$, suggesting that the volume increases with increasing x for Li$_{2+x}$Ti$_3$O$_{7+x/2}$.
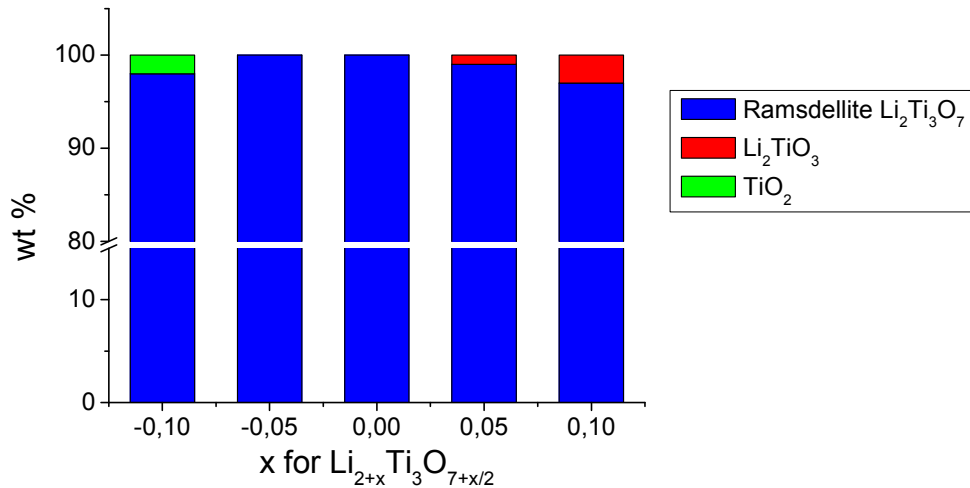
Figure 4.17. Phase distributions in wt% for ramsdellite $Li_{2+x}Ti_3O_{7+x/2}$ prepared in air. The amount of phases was calculated by Rietvelt analysis on XRD data
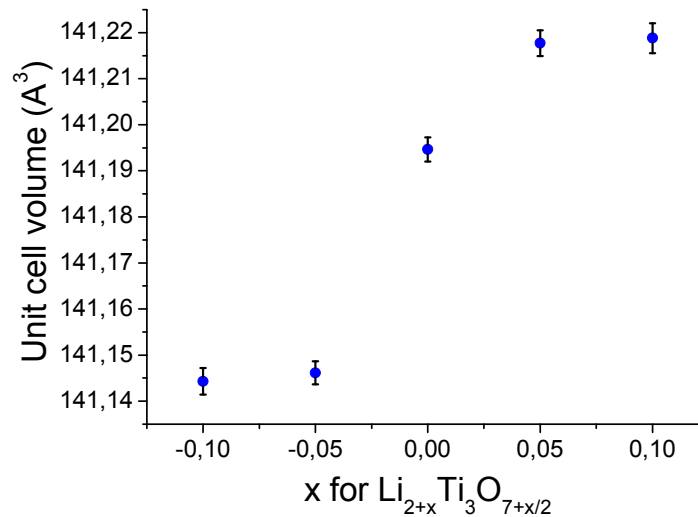
Figure 4.18. Unit cell volume at room temperature as a function of the amount of x for ramsdellite $Li_{2+x}Ti_3O_{7+x/2}$ samples processed in air. The lattice parameters were calculated by Rietvelt analysis on XRD data

Table 4.2 shows the solubility of dopants into ramsdellite $Li_2Ti_3O_7$ structure. Shannon ionic radii of the dopants are also listed in the Table [Sha76]. Solubility was confirmed by checking XRD patterns if there was no second phases except TiO_2 or Li_2TiO_3. Similar to the spinel $Li_{4/3}Ti_{5/3}O_4$, most of the samples except undoped ramsdellite $Li_2Ti_3O_7$ processed in air, contained up to 7 wt% TiO_2 or Li_2TiO_3. For ramsdellite $Li_2Ti_3O_7$, Mg, Cu, and Zr doped samples showed relatively good solubility, x ~ 0.1, except the Cu doped samples processed in reducing atmosphere with

elemental Cu as a second phase. Nb doped sample showed even better solubility, x = 0.2.

Table 4.2. Solubility of the dopants into ramsdellite Li$_2$Ti$_3$O$_7$ ceramic. Shannon ionic radii of dopants, Li, and Ti ions are listed [Sha76]

Structure	Dopant	Chemical formula	Solubility confirmed (at least)	Shannon Ionic radius (Å)	
				tetrahedral	octahedral
Ramsdellite	Mg^{2+}	Li$_{2-x}$Mg$_x$Ti$_3$O$_7$	0.105	0.57	0.72
	Cu^{2+}	Li$_{2-x}$ Cu$_x$Ti$_3$O$_7$	0.1 (only in air)	0.57	0.73
	Nb^{5+}	Li$_2$Ti$_{3-x}$Nb$_x$O$_7$	0.2	0.48	0.64
	Zr^{4+}	Li$_2$Ti$_{3-x}$Zr$_x$O$_7$	0.1	0.59	0.72
Size of Li and Ti	Li^{1+}	-	-	0.59	0.76
	Ti^{4+}	-	-	0.42	0.605
	Ti^{3+}	-	-	-	0.67

Figure 4.19 shows a unit cell volume as a function of dopant concentration for the doped ramsdellite Li$_2$Ti$_3$O$_7$ samples processed in air. The result shows that Mg, Nb, and Zr doping increased the unit cell volume linearly, whereas Cu doping slightly decreased the volume.
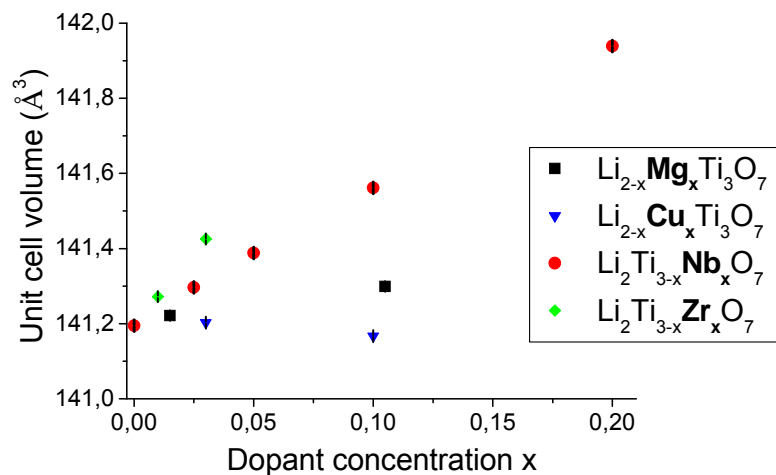
Figure 4.19. Unit cell volume as a function of dopant concentration for doped ramsdellite Li$_2$Ti$_3$O$_7$ samples processed in air. Lattice parameters were calculated by Rietvelt analysis on XRD data.

4.2.3 Electric properties

4.2.3.1 Electronic conductivity

Electronic conductivity of the undoped ramsdellite $Li_2Ti_3O_7$ was very similar to the undoped spinel $Li_{4/3}Ti_{5/3}O_4$. The pellet processed in air resulted in white color and an electrically insulator with an electronic conductivity of $< 10^{-9}$ S/cm. The pellet processed in reducing atmosphere resulted in the blue color similar to the spinel $Li_{4/3}Ti_{5/3}O_4$, and a higher electronic conductivity in the order of 10^{-2} S/cm.

Figure 4.20 shows electronic conductivity on ramsdellite $Li_2Ti_3O_7$ doped with Mg, Cu, Nb, and Zr in terms of processing atmospheres. When processed in reducing atmosphere, the samples doped with Mg, Nb, Ta, and Zr showed no obvious increase in electronic conductivity compared with the undoped ramsdellite $Li_2Ti_3O_7$. However, similar to the spinel $Li_{4/3}Ti_{5/3}O_4$ system, the Cu doped samples processed in reducing atmosphere increased electronic conductivity further, which was above the target value.
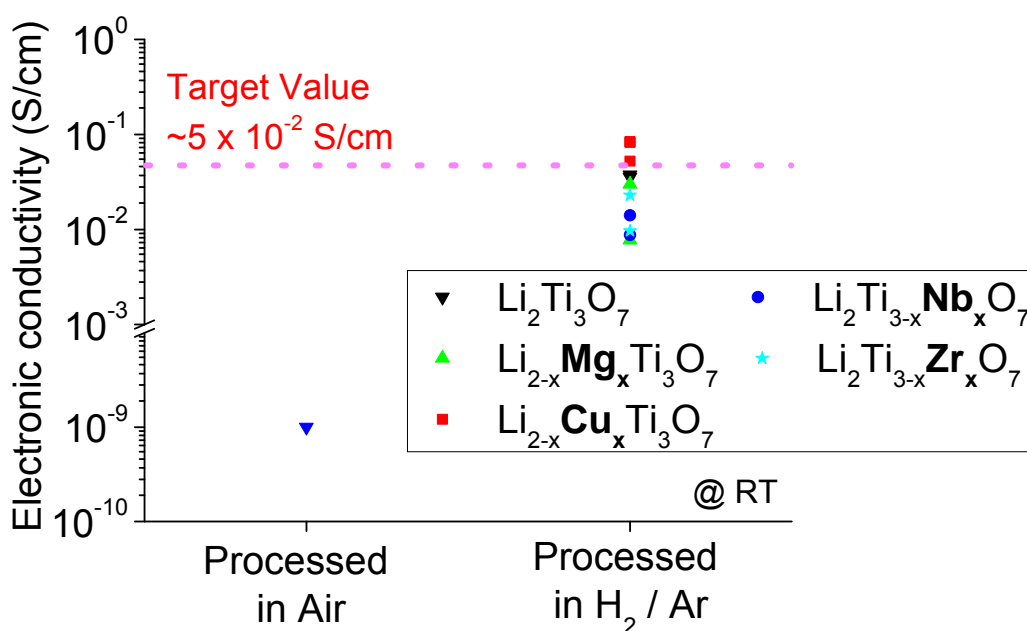
Figure 4.20. Electronic conductivity at room temperature for ramsdellite $Li_2Ti_3O_7$ doped with Mg, Cu, Nb, and Zr processed in air or reducing atmosphere

To understand the effect of Cu doping on electronic conductivity, activation energies for the Cu doped samples were calculated by measuring electronic conductivity at different temperatures with impedance spectroscopy. The activation energy for the undoped sample was also measured for the comparison. Figure 4.21

shows the electronic conductivity as a function of temperature for the undoped and Cu doped ramsdellite Li$_2$Ti$_3$O$_7$ with the calculated activation energies. The activation energies for the Cu doped ramsdellite Li$_2$Ti$_3$O$_7$ were significantly different from the undoped sample; the Cu doped samples ~ 0.10 eV and the undoped sample ~ 0.19 eV.
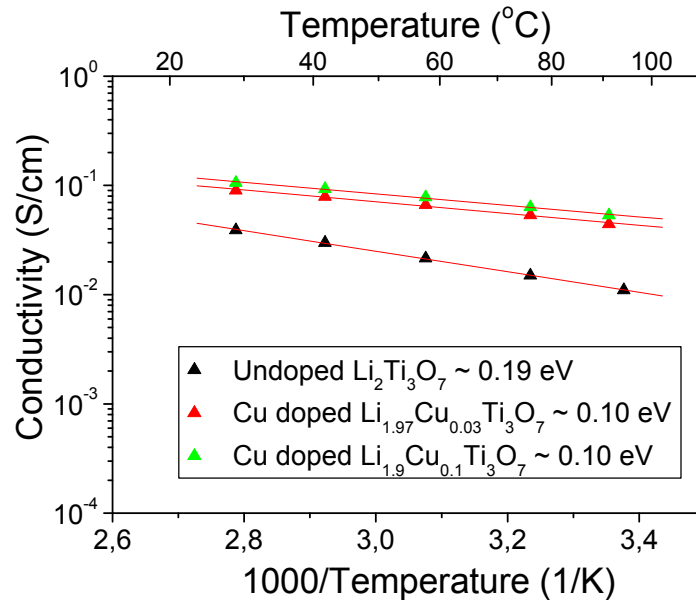
Figure 4.21. Electronic conductivity as a function of temperature for the undoped and Cu doped ramsdellite Li$_2$Ti$_3$O$_7$ processed in reducing atmosphere. The solid lines are fitted to an Arrhenius model. Measurements were performed in Ar atmosphere

4.2.3.2 Li-ion conductivity

The pellet processed in air resulted in a Li-ion conductivity of ~10^{-6} S/cm. Activation energy for Li-ion conduction was also calculated by measuring Li-ion conductivity at different temperatures. Figure 4.22 shows Li-ion conductivity multiplied by temperature as a function of temperature for undoped ramsdellite Li$_2$Ti$_3$O$_7$ with the calculated activation energy.
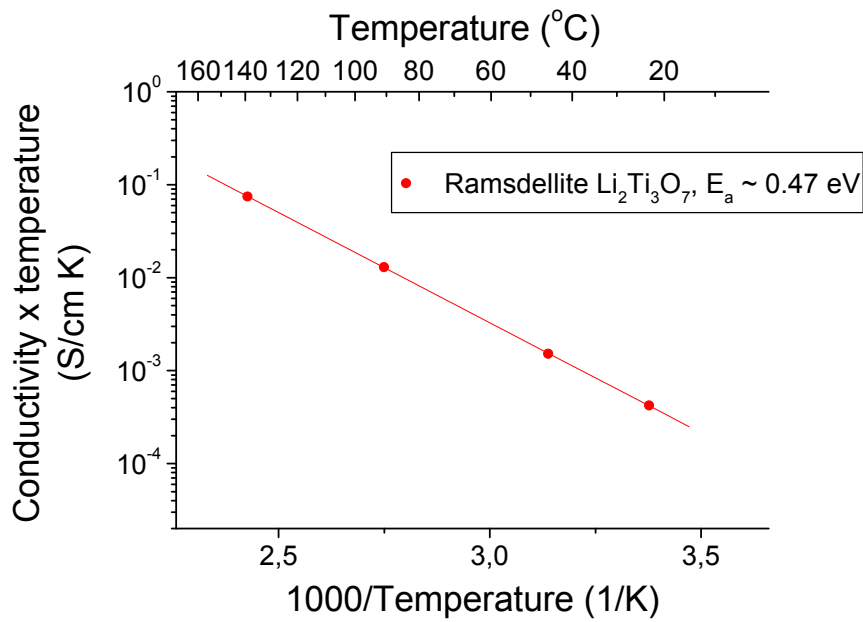
Figure 4.22 Li-ion conductivity multiplied by temperature as a function of temperature for undoped ramsdellite $Li_2Ti_3O_7$. The solid lines are fitted to an Arrhenius model

Figure 4.23 shows the Li-ion conductivity and activation energy for Li-ion conductivity of ramsdellite $Li_{2+x}Ti_3O_{7+x/2}$. Both the Li-ion conductivity and the activation energy did not change significantly with different x for $Li_{2+x}Ti_3O_{7+x/2}$.
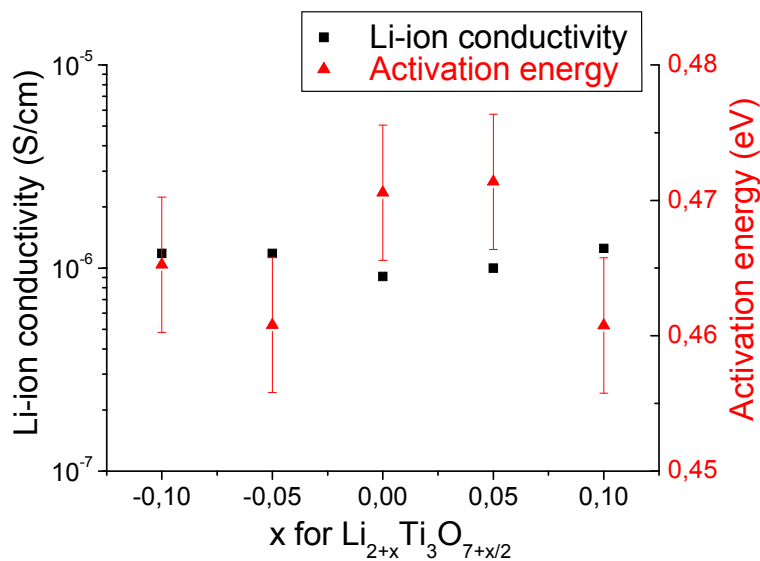
Figure 4.23. Li-ion conductivity at room temperature and activation energy for Li-ion conductivity as a function of x for ramsdellite $Li_{2+x}Ti_3O_{7+x/2}$

Figure 4.24 shows the Li-ion conductivity as a function of dopant concentration for ramsdellite Li$_2$Ti$_3$O$_7$ samples processed in air. The result shows that Li-ion conductivity did not increase with Mg, Cu, and Zr doping; the conductivity even decreased with Mg and Cu doping. The conductivity increased with Nb doping; the increase would be, however, not due to the bulk property, but likely due to the increase in the sample density. The reason why this is considered to be the case is discussed in section 5.2.2.2.
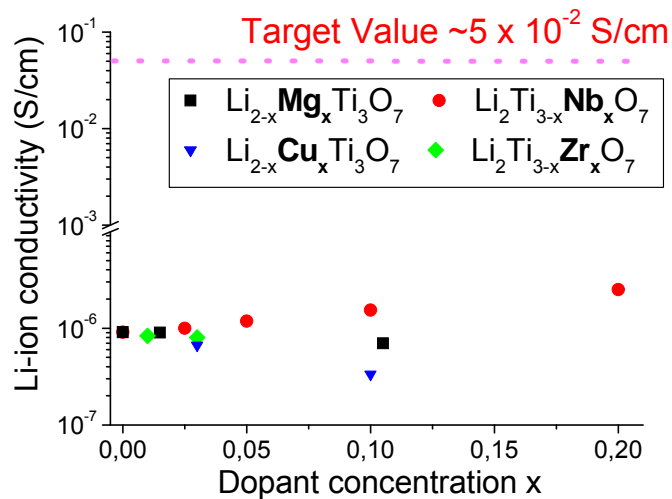
Figure 4.24. Li-ion conductivity at room temperature as a function of dopant concentration for doped ramsdellite Li$_2$Ti$_3$O$_7$ samples processed in air

Li-ion conductivity in the samples processed in reducing atmosphere was not measured due to the same problems as discussed in section 4.1.3.2.1 for the spinel Li$_{4/3}$Ti$_{5/3}$O$_4$ samples.

4.3 Li insertion into spinel $Li_{4/3}Ti_{5/3}O_4$ ceramics

4.3.1 Compositions

As explained in section 2.3.4, Li can be inserted into spinel $Li_{4/3}Ti_{5/3}O_4$ to transform to rock salt derived $Li_{7/3}Ti_{5/3}O_4$; $Li_{4/3+x}Ti_{5/3}O_4$ with x = 0 for spinel and x = 1 for rock salt derived structure. The Li insertion, $Li_{4/3+x}Ti_{5/3}O_4$ with $0 \leq x \leq 1$, was performed either chemically or electrochemically to confirm if the Li insertion increases electronic and Li-ion conductivity in the material or not.

4.3.2 Structural characterization

Spinel $Li_{4/3}Ti_{5/3}O_4$ and rock salt derived $Li_{7/3}Ti_{5/3}O_4$ have the same Fd-3m structure and almost the same lattice parameter: a = 8.3595 Å for $Li_{4/3}Ti_{5/3}O_4$ and 8.3538 Å for $Li_{7/3}Ti_{5/3}O_4$ [Sch99]. The same structure with similar lattice parameters makes it difficult to distinguish the two compounds with standard XRD. It has been shown that neutron diffraction [Wag06] or high resolution XRD at high angles [Sch99] can distinguish the two compounds. With the machine employed in this study, however, it was impossible to distinguish spinel $Li_{4/3}Ti_{5/3}O_4$ and rock salt derived $Li_{7/3}Ti_{5/3}O_4$.

4.3.3 Electrochemical Li insertion

Electrochemical Li insertion into Spinel $Li_{4/3}Ti_{5/3}O_4$ was performed in Swagelok[®] cells. Isostatically pressed pellets processed in air without sintering, sintered pellets processed in air, and sintered pellets processed in reducing atmosphere were tested. Figure 4.25 (a) shows a typical voltage profile for the pressed pellets during 1st discharge with C rate of ~C/100, and Figure 4.25 (b) and (c) shows voltage profiles with a C rate of ~C/500 for the pellet sintered in air and reducing atmosphere, respectively. The theoretical capacity was calculated for the reaction from spinel $Li_{4/3}Ti_{5/3}O_4$ to rock salt derived $Li_{7/3}Ti_{5/3}O_4$. Although the pressed pellets achieved close to 100 % theoretical capacity, the sintered pellets processed in air and reducing atmosphere achieved only about 0.3 % and 20 % theoretical capacity, respectively. Both pressed and sintered pellets processed in air changed the color from white to blue after Li insertion, as shown in Figure 4.26 for the pellet sintered in air.
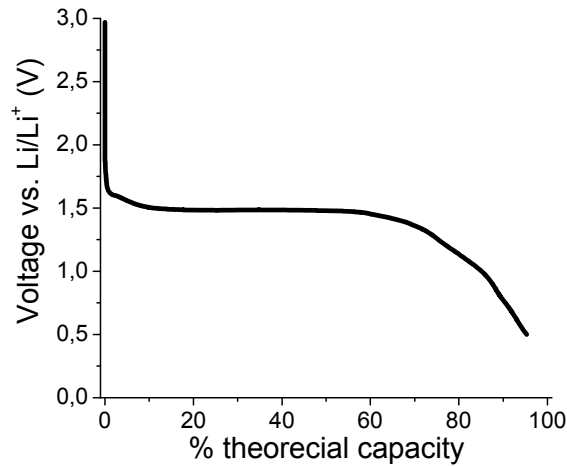
(a)
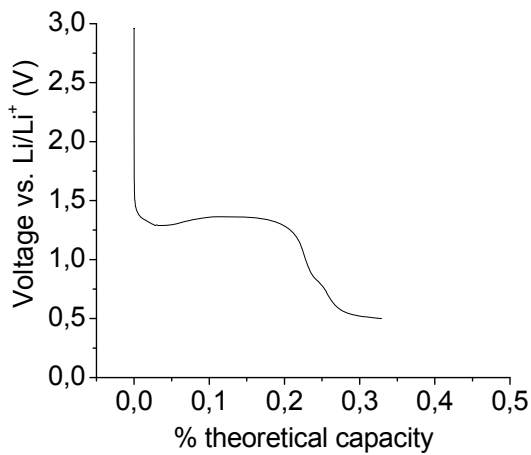
(b)
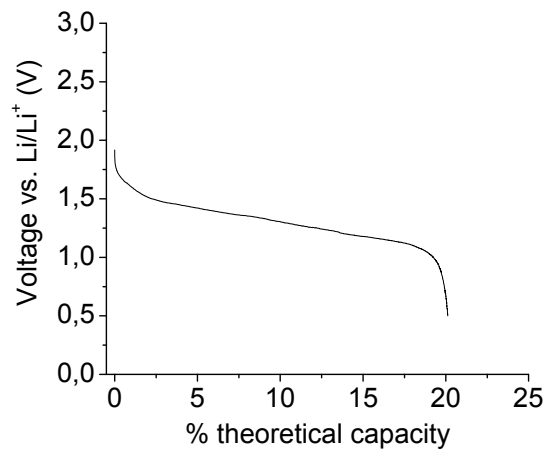
(c)

Figure 4.25. Voltage profile for the cell with (a) pressed spinel Li$_{4/3}$Ti$_{5/3}$O$_4$ processed in air during 1st discharge with a C rate of ~C/100, sintered spinel Li$_{4/3}$Ti$_{5/3}$O$_4$ processed in air (b) and reducing atmosphere (c) during 1st discharge with a C rate of ~C/500

(a)
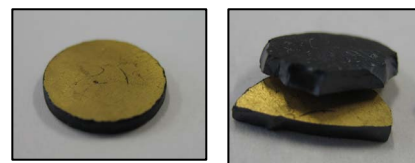
(b)

Figure 4.26. A sintered pellet processed in air (a) before and (b) after Li insertion. Gold was sputtered on one site of the pellet to serve as a current collector. The pellet was fractured for the cross section view

The cell with the pressed spinel $Li_{4/3}Ti_{5/3}O_4$ pellet was further cycled after the 1st discharge. Figure 4.27 shows the voltage profile for the 1st 3 cycles, and Table 4.3 shows % theoretical capacity for each discharge and charge step. The capacity degradation was observed during charge steps, especially during the 1st charge step (96 to 51 % theoretical capacity). The similar capacity degradation during the charge steps was observed for the pressed pellet of spinel $Li_{4/3}Ti_{5/3}O_4$ processed in reducing atmosphere.
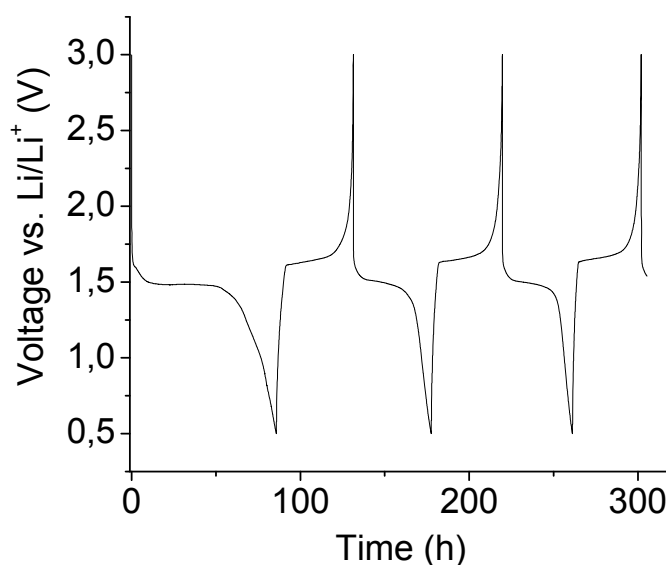
Figure 4.27. Voltage profile for the cell with pressed spinel $Li_{4/3}Ti_{5/3}O_4$ processed in air during 1st 3 cycles with C rate of ~C/100

Table 4.3. % theoretical capacity for the cell with pressed spinel $Li_{4/3}Ti_{5/3}O_4$ processed in air during 1st 3 cycles with C rate of ~C/100

Cycle	Charge or Discharge	% theorecical capacity
1	Discharge	96
	Charge	51
2	Discharge	52
	Charge	46
3	Discharge	46
	Charge	45

Electronic conductivity was measured to confirm if the Li insertion improves the conductivity or not. Figure 4.28 shows electronic conductivity as a function of

amount of Li inserted. For the measurement, the samples were taken out from the Swagelok® cell and Ag paste was applied on the both faces as electrodes. The amount of Li inserted was calculated from the experimental capacity and the theoretical capacity for the reaction from spinel $Li_{4/3}Ti_{5/3}O_4$ to rock salt derived $Li_{7/3}Ti_{5/3}O_4$. The electronic conductivity of the sintered pellet processed in air increased from 10^{-9} to 10^{-3} S/cm with the insertion amount of x ~ 0.003 for $Li_{4/3+x}Ti_{5/3}O_4$. The sample processed in reducing atmosphere showed better electronic conductivity already before the Li insertion, but the conductivity increased further with Li insertion.
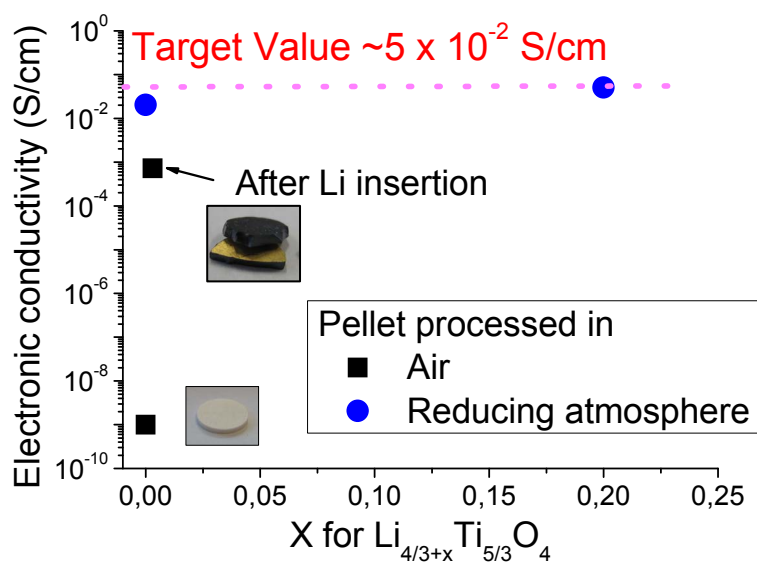
Figure 4.28. Electronic conductivity at room temperature as a function of amount of Li inserted. Li was inserted electrochemically into sintered pellet processed in air or reducing atmosphere

The change in Li-ion conductivity during the Li insertion is also of interest. Since electronic conductivity increased significantly with Li insertion, Li-ion conductivity could not be measured by impedance spectroscopy.

GITT (Galvanostatic Intermittent Titration Technique) [Wep77] was applied to check if Li-ion conductivity in the $Li_{4/3+x}Ti_{5/3}O_4$ could be obtained or not. GITT is an electrochemical method to estimate Li-ion conductivity of materials. Current pulses are applied on a cell and voltage responses are monitored. From the voltage responses, Li-ion diffusivity can be calculated. GITT is applicable only for a material

with a single phase reaction, where there is a change in equilibrium voltage with Li insertion [Wep77]. This condition limits the range of x for $Li_{4/3+x}Ti_{5/3}O_4$ where GITT can be applied, since the material shows the flat voltage profile (i.e. no change in equilibrium voltage) over the wide range of x.

GITT measurement was performed at the initial stage of Li insertion (x < 0.1 for $Li_{4/3+x}Ti_{5/3}O_4$) into spinel $Li_{4/3}Ti_{5/3}O_4$, where the change in equilibrium voltage was observed. GITT measurement did not supply reliable Li-ion diffusivity values. The values changed significantly with different experimental conditions such as pulse current, pulse time, and relaxation time between pulses. GITT assumes that the change in equilibrium voltage after each titration step is small. The voltage change at the initial stage of Li insertion into spinel $Li_{4/3}Ti_{5/3}O_4$, however, may be beyond the limit, where this assumption can be held.

The Li-ion conductivity measurement with electronically blocking electrode was performed on chemically Li inserted pellet and presented in section 4.3.4.

4.3.4 Chemical Li insertion

Li insertion into spinel $Li_{4/3}Ti_{5/3}O_4$ was also achieved chemically either by using Li metal or butyllithium.

Li-metal was applied directly on the both surfaces of the sintered spinel $Li_{4/3}Ti_{5/3}O_4$ pellets processed in air or in reducing atmosphere. The pellets processed in air changed the color from white to blue by the contact with Li-metal, as in Figure 4.29; the pellet turned into blue from the edge and completely blue within 7 days.

(a)   (b)

Figure 4.29. Pellets processed in air after contact with Li-metal for (a) 1 day and (b) 7 days

Figure 4.30 shows the change in electrical conductivity by the contact with Li-metal. The electronic conductivity of the pellet processed in air increased significantly in the 1st 100 hr and saturated to about 5 x 10^{-3} S/cm after 500 hr. The

sample processed in reducing atmosphere showed better electronic conductivity already before the contact with Li-metal, but the conductivity increased further with the Li insertion.
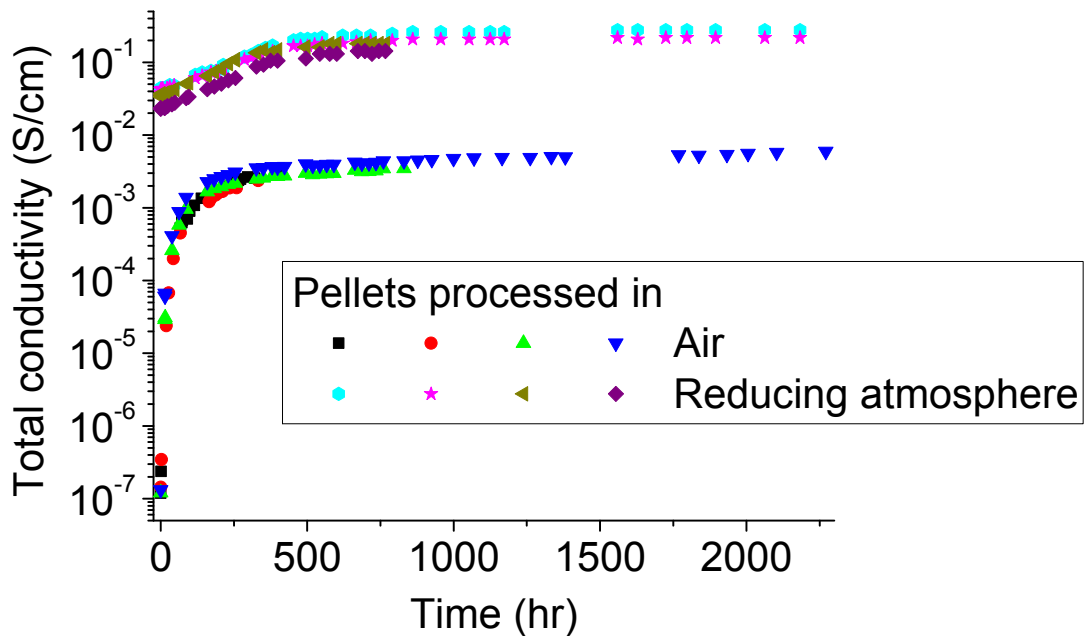

Figure 4.30. Electrical conductivity change in time by the contact with Li-metal. The different symbols and colors are for different samples

With Li-metal as electrodes, total conductivity (i.e. electronic + Li-ion conductivity) is measured. The separation of the electronic and Li-ion contribution on the conductivity is of interest. For that purpose, it was attempted to remove the Li-metal from the pellet and apply Ag paste to be able to measure only the electronic contribution. However, it was unsuccessful since it was difficult to remove Li-metal cleanly from the pellets.

In order to obtain the activation energy of the conduction, conductivities at different temperatures were measured. Figure 4.31 shows conductivity as a function of temperature for the 2 spinel $Li_{4/3}Ti_{5/3}O_4$ pellets processed in air after the contact with Li-metal for 500 hr. The calculated activation energies are also listed in Figure 4.31. The conduction was confirmed to be thermally activated.
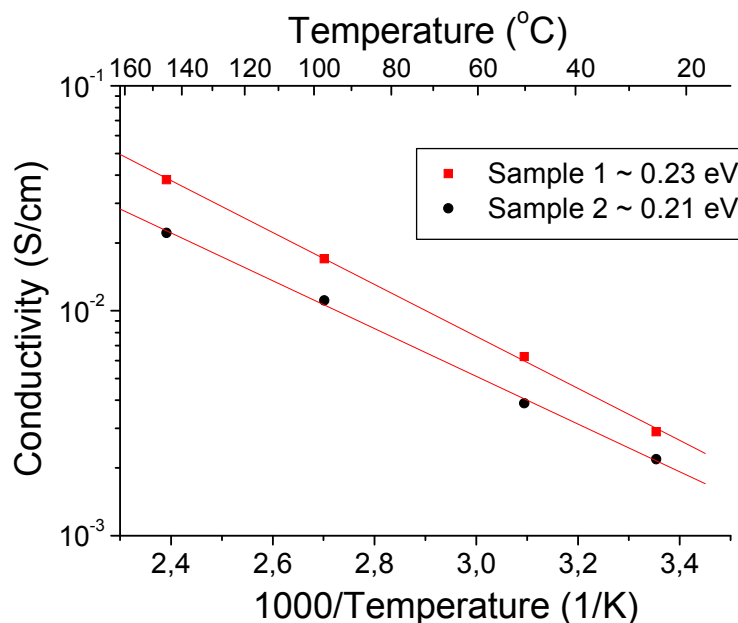
Figure 4.31. Electrical conductivity as a function of temperature for sintered spinel $Li_{4/3}Ti_{5/3}O_4$ samples processed in air after being in contact with Li-metal for 500 hr. The solid lines are fitted to an Arrhenius model. Measurements were performed in Ar atmosphere

Li was also inserted by dipping the spinel $Li_{4/3}Ti_{5/3}O_4$ samples in butyllithium. The amount of butyllithium was calculated to the desired Li insertion amount. Here, the results for the sintered pellets targeted for x = 0.5 for $Li_{4/3+x}Ti_{5/3}O_4$ are explained.

The pellet processed in air changed the color from white to blue, as shown in Figure 4.32. After a few minutes in butyllithium, the surface of the pellet started to change the color and the pellet completely turned into blue after 7 days.

(a)　　　　　　　　　　(b)　　　　　　　　　　(c)
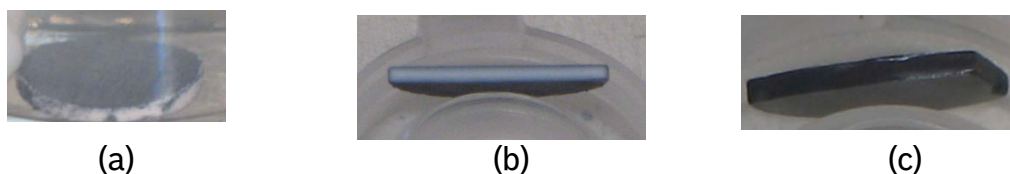
Figure 4.32. Sintered pellets processed in air in butyllithium after (a) a few minutes, (b) 12 hr, and (c) 7 days. Pellets in (b) and (c) were fractured for the cross section view

Figure 4.33 shows the change in electronic conductivity after 7 days in butyllithium. The sample processed in air and reducing atmosphere increased the conductivity up to 10^{-3} S/cm and 10^{-1} S/cm, respectively.
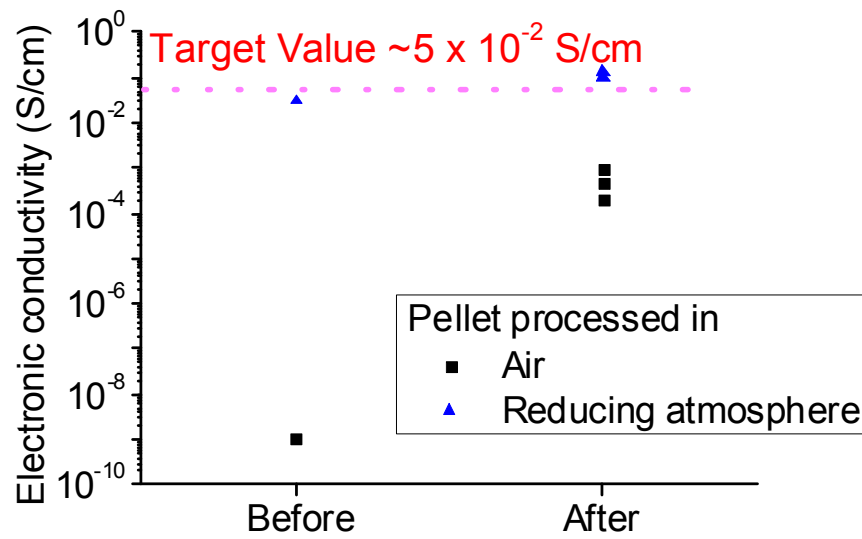
Figure 4.33. Electronic conductivity before the Li insertion and after 7 days in butyllithium.

Figure 4.34 shows the change in electronic conductivity with time in air of the spinel $Li_{4/3}Ti_{5/3}O_4$ pellet which was in butyllihium for 7 days targeted for x = 0.5 for $Li_{4/3+x}Ti_{5/3}O_4$. Within the first couple of hours, the electrical conductivity decreased significantly, down to 10^{-6} S/cm, and continuously further decreased down to 10^{-8} S/cm after 18 days. After 18 days, the pellet turned back to white completely.
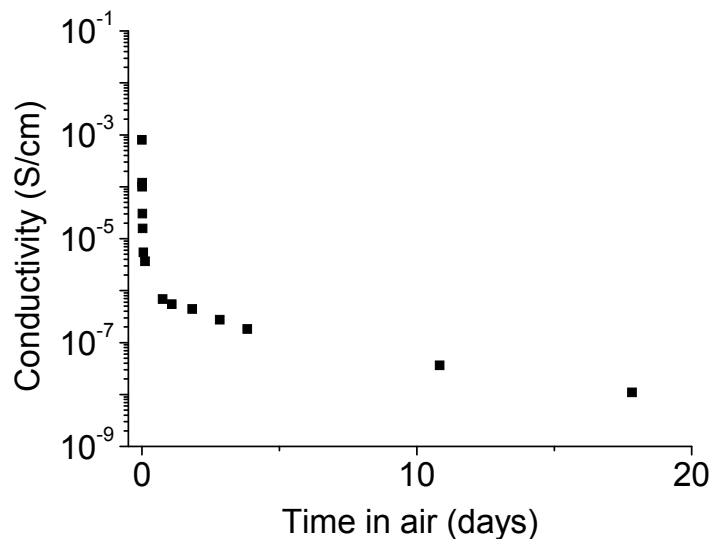
Figure 4.34. Electronic conductivity at room temperature as a function of time in air for the spinel $Li_{4/3}Ti_{5/3}O_4$ pellet which was in butyllihium for 7 days targeted for x = 0.5 for $Li_{4/3+x}Ti_{5/3}O_4$

Similar to the spinel $Li_{4/3}Ti_{5/3}O_4$ and the ramsdellite $Li_2Ti_3O_7$ samples prepared in reducing atmosphere, the high electronic conductivity in the Li inserted samples makes the Li-ion conductivity measurement difficult.

LiPON was sputtered on the both surfaces of the spinel $Li_{4/3}Ti_{5/3}O_4$ pellet which was in butyllihium for 7 days targeted for x = 0.5 for $Li_{4/3+x}Ti_{5/3}O_4$. Insulating ring tapes were placed on the surfaces to mask the samples for the desired geometry, as in Figure 4.35 (a) and (b). On the LiPON layers, Li-metal pieces smaller than the LiPON layers were placed for the desired sample geometry, as shown in Figure 4.35 (c). Figure 4.36 shows SEM micrographs of the samples. The SEM micrographs proofed that the LiPON layers are continuous with a thickness of 1.5 to 3.5 μm.

| (a) | (b) | (c) |
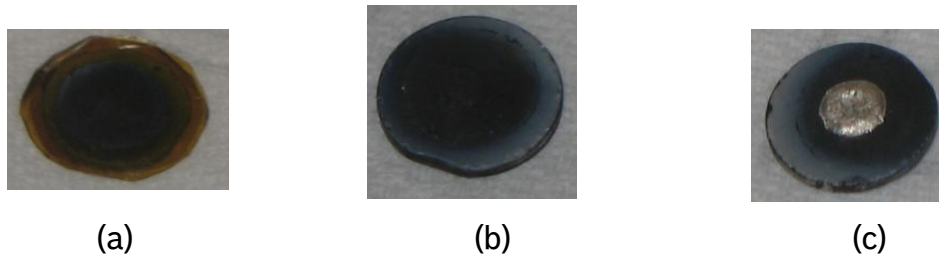
Figure 4.35. Pictures of the sample for Li-ion conductivity measurement with LiPON layer; (a) with insulating tape before LiPON sputtering, (b) after LiPON sputtering, and (c) with Li-metal.

(a) Cross section
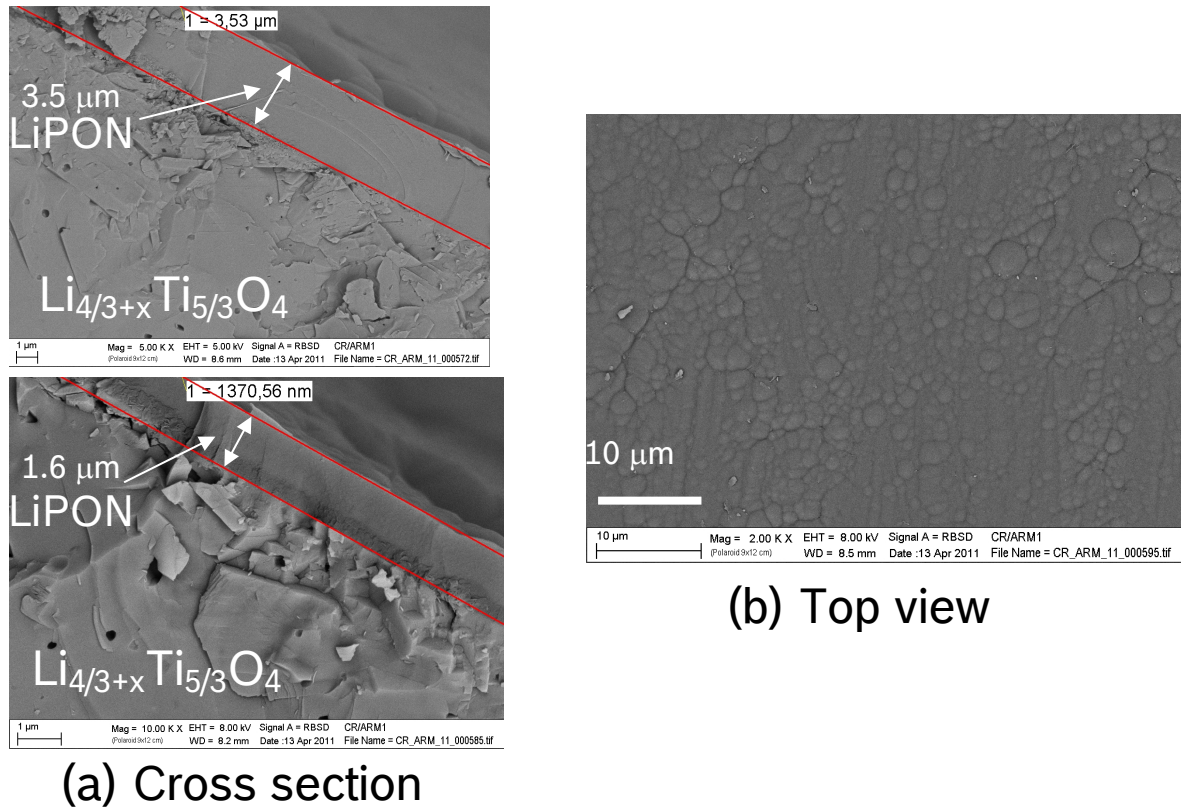
(b) Top view

Figure 4.36. SEM pictures of LiPON layers on $Li_{4/3+x}Ti_{5/3}O_4$ pellets, (a) cross section and (b) top view.

In order to obtain resistance of the sample, current from 0.01 to 2 mA was applied to the cell and the voltage response was monitored. Figure 4.37 and 4.38 show the result of the DC measurement: Figure 4.37 for the applied current and the voltage response as a function of time, Figure 4.38 for conductivity as a function of the applied current. Conductivity was calculated with the sample geometry by taking the voltage at the end of each current step, with the assumption that all of the resistance is due to the $Li_{4/3+x}Ti_{5/3}O_4$ samples. The Li-ion conductivity values from 10^{-5} to 10^{-3} S/cm were observed, which are higher than that of the material without Li insertion, spinel $Li_{4/3}Ti_{5/3}O_4$.
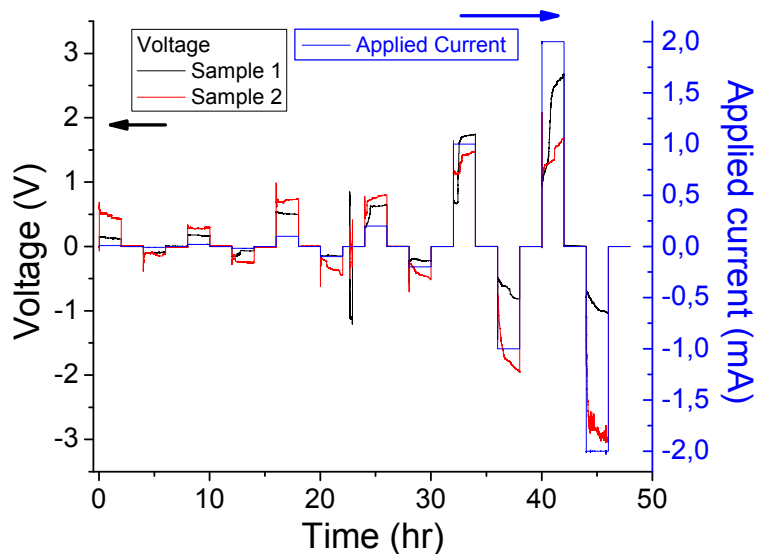
Figure 4.37. Applied current and the voltage response as a function of time
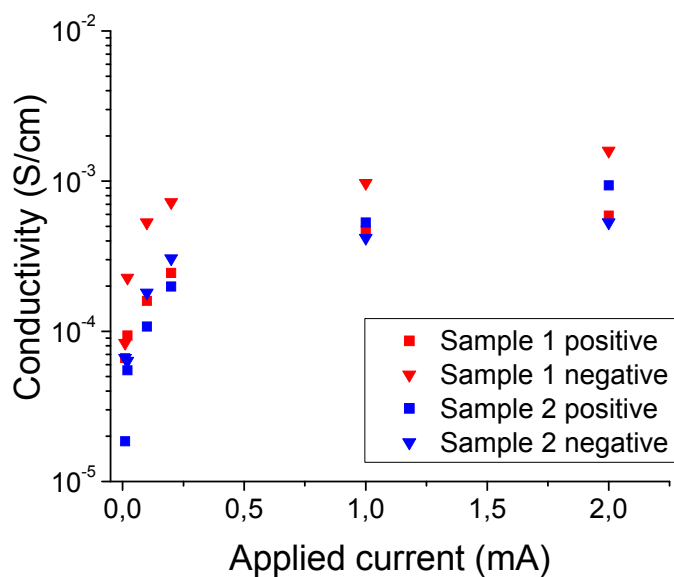
Figure 4.38. Conductivity as a function of applied current. The results from 2 different cells for positive and negative current direction are shown

The Li-ion conductivity values from 10^{-5} to 10^{-3} S/cm were estimated from the measurement with the LiPON layers with the assumption that all the resistance measured was due to the $Li_{4/3+x}Ti_{5/3}O_4$ samples. The electronic and Li-ion conduction in the LiPON layers should also be considered for the estimation to be correct.

The conductivity measurement with LiPON may provide not Li-ion conductivity but electronic conductivity if the LiPON layer is not a good electronic insulator. To confirm if the LiPON layer was a good electronic insulator or not, the measurement with Ag electrodes instead of Li-metal electrodes was also performed. Ag is an electronically conducting and Li-ion blocking electrode, so high resistance should be observed if the LiPON layer is a good electronic insulator. About 3 orders of magnitude higher resistance was observed with Ag electrodes than with Li-metal electrodes. This is the proof that the LiPON layer was a good electronic insulator and Li-ion conductivity was measured with Li-metal electrodes.

In order to calculate the Li-ion conductivity in Figure 4.38, the resistance only from the $Li_{4/3+x}Ti_{5/3}O_4$ was considered. However, the resistance of the LiPON layers may be a limiting factor for the Li-ion conductivity; therefore it needs to be considered. From the geometry and the Li-ion conductivity value of LiPON as 10^{-6} S/cm from literature [Ham06], the resistance of 2000-6000 ohm is expected from the LiPON layers. This is in the same order of magnitude which was observed during the measurement. This result suggests that the measured resistance may be dominated not by the $Li_{4/3+x}Ti_{5/3}O_4$ but by the LiPON layers. If this is the case, Li-ion conductivity of the $Li_{4/3+x}Ti_{5/3}O_4$ can be estimated to be higher than 10^{-4} S/cm since the thickness of the $Li_{4/3+x}Ti_{5/3}O_4$ is 100-300 times thicker than the LiPON layers.

4.4 Fe doped spinel $Li_{4/3}Ti_{5/3}O_4$ ceramics

4.4.1 Compositions

For the Fe doped spinel $Li_{4/3}Ti_{5/3}O_4$ system, the samples with the following nominal compositions were prepared. The compositions were chosen to be close to y = 0.16, the composition shown in section 2.5 with the promising Li-ion conductivity. The two compositions with the different crystal structures around y = 0.16 were chosen from the phase diagram (Figure 2.13); one with Fd-3m and the other with $P4_332$.

Thus the compositions studied were:

$Li_{4/3-y/3}Fe_yTi_{5/3-2y/3}O_4$, with y = 0.115 and 0.25

4.4.2 Structural characterization

Figure 4.39 (a) shows the XRD patterns after sintering of the Fe doped spinel $Li_{4/3}Ti_{5/3}O_4$ samples processed in air. Note that the sample with y=0.25 for $Li_{4/3-y/3}Fe_yTi_{5/3-2y/3}O_4$ was sintered at 850 ^{o}C, instead of the standard process at 950 ^{o}C. The sample with x = 0.25 showed a large amount of the ramsdellite phase when sintered at 950 ^{o}C. The samples with y = 0.115 and 0.25 resulted in different structures; Fd-3m structure and $P4_332$ structure, respectively. (ICSD #84971[FIZ11] for $P4_332$)

Figure 4.39 (b) shows the magnified XRD patterns of the (220) peak. Similar to the Mg doped spinel samples in section 4.2.2, the increase in the intensity of the peak was observed with Fe doping, indicating that more Fe ions sit on the tetrahedral Li site with increasing Fe concentration.
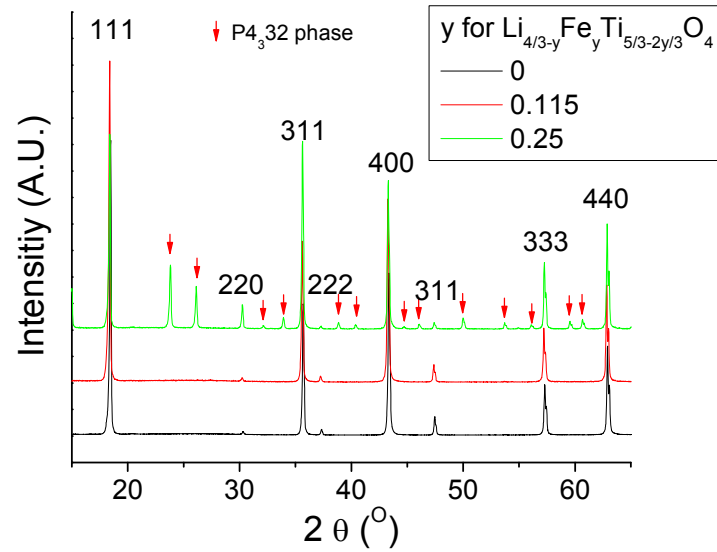
(a)
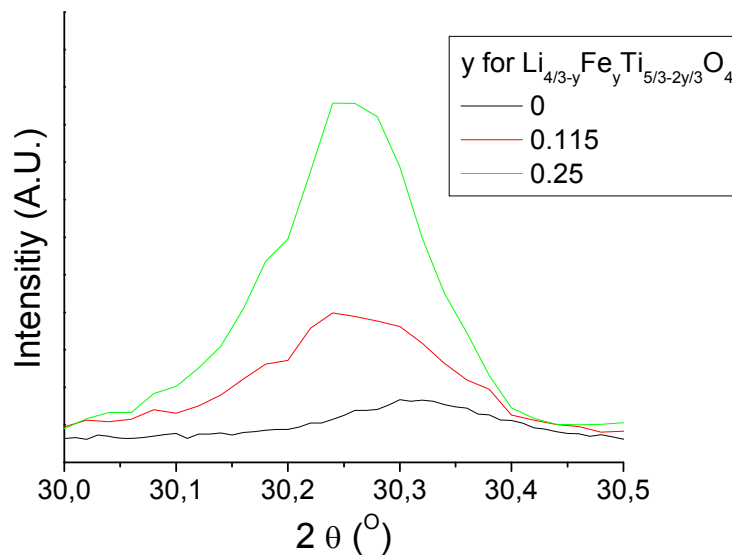
(b)

Figure 4.39. X-ray diffraction patterns (a) 15-65° (b) 30-30.5° of Fe doped spinel ceramics, $Li_{4/3-y/3}Fe_yTi_{5/3-2y/3}O_4$, with y = 0, 0.115, and 0.25, processed in air. The indexing is based on cubic spinel unit cells

Figure 4.40 shows the XRD patterns of the Fe doped spinel $Li_{4/3}Ti_{5/3}O_4$ samples after calcination and sintering in reducing atmosphere. Calcination in 10 % H_2, 90 % Ar resulted in the appearance of elemental Fe and Li_2TiO_3. After sintering in Ar, both samples with y = 0.115 and 0.25 indicated an almost pure spinel phase with little Li_2TiO_3, but a finite amount of elemental Fe was still observed.
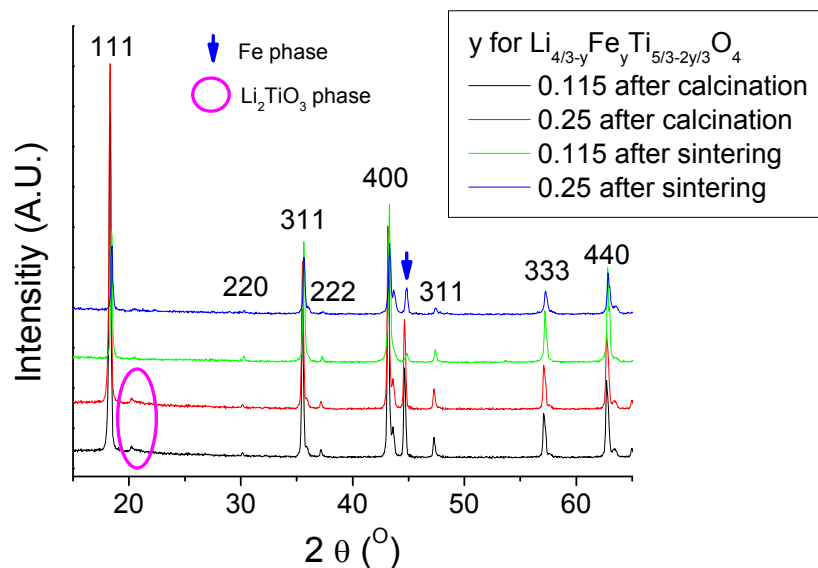
Figure 4.40. X-ray diffraction patterns after calcination and sintering of Fe doped spinel ceramics, $Li_{4/3-y/3}Fe_yTi_{5/3-2y/3}O_4$, with y = 0.115, and 0.25, processed in reducing atmosphere. The indexing is based on cubic spinel unit cells

4.4.3 Electrical characterization

Figure 4.41 shows the electronic conductivity for Fe doped samples processed in air or reducing atmosphere. When processed in air, similar to the Cu doped sample, Fe doping on spinel $Li_{4/3}Ti_{5/3}O_4$ resulted in the brownish color after sintering, as shown in Figure 3.4 and increased the conductivity slightly (~ 4 x 10^{-8} S/cm with y = 0.25 for $Li_{4/3-y/3}Fe_yTi_{5/3-2y/3}O_4$). The conductivity was measured by impedance spectroscopy, so the value may account for either electronic or Li-ion conductivity. The reason why this is considered to be electronic conductivity is discussed in section 5.5.2.

When processed in reducing atmosphere, the Fe doped samples showed no obvious increase in electronic conductivity compared with the undoped spinel $Li_{4/3}Ti_{5/3}O_4$. Figure 4.42 shows an electronic conductivity as a function of temperature for the undoped and Fe doped spinel $Li_{4/3}Ti_{5/3}O_4$ with the calculated activation energies. The activation energies for Fe doped spinel $Li_{4/3}Ti_{5/3}O_4$ were similar to the undoped spinel $Li_{4/3}Ti_{5/3}O_4$, ~ 0.2 eV.
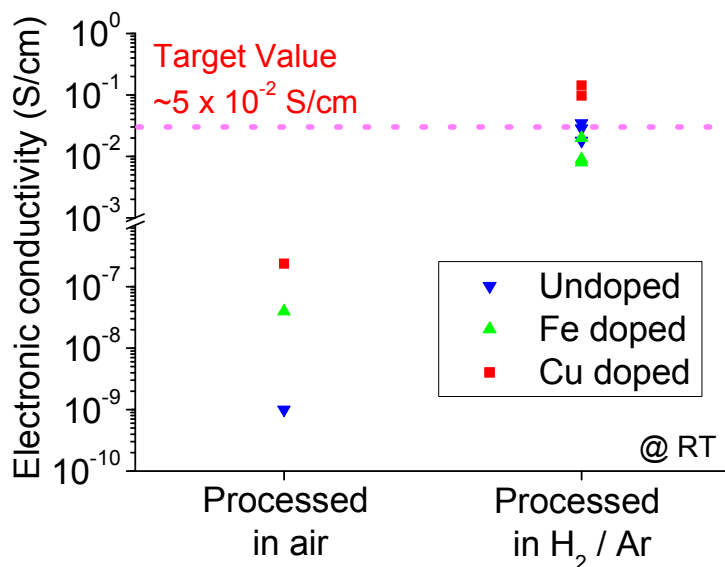
Figure 4.41. Electronic conductivity at room temperature for spinel Li$_{4/3}$Ti$_{5/3}$O$_4$ doped with Fe processed in air or reducing atmosphere (10 % H$_2$ 90 % Ar for calcination and 100 % Ar for sintering). Undoped and Cu doped spinel Li$_{4/3}$Ti$_{5/3}$O$_4$ are also shown for comparison
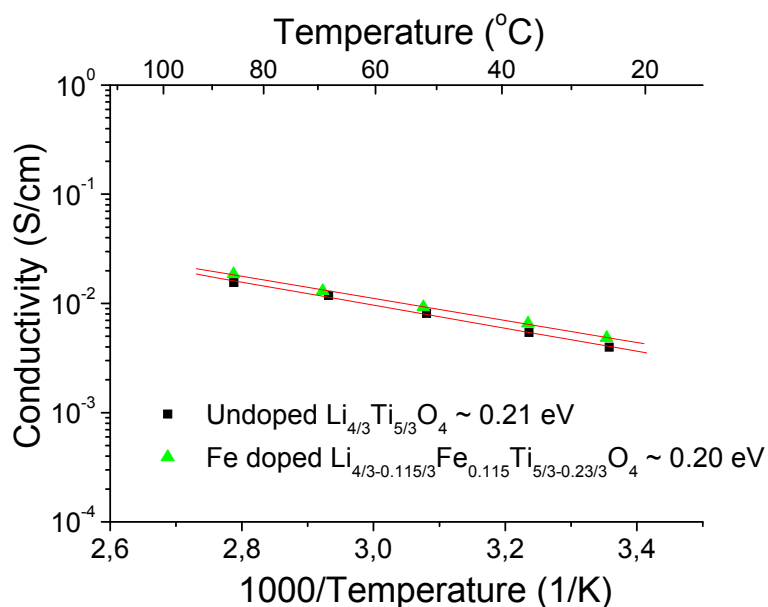
Figure 4.42. Electronic conductivity as a function of temperature for the undoped and Fe doped spinel Li$_{4/3}$Ti$_{5/3}$O$_4$ processed in reducing atmosphere. The solid lines are fitted to an Arrhenius model. Measurements were performed in Ar atmosphere

4.4.4 Electrochemical and chemical Li insertion

Figure 4.43 (a) and (b) show typical voltage profiles for the pressed pellets from the Fe doped spinel $Li_{4/3-y/3}Fe_yTi_{5/3-2y/3}O_4$ processed in air and reducing atmosphere for the initial discharge steps, respectively. The test was performed with the cycles with 1hr discharge with C rate of ~C/100, followed by a 71 hr pause for the samples processed in air and 23 hr pause for the samples processed in reducing atmosphere. Even after 71 hr pauses, the voltages of the cells with the Fe doped samples processed in air were not saturated.   On the other hand, the voltage of the cells with the Fe doped samples processed in reducing atmosphere was saturated in 23 hr for the most of the steps.

Figure 4.44 (a) and (b) show voltage profiles as a function of amount of Li inserted for the pressed pellets from the Fe doped spinel $Li_{4/3-y/3}Fe_yTi_{5/3-2y/3}O_4$ processed in air and reducing atmosphere, respectively. The voltages after 71 or 23 hr pause steps are plotted. The amount of Li inserted was calculated from the experimental capacity and the theoretical capacity for the reaction from x = 0 to 1 for $Li_{4/3-y/3+x}Fe_yTi_{5/3-2y/3}O_4$. The Fe doped samples processed in air resulted in a higher voltage than the undoped sample, and the voltages of the Fe doped samples decreased continuously. The samples processed in reducing atmosphere showed no obvious differences between the Fe doped samples and the undoped sample. The samples showed the short shoulders at 1.6-2.2 V at the beginning, followed by the stable plateaus at about 1.5 V.
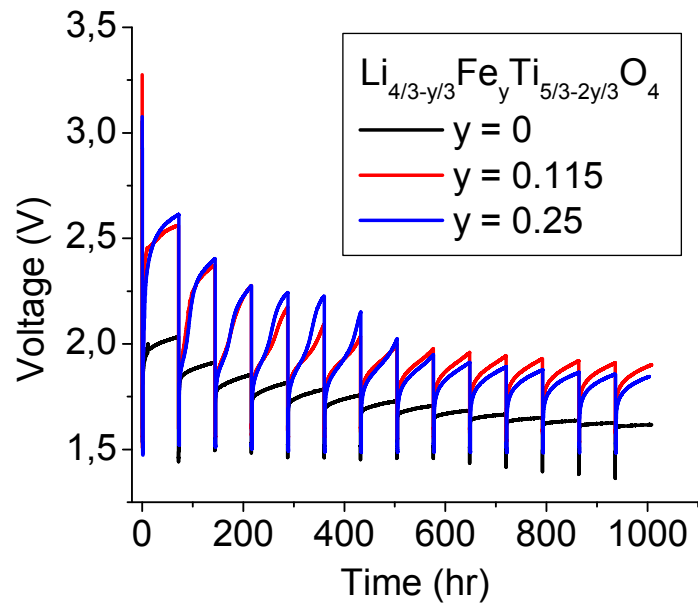
(a)
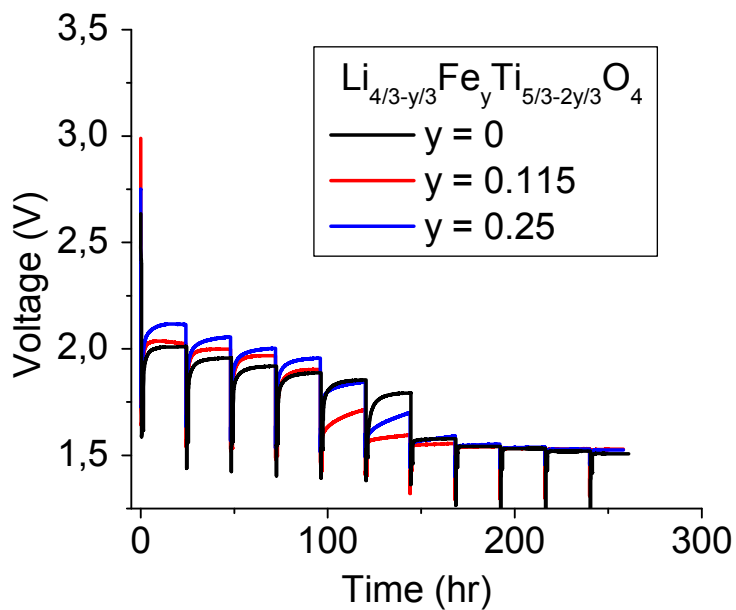
(b)

Figure 4.43. Voltage profiles for the cell with pressed Fe doped spinel $Li_{4/3-y/3}Fe_yTi_{5/3-2y/3}O_4$ processed in (a) air and (b) reducing atmosphere
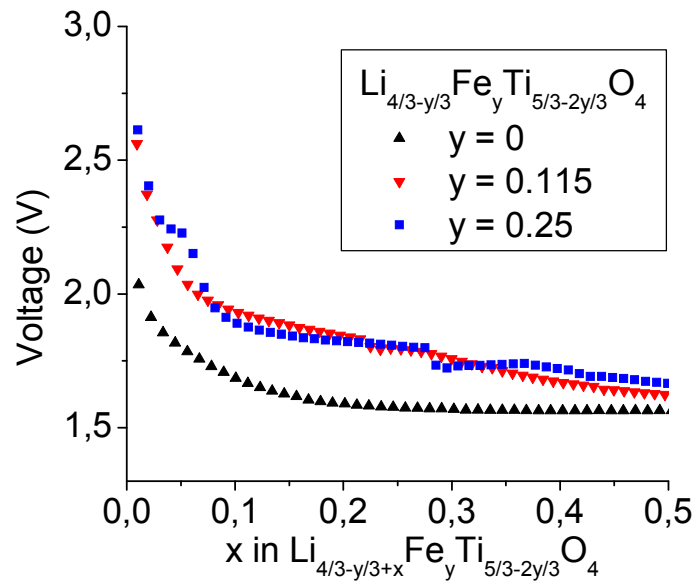
(a)
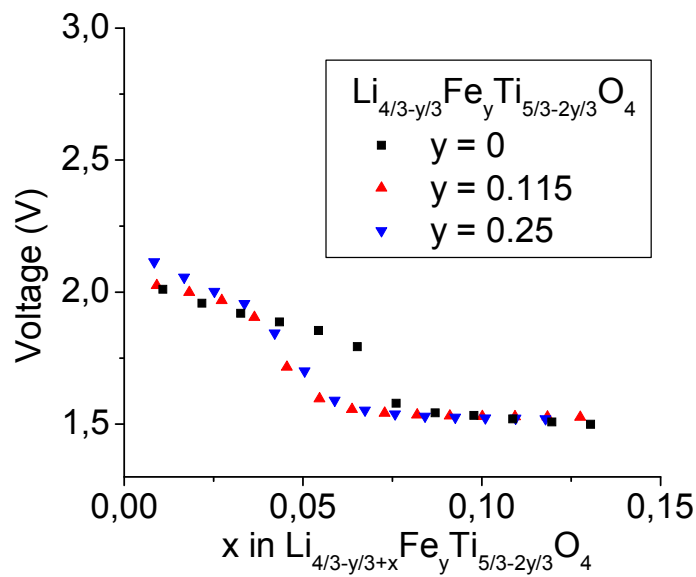
(b)

Figure 4.44. Voltage profiles as a function of amount of Li inserted for the pressed pellets from the Fe doped spinel $Li_{4/3-y/3}Fe_yTi_{5/3-2y/3}O_4$ processed in (a) air and (b) reducing atmosphere

Li-metal was applied on the both surfaces of the sintered Fe doped spinel $Li_{4/3-y/3}Fe_yTi_{5/3-2y/3}O_4$ pellets processed in air or in reducing atmosphere. Figure 4.45 shows the change in color of the pellets processed in air; the color changed from brown to black with time and the pellet turned into black within 50 days completely.

(a)	(b)	(c)	(d)
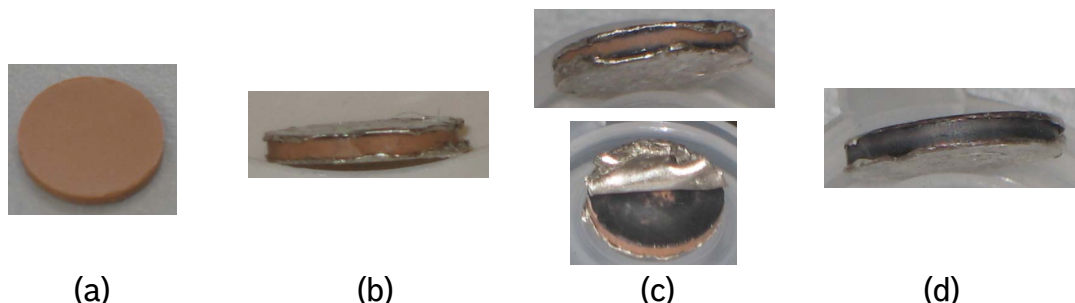
Figure 4.45. Fe doped pellets, $Li_{4/3-y/3}Fe_yTi_{5/3-2y/3}O_4$, with y = 0.115, processed in air after contact with Li-metal for (a) 0 day, (b) 1 day, (c) 7 days, and (d) 50 days

Figure 4.46 shows the change in electrical conductivity by the contact with Li-metal. The electronic conductivity of the pellets processed in air increased from 10^{-8} S/cm to $10^{-7} \sim 10^{-6}$ S/cm slowly in the first 500 hr and then increased rapidly up to 10^{-1} S/cm after 750-1500 hr, depending on the samples. The sample processed in reducing atmosphere showed better electronic conductivity already before the contact with Li-metal, but the conductivity increased further with Li insertion.
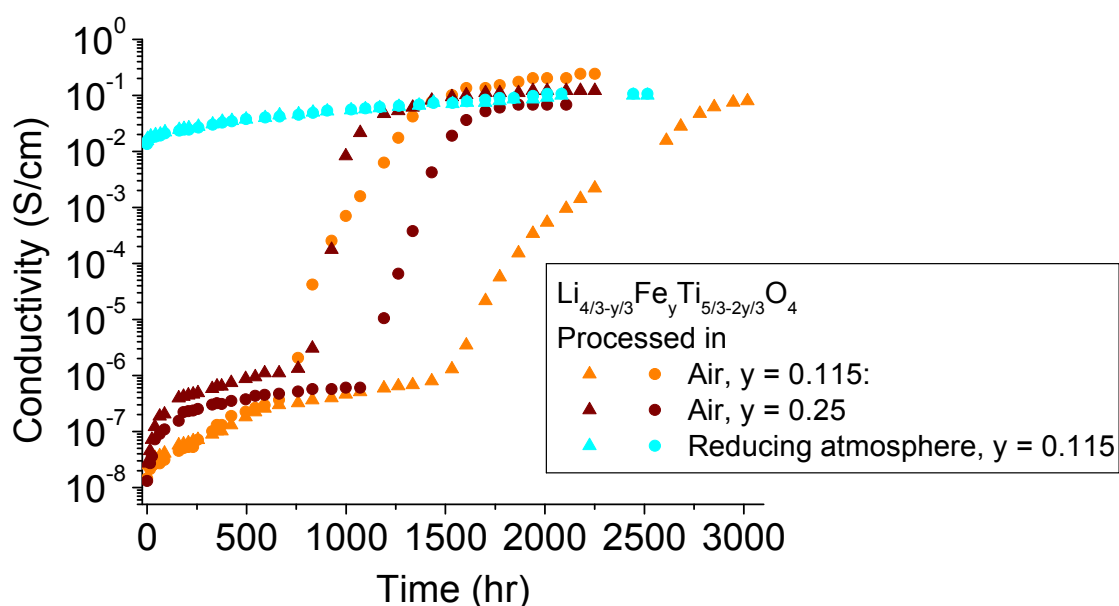
Figure 4.46. Electrical conductivity change with time by the contact with Li-metal for the Fe doped samples, $Li_{4/3-y/3}Fe_yTi_{5/3-2y/3}O_4$. The triangle and circle symbols represent different samples from the same composition and process condition.

Chapter 5: Discussion

5.1 Spinel $Li_{4/3}Ti_{5/3}O_4$ ceramics

5.1.1 Structural characterization

As shown in Figure 4.2, the sample with 3 wt% excess Li_2CO_3 resulted in the phase pure spinel $Li_{4/3}Ti_{5/3}O_4$. The appearance of the second phase with 1 and 5 wt% excess Li_2CO_3 suggests no (or a very limited) solid solution range of spinel $Li_{4/3}Ti_{5/3}O_4$. This agrees with the phase diagram in literature, which suggests that a slight off-stoichiometry from spinel $Li_{4/3}Ti_{5/3}O_4$ composition would result in TiO_2 or Li_2TiO_3 as a second phase [Izq80].

The undoped spinel $Li_{4/3}Ti_{5/3}O_4$ sample processed in reducing atmosphere had a significant amount of Li_2TiO_3 phase (up to 7 wt %). Many of the doped $Li_{4/3}Ti_{5/3}O_4$ samples also showed up to 7 wt % TiO_2 or Li_2TiO_3 phase. The existence of the TiO_2 or Li_2TiO_3 phase would be a result of off-stoichiometry introduced by reducing atmosphere or the doping. The appearance of Li_2TiO_3 in the samples processed in reducing atmosphere suggests that the Li loss during sample preparation in reducing atmosphere may be less than in air. TiO_2 may be the result of Ti vacancies created by the dopants (see chapter 5.1.2.1 for detail discussion on Mg doping). By changing the amount of excess Li_2CO_3, phase pure spinel $Li_{4/3}Ti_{5/3}O_4$ samples could be prepared also in reducing atmosphere or with the dopants, but such tuning was not performed.

As Table 4.1 shows, different dopants had different solubilities. The relatively large solubilities of Mg and Cu ions (x = 0.15 and 0.1 confirmed in air, respectively) are due to that fact that the ion sizes are similar to that of Li (Mg^{2+} and Cu^{2+}: 0.57 Å, Li^{1+}: 0.59 Å for tetrahedral coordination [Sha76]). On the other hand, no or only small solubilities (up to 0.03 in air) of Ca, Nb, Ta, and Zr ions can be attributed to the large ionic sizes of the dopants, which would be too big for the octahedral sites in spinel $Li_{4/3}Ti_{5/3}O_4$.

The linear increase in the lattice parameter with the increasing dopant concentration was observed, except in the case of Ca doping, which did not show any solubility. The linear behavior is consistent with Vegard's law, confirming a solid solution [Veg21]. The solubility limit of Mg doping was estimated based on the deviation from Vegrad's law for the sample with x = 0.2, as shown in Figure 5.1. The result indicates that the solubility limit of Mg in spinel $Li_{4/3-x}Mg_xTi_{5/3}O_4$ is about x = 0.17, which agrees well with the data in literature [Che01]. This estimated solubility

limit coincides with both the XRD result (Figure 4.4), which showed no 2nd phase for x = 0.15 but a clear 2nd phase for x = 0.20, and the (220) peak result (Figure 4.6), which showed more Mg ions sitting on the tetrahedral sites for x = 0.20 than 0.15. The amount of Mg ions on the tetrahedral sites would have increased until the solubility limit of x = 0.17 was reached.
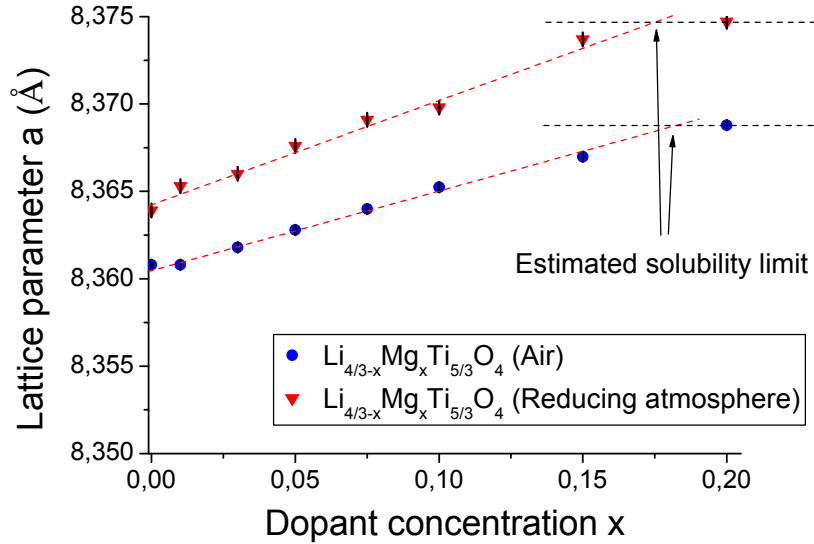
Figure 5.1. Lattice parameter as a function of dopant concentration for Mg doped spinel Li$_{4/3}$Ti$_{5/3}$O$_4$ samples processed in air and reducing atmosphere (10 % H$_2$ 90 % Ar for calcination and 100 % Ar for sintering). Lattice parameters were calculated by Rietvelt analysis of XRD data

5.1.2 Electric properties

5.1.2.1 Electronic conductivity

The increase in electronic conductivity by processing the material in reducing atmosphere may be explained well by defect chemistry. In spinel Li$_{4/3}$Ti$_{5/3}$O$_4$, oxygen vacancies can be compensated by the change in the oxidation state of titanium ions from 4$^+$ to 3$^+$ through the following equation 5.1 or compensated by extra electrons through equation 5.2,

$$Li_{4/3}Ti_{5/3}^{IV}O_4 \xrightarrow{reducing \quad atmosphere} Li_{4/3}Ti_{5/3-x}^{IV}Ti_x^{III}O_{4-\frac{x}{2}} + \frac{x}{4}O_2(g) \qquad (5.1)$$

$$Li_{4/3}Ti_{5/3}^{IV}O_4 \xrightarrow{reducing \quad atmosphere} Li_{4/3}Ti_{5/3}^{IV}O_{4-\frac{x}{2}} + x\,e^- + \frac{x}{4}O_2(g) \qquad (5.2)$$
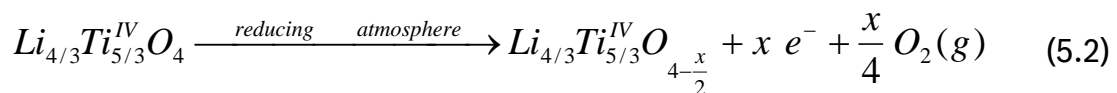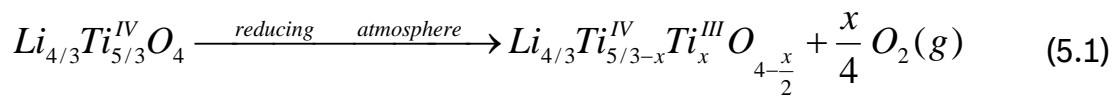
Either Ti^{3+} ions or the extra electrons, or both of them would be responsible for the increase in the electronic conductivity in spinel $Li_{4/3}Ti_{5/3}O_4$ processed in reducing atmosphere. The mixed valence state of Ti ions (Ti^{3+} and Ti^{4+}) may lead to good electron hopping conduction. The extra electrons created by oxygen vacancies are also known to often contribute to electronic conductivity in oxide materials by creating an energy level near a conduction band, similar to n-type semiconductors (section 2.2.1).

The existences of Ti^{3+} ions or extra electrons associated with oxygen vacancies could also explain the degradation in electronic conductivity in air. Oxygen in air is diffused into the material to fill the oxygen vacancy, which simultaneously changes the valency of Ti ions back to +4, or fill the oxygen vacancies by utilizing the extra electrons, according to the following equations:

$$Li_{4/3}Ti_{5/3-x}^{IV}Ti_{x}^{III}O_{4-\frac{x}{2}} + \frac{x}{4}O_2(g) \xrightarrow{\quad in \quad air \quad} Li_{4/3}Ti_{5/3}^{IV}O_4 \qquad (5.3)$$

$$Li_{4/3}Ti_{5/3}^{IV}O_{4-\frac{x}{2}} + x\ e^- + \frac{x}{4}O_2(g) \xrightarrow{\quad in \quad air \quad} Li_{4/3}Ti_{5/3}^{IV}O_4 \qquad (5.4)$$
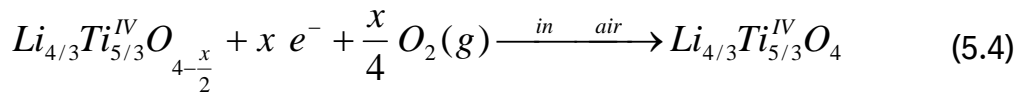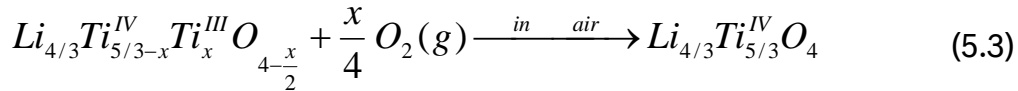
After polishing the surface and re-electroding, the degraded electronic conductivity was partially recovered, ~ 10^{-3} S/cm as shown in Figure 4.8. The value was not as high as the initial conductivity but close to it, suggesting that the degradation occurs severely in the surface layer of the pellet. This result could be explained by a slow diffusion of oxygen into the structure to fill the oxygen vacancies.

Conductivity measurements in air and Ar atmosphere were performed to confirm if there are oxygen vacancies in the material processed in reducing atmosphere. If there are oxygen vacancies in the material and either the Ti^{3+} or free electrons introduced by the vacancies contribute to electronic conductivity, a lower electronic conductivity should be observed in higher P_{O2} environment through the following reactions,

$$V_O^{\bullet\bullet} + \frac{1}{2}O_2 \rightarrow O_0 + 2\ h^{\bullet} \qquad (5.5)$$

$$h^{\bullet} + Ti^{III} \rightarrow\ Ti^{IV} \qquad (5.6)\ , \qquad or \quad h^{\bullet} + e^{'} \rightarrow nil \qquad (5.7)$$
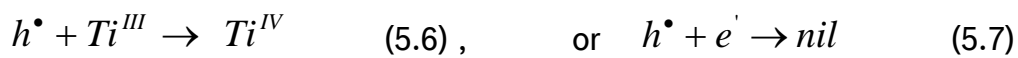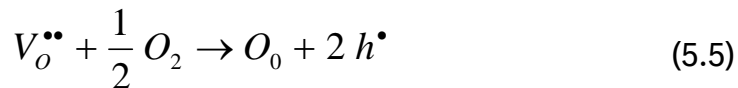
Electron holes which were created by filling oxygen vacancies would either react with Ti^{3+} ions to re-introduce Ti^{4+} ions or neutralize with free electrons. The Ti valence change or the neutralization reduces the number of electronic carriers, which leads to

the decrease in electronic conductivity. The conductivity in Ar atmosphere (~ 7.0 x 10^{-4} S/cm) was slightly higher than in air (~ 6.2 x 10^{-4} S/cm) in an aged spinel Li$_{4/3}$Ti$_{5/3}$O$_4$ pellet prepared in reducing atmosphere, suggesting that oxygen vacancies exist and either Ti^{3+} or electrons introduced by the vacancies contribute to the conductivity. If equation (5.2) describes the electronic conduction well, the change in electronic conductivity as a function of P$_{O2}$ can be calculated. Equation (5.2) then leads to

$$K = \left[V_O^{\bullet\bullet}\right]^{\frac{1}{2}} n \; P_{O2}{}^{\frac{1}{4}} \qquad (5.8)$$

where K is equilibrium constant and n is the density of charge carriers. The electroneutrality condition states,

$$n = 2\left[V_O^{\bullet\bullet}\right] \qquad (5.9)$$

By combining equation (5.8) and (5.9), the following equation is obtained:

$$n = \left(\sqrt{2}K\right)^{\frac{2}{3}} P_{O2}{}^{-\frac{1}{6}} \qquad (5.10)$$

By assuming an electronic conductivity, σ, is proportional to n, the relationship between σ and P$_{O2}$ is derived:

$$\sigma \propto P_{O2}{}^{-\frac{1}{6}} \qquad (5.11)$$

To check whether this relationship agrees with the experimental result, the slope of conductivity vs. P$_{O2}$ in a log scale was calculated. The calculated value was -0.008, which is significantly smaller than -1/6. This result may exclude the conduction mechanism by the free electrons suggested by equation (5.2). This result only from two measurement points, however, is not enough to conclude that the free electrons do not contribute to the conductivity. The smaller value can also be observed if the entire 1 mm thick sample was not in equilibrium with the measurement atmosphere.

The conduction of the samples processed in reducing atmosphere is thermally activated (Figure 4.9), which is typical for insulator or semiconductor materials. This thermally activated conduction suggests that the hopping conduction by the Ti^{3+} and Ti^{4+} ions or the band model with the free electrons in the extrinsic range may dominate the electronic conductivity.

With the hopping conduction model, mobility of electronic carrier is temperature dependent and carrier density is fixed at different temperatures. It can be understood in the case of spinel Li$_{4/3}$Ti$_{5/3}$O$_4$ processed in reducing atmosphere that the carrier

density, i.e. number of Ti^{3+}, decreases with time in air, leading to the degradation of electronic conductivity.

The band conduction in the extrinsic range could also support the result. In the extrinsic range, carrier concentration is temperature dependent and mobility is fixed at different temperatures. The carrier concentration (i.e. free electrons introduced by the oxygen vacancies) decreases with time in air, leading to the degradation of electronic conductivity. The extrinsic range is usually at much lower than room temperature in semiconductor so that the exhaustion range with the relatively flat electronic conductivity behavior against temperature can be utilized for electric application around room temperature. It would be, however, possible that spinel $Li_{4/3}Ti_{5/3}O_4$ processed in reducing atmosphere is in the extrinsic range even at room temperature if the gap between the oxygen vacancy state and the conduction band is relatively large. In fact, the experimental activation energy was ~ 0.2 eV, which is larger than the gap in typical semiconductors (e.g. 0,01 eV for P^{5+} on Si^{4+} site, [Mou03]).

The band conduction in the intrinsic range would not support the thermally activated result. If this was the case, the decrease in conductivity in air would have to be due to the decrease in electron mobility in the conduction band, which is unrealistic to occur.

To confirm if there are Ti^{3+} ions introduced by the oxygen vacancies in the material processed in reducing atmosphere, EPR (electron paramagnetic resonance) measurement were performed. Ti^{3+} ions can be detected by EPR measurements since Ti^{3+} ions have unpaired electron spins. EPR measurements proofed that there are Ti^{3+} ions in the spinel $Li_{4/3}Ti_{5/3}O_4$ samples processed in reducing atmosphere, although quantitative analysis was not performed.

Only with the results achieved in this study, the exact electronic conduction mechanism in spinel $Li_{4/3}Ti_{5/3}O_4$ processed in reducing atmosphere is still unclear. To determine if the conduction is dominated by Ti^{3+} ions or free electrons require further investigations. For example, conductivity measurements over a wider range of temperature may be useful; there would be a transition to an exhaustion range if the material follows the band conduction in the extrinsic range.

The Cu doped sample processed in reducing atmosphere resulted in higher electronic conductivity than the other samples (Figure 4.10). The low activation energy of Cu doped sample (Figure 4.11(a)) indicates that the conduction

mechanism may be different. The Cu ions may have been on the Li-sites and contributes to the increase in electronic conductivity as desired, but no clear signature of the Cu ions on the Li-sites was found in the (220) peak (Section 4.1.2). Moreover, in the Cu doped sample, elemental Cu was detected as a second phase by XRD measurement, and the amount of elemental Cu in the sample was estimated ~ 1 wt% by Rietvelt analysis for the sample with x = 0.03 for $Li_{4/3-x}Cu_xTi_{5/3}O_4$, whereas the total amount of Cu in this composition is 1.2 wt%; all Cu in the sample may exist as elemental Cu. This implies that the increase in electronic conductivity may not be due to the Cu ions on the Li-sites. Better quantitative structural analysis for the position and valence state of Cu is required to conclude the reason for the increase in electronic conductivity.

The Cu doped sample processed in air also increased the electronic conductivity. The value was measured by impedance spectroscopy, which may reflect Li-ion conductivity, but the activation energy measurement supports that the conductivity measured for the sample with x = 0.1 would be for electronic conductivity. Figure 5.2 and 5.3 show the conductivity as function of Cu dopant concentration and conductivity as a function of temperature for the Cu doped spinel $Li_{4/3}Ti_{5/3}O_4$ samples, respectively. The conductivity for the sample with x = 0.1 for $Li_{4/3-x}Cu_xTi_{5/3}O_4$ is higher than the sample with x = 0 or 0.03, and the activation energy for the sample with x = 0.1 (0.25 eV) is much different from the typical activation energies for Li-ion conductivity in the spinel $Li_{4/3}Ti_{5/3}O_4$ system (~ 0.5-0.6 eV as shown in Figure 4.14). Therefore, the conductivity for the sample with x = 0.1 can be considered as electronic conductivity.
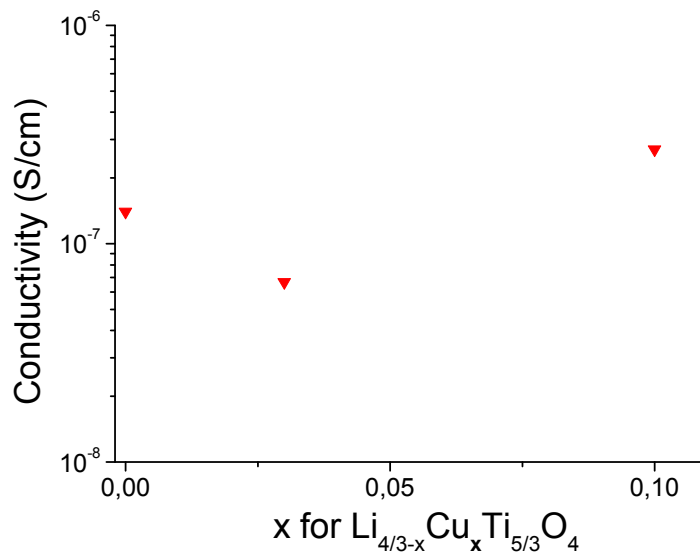
Figure 5.2. Electronic conductivity at room temperature as a function of Cu dopant concentration for Cu doped spinel $Li_{4/3}Ti_{5/3}O_4$ samples processed in air
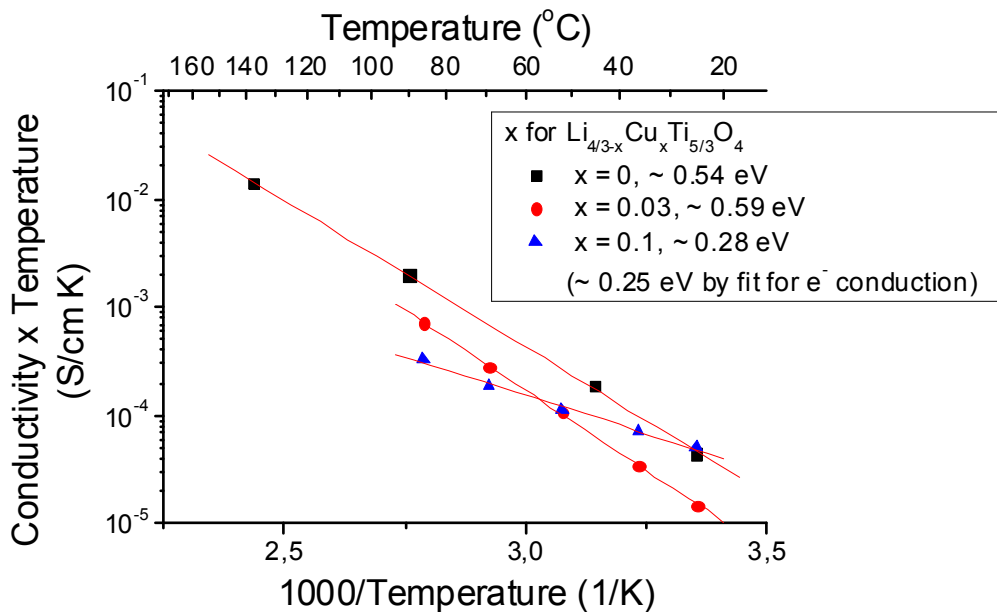
Figure 5.3. Conductivity multiplied by temperature as a function of temperature for Cu doped spinel $Li_{4/3}Ti_{5/3}O_4$ samples. The solid lines are fitted to an Arrhenius model.

For the Cu doped sample with x = 0.03, electronic conductivity could not be separated from Li-ion conductivity, probably since the Li-ion conductivity would be

still larger than the electronic conductivity or they are in the same range. The Cu doped samples processed in air did not show any elemental Cu as a second phase, so Cu incorporated into spinel Li$_{4/3}$Ti$_{5/3}$O$_4$ should contribute to the increase in electronic conductivity.

Electronic conductivity in the Mg doped samples processed in reducing atmosphere was investigated to confirm if there is a relationship between the Mg dopant concentration and the electronic conductivity. Assuming either of the following reactions,

$$(1-\frac{3}{4}x)Li_{4/3}Ti^{IV}_{5/3}O_4 + xMgO + \frac{5}{4}xTiO_2 \longrightarrow Li_{4/3-x}Mg_xTi^{IV}_{5/3-x}Ti^{III}_xO_4 + \frac{x}{4}O_2(g) \quad (5.12)$$

or,

$$(1-\frac{3}{4}x)Li_{4/3}Ti^{IV}_{5/3}O_4 + xMgO + \frac{5}{4}xTiO_2 \longrightarrow Li_{4/3-x}Mg_xTi^{IV}_{5/3}O_4 + x\ e^- + \frac{x}{4}O_2(g) \quad (5.13)$$
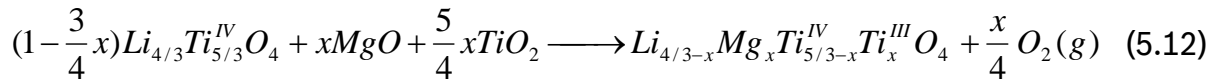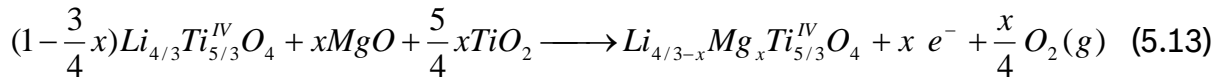
doping with Mg ions on Li sites in spinel Li$_{4/3}$Ti$_{5/3}$O$_4$ introduces either Ti^{3+} ions or extra free electrons in the structure. The amount of the Ti^{3+} ions or the free electrons should be proportional to the amount of Mg if either of the reactions above is correct. If the Ti^{3+} ions or the free electrons are responsible for the higher electronic conductivity, the correlation between the amount of Ti^{3+} ions or free electrons and electronic conductivity as a function of Mg concentration should be observed. However, the conductivity measurement did not show any clear trends with the dopant concentration (Figure 4.12). The stable activation energy (Figure 4.13) suggests that Mg doping would not affect the electronic conduction mechanism. Therefore the scatter in electronic conductivity as a function of the dopant concentration may be due to large error bars of the test. The measurement itself has relatively good precision (i.e. resolution of multimeter), but the sample preparation step can be problematic. One error source can be that samples are in air during sample preparation for a certain period of time, possibly up to total 1 hr. For example, contact with air cannot be avoided during pressing samples after calcination and transporting samples from an oven to a glove box, or vice versa. The duration in air was shown to be critical on electronic conductivity (Figure 4.8), but the duration cannot be controlled to be exactly same for all samples. Another error may arise from the difficulty to polish and electrode samples properly in a glove box. With these considerations, it may be concluded that there would be no clear change in electronic conductivity with increasing dopant concentration of Mg.

In the Mg doped spinel $Li_{4/3}Ti_{5/3}O_4$ samples processed in air, no Ti^{3+} ions were detected by EPR measurement and up to 5 wt% TiO_2 phase was observed as a second phase in the samples with high Mg doping concentrations (Figure 4.5). The anticipated but unproven solution with ionic compensated defects could be that Mg doping processed in air would be compensated not by Ti^{3+} ions as desired, but by titanium vacancies,

$$\left[V_{Ti}^{''''}\right] = 4\left[Mg_{Li}^{\bullet}\right] \tag{5.14}$$

through the following formula for the Mg doped sample with the nominal composition of $Li_{4/3-x}Mg_xTi_{5/3}O_4$,

$$\left((\frac{4}{3}-x)Li_{Li} + xMg_{Li}^{\bullet} + (\frac{5}{3}-\frac{x}{4})Ti_{Ti}^{IV} + \frac{x}{4}V_{Ti}^{''''} + 4O_O\right) + \frac{x}{4}TiO_2 \tag{5.15}$$

The excess Ti as a result of the Ti vacancies would react with oxygen to produce TiO_2, assuming that extra oxygen is always available in air. This reaction explains why Mg doping did not increase electronic conductivity as desired and why the TiO_2 phase was observed.

5.1.2.2 Li-ion conductivity

The Li-ion conductivity value of 10^{-7} S/cm and the activation energy of 0.51 eV for the undoped spinel $Li_{4/3}Ti_{5/3}O_4$ agree with literature data [Wol08][Hua04][Hay94], but they are much lower than the target value of 5 x 10^{-2} S/cm. The increase in lattice parameter with doping was observed as expected (Figure 4.7). The next assumption was that increasing lattice parameter would increase Li-ion conductivity, but it was not the case (Figure 4.15).

The conductivity even decreased with Mg and Cu doping, probably due to Mg/Cu on the tetrahedral site, which is a Li conduction path in the spinel $Li_{4/3}Ti_{5/3}O_4$. XRD results showed that some of Mg/Cu ions were on the tetrahedral site (Figure 4.6).

Another possibility which may improve Li-ion conductivity is to prepare materials with off-stoichiometric compositions. For example, Li vacancies in the structure may improve Li-ion conduction. As in the Li_2O-TiO_2 phase diagram (Figure 2.8), however, spinel $Li_{4/3}Ti_{5/3}O_4$ would not allow any off-stoichiometric compositions since spinel $Li_{4/3}Ti_{5/3}O_4$ has no or little solid solution range. In fact, a slight change in the amount of Li from the stoichiometry resulted in the appearance of TiO_2 or Li_2TiO_3 phase (Figure 4.2).

5.2 Ramsdellite $Li_2Ti_3O_7$ ceramics

5.2.1 Structural characterization

The phase distributions (Figure 4.17) for Ramsdellite $Li_{2+x}Ti_3O_{7+x/2}$ with $-0.1 < x < 0.1$ agree well with the phase diagram [Izq80]; with more Li, Li_2TiO_3 appeared as a second phase, and with more Ti, TiO_2 appeared as a second phase.

The solubilities of Nb and Zr into ramsdellite $Li_2Ti_3O_7$ was higher than that into spinel $Li_{4/3}Ti_{5/3}O_4$, suggesting that ramsdellite $Li_2Ti_3O_7$ can accommodate more change in the octahedra volume than spinel $Li_{4/3}Ti_{5/3}O_4$. The open space along the Li-ion channel around the octahedra framework in ramsdellite $Li_2Ti_3O_7$ may be contributing to the flexibility.

5.2.2 Electric conductivity

5.2.2.1 Electronic conductivity

The electronic conduction mechanism in ramsdellite $Li_2Ti_3O_7$ is not explained here, but the similar argument to the spinel $Li_{4/3}Ti_{5/3}O_4$ mentioned in section 5.1.2.1 would also be applicable for ramsdellite $Li_2Ti_3O_7$.

5.2.2.2 Li-ion conductivity

The pellet processed in air resulted in Li-ion conductivity $\sim 10^{-6}$ S/cm with the activation energy of 0.46 eV. The values agree with literatures [Boy79].

For ramsdellite $Li_2Ti_3O_7$, which possesses an anisotropic Li-ion conduction property, the increase in Li-ion conductivity is expected if the crystals are aligned along c-axis with the higher Li-ion conduction than the other axes. The increase, however, would be only one order of magnitude at the most [Boy79], so the alignment of the structure would not lead to the proposed target value of 5×10^{-2} S/cm.

Another possibility which may improve Li-ion conductivity is to prepare materials with off-stoichiometric compositions. As shown in Figure 2.8 and Figure 4.17, ramsdellite $Li_2Ti_3O_7$ has a narrow but finite solid solution range of $Li_{2+x}Ti_3O_{7+x/2}$. Creating Li vacancies or Li interstices in the structure may allow Li-ions to diffuse in the structure easier, which may increase Li-ion conductivity. As Figure 4.23 shows, however, both Li-ion conductivity and the activation energy did not change significantly with different x for $Li_{2+x}Ti_3O_{7+x/2}$. The result concludes that preparing off-

stoichiometry ramsdellite $Li_2Ti_3O_7$ compositions does not contribute to the increase in Li-ion conductivity.

The conductivity decreased with Mg and Cu doping (Figure 4.24), probably due to Mg/Cu in the Li channel along the c-axis, which is the Li conduction path in ramsdellite $Li_2Ti_3O_7$. The increase in the conductivity with Nb doping (Figure 4.24) could be associated with the increase in sample density with the dopant concentration of Nb. Figure 5.4 shows that the density of the samples increased as a function of Nb dopant concentration. Figure 5.5 shows the activation energy as a function of Nb concentration in comparison to Zr doped samples. The activation energy does not change significantly with the Nb dopant concentration, which confirms that the increase in conductivity would be due to the increase in sample density.
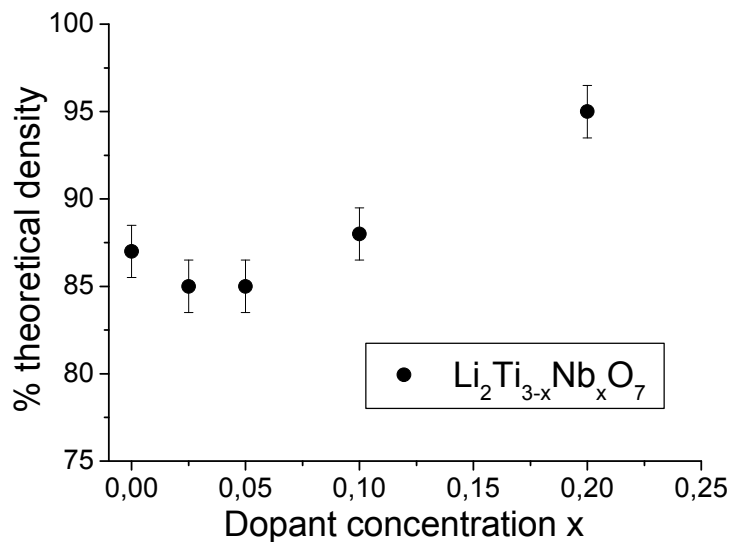
Figure 5.4. Relative density as a function of dopant concentration for Nb doped ramsdellite $Li_2Ti_3O_7$ samples processed in air. Theoretical densities were calculated with lattice parameters obtained from Rietvelt analysis on XRD data
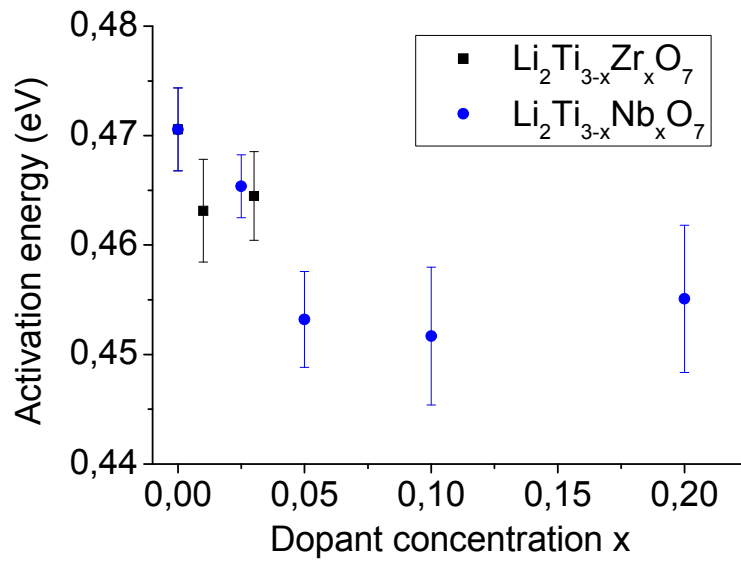
Figure 5.5. Activation energy as a function of dopant concentration for Nb and Zr doped ramsdellite Li$_2$Ti$_3$O$_7$ samples processed in air

The result indicates that unit cell volume increase does not lead to an increase in Li-ion conductivity in the ramsdellite Li$_2$Ti$_3$O$_7$ system.

5.3 Li insertion into spinel $Li_{4/3}Ti_{5/3}O_4$ ceramics

5.3.1 Electrochemical characterization

The flat voltage behavior in Figure 4.25(a) for the $Li_{4/3+x}Ti_{5/3}O_4$ agrees with literature [Sch99]. The test cells with the isostatically pressed pellets achieved almost 100% theoretical capacity, which suggests that 1 extra Li was inserted into spinel $Li_{4/3}Ti_{5/3}O_4$ to achieve the complete change into rock salt derived $Li_{7/3}Ti_{5/3}O_4$. The sintered pellets processed in air and reducing atmosphere achieved only about 0.3 % and 20 % theoretical capacity, respectively. This would be due to the fact that there are not many open pores available for the liquid electrolyte to go through the about 1 mm thick dense samples. Without the pores, electrons have to travel through the bulk ceramic from the current collector and Li-ions from the interface with the electrolyte to the other surface of the pellet. On the other hand, the pressed pellets have about 60 % theoretical density, which allows the electrolyte to travel through the pores toward the current collector of the cathode. Therefore, it would be easier for Li-ions and electrons to meet to incorporate into the $Li_{4/3+x}Ti_{5/3}O_4$.

The capacity during the 1st charge was much smaller than the capacity achieved during the 1st discharge cycle, as shown in Table 4.3. This implies that the Li extraction from the $Li_{4/3+x}Ti_{5/3}O_4$ phase with x > 0 is slower than the Li insertion into spinel $Li_{4/3}Ti_{5/3}O_4$. The slow Li extraction may be the sign that the Li-ion conduction in the $Li_{4/3+x}Ti_{5/3}O_4$ with x > 0 may be better than the spinel $Li_{4/3}Ti_{5/3}O_4$. The electronic conduction should not be the limiting factor for the slow Li extraction, since the capacity degradation was also observed for the samples processed in reducing atmosphere with the electronic conductivity of ~ 10^{-2} S/cm. Figure 5.6 shows schematics for Li insertion and extraction on a single $Li_{4/3+x}Ti_{5/3}O_4$ particle with the assumption that the white particle, spinel $Li_{4/3}Ti_{5/3}O_4$, is a bad Li-ion conductor and the blue particle, the $Li_{4/3+x}Ti_{5/3}O_4$, is a better Li-ion conductor. The worse capacity during the charge cycle can be explained well with this schematic. During the Li insertion, the blue phase grows from outside to inside, and during the Li extraction, the white phase grows from outside to inside. The white spinel $Li_{4/3}Ti_{5/3}O_4$ layer would block Li-ion conduction. The core-shell model is also suggested in the literature [Lu07].
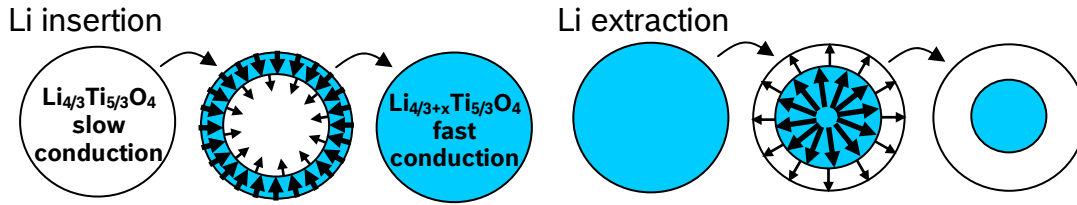
Figure 5.6. Schematics showing Li insertion and extraction on a single a single Li$_{4/3+x}$Ti$_{5/3}$O$_4$ particle

5.3.2 Electric characterization

Electronic conductivity increased with both electrochemical and chemical Li insertion into spinel Li$_{4/3}$Ti$_{5/3}$O$_4$. (Figure 4.28 for electrochemical and Figure 4.33 for chemical insertion). This result implies that only Ti^{3+} ions or free electrons without formation of oxygen vacancies can increase electronic conductivity, since no oxygen vacancies are created during the Li insertion as expressed in the following equations;

$$x\,Li^+ + x\,e^- + Li_{4/3}Ti_{5/3}^{+IV}O_4 \longrightarrow Li_{4/3+x}Ti_{5/3-x}^{+IV}Ti_x^{+III}O_4 \qquad (5.16)$$

$$x\,Li^+ + x\,e^- + Li_{4/3}Ti_{5/3}^{+IV}O_4 \longrightarrow Li_{4/3+x}Ti_{5/3}^{+IV}O_4 + x\,e^- \qquad (5.17)$$
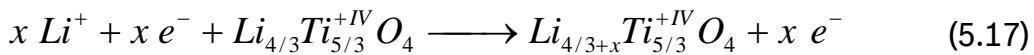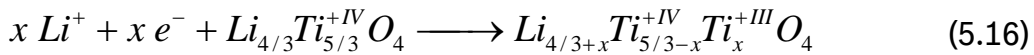
Each extra Li incorporated into the spinel Li$_{4/3}$Ti$_{5/3}$O$_4$ is compensated either by Ti^{3+} or a free electron. The thermally activated conduction (Figure 4.31) suggests that equation 5.16 would likely to be the case. If equation 5.17 was correct, the free electrons would be in the conduction band and the metallic conduction behavior should be observed; there are no oxygen vacancies unlike the samples processed in reducing atmosphere, and there would be no energy levels available between valence and conduction bands, which should result in the free electrons in equation 5.17 in the conduction band.

The electronic conductivity of the Li-inserted sample decreased with time in air (Figure 4.34). Reaction of the Li$_{4/3+x}$Ti$_{5/3}$O$_4$ with oxygen (or carbon dioxide) in air may be preferred due to the electronically unstable Ti^{3+} or the free electrons;

$$Li_{4/3+x}Ti_{5/3-x}^{+IV}Ti_x^{+III}O_4 + \frac{1}{4}x\,O_2(or\,CO_2) \longrightarrow Li_{4/3}Ti_{5/3}^{+IV}O_4 + \frac{1}{2}x\,Li_2O(or\,Li_2CO_3)$$

$$(5.18)$$

$$Li_{4/3+x}Ti_{5/3}^{+IV}O_4 + x\,e^- + \frac{1}{4}x\,O_2(or\,CO_2) \longrightarrow Li_{4/3}Ti_{5/3}^{+IV}O_4 + \frac{1}{2}x\,Li_2O(or\,Li_2CO_3)$$

$$(5.19)$$
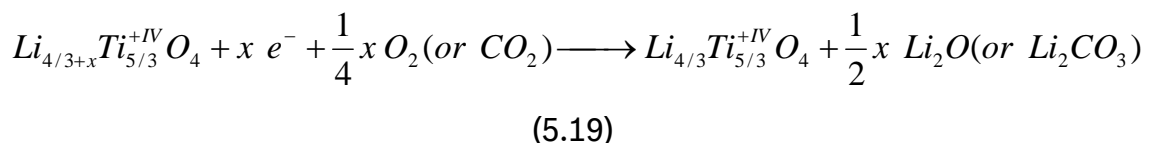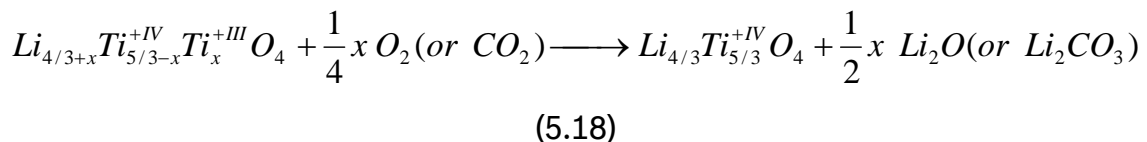
The equations would explain the decrease, but this solution has not been proven.

XRD analysis was performed on the Li-inserted sample which was in air for 2 weeks, but neither Li_2O nor Li_2CO_3 was confirmed to exist in the sample. The compounds formed by the excess inserted Li may be in amorphous phases.
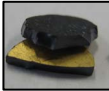
The measurement with the LiPON layers confirms that the Li insertion into spinel $Li_{4/3}Ti_{5/3}O_4$ increases Li-ion conductivity, but only qualitative analysis is possible with the current measurement set-up. As explained in Chapter 4.3.4, the separation of the contribution of the $Li_{4/3+x}Ti_{5/3}O_4$ to the Li-ion conductivity from that of the LiPON was difficult. The wide range of conductivity values ($10^{-5} - 10^{-3}$ S/cm) was also observed at different applied currents (Figure 4.38). The reason for the wide range of conductivity values at different currents may be due to the mechanical strength of LiPON layers. The LiPON layers may be damaged at higher current. The damaged LiPON part may lead to a local shortcut of the cell, which results in a lower resistance of the cell. For quantitative measurement, the LiPON layers need to be more uniformly sputtered on the $Li_{4/3+x}Ti_{5/3}O_4$ samples and the Li-ion conductivity of the LiPON layers needs to be known accurately. Moreover, the contact of the samples with air could not be completely avoided during sample transportation for the LiPON sputtering preparation, which may degrade the conduction property as well. Once the quantitative Li-ion conductivity measurement becomes available, it would be interesting to see the conductivity change as a function of x for $Li_{4/3+x}Ti_{5/3}O_4$.

The mechanism for the good Li-ion conduction in the $Li_{4/3+x}Ti_{5/3}O_4$ samples is not understood well. If the Li insertion undergoes the two phase reaction, there may be good conductions along the phase boundary between the spinel $Li_{4/3}Ti_{5/3}O_4$ and the rock salt derived $Li_{7/3}Ti_{5/3}O_4$. If the Li insertion occurs through the single solid solution phase, $Li_{4/3+x}Ti_{5/3}O_4$, the random distribution of Li ions in the tetrahedral sites and the Li ions in the octahedral sites which are introduced by the Li insertion may enhance the Li-ion conduction in the material.

5.4 Relationship between spinel, ramsdellite, and rock salt derived lithium titanates

Table 5.1 summarizes the electronic and Li-ion conductivity of the undoped spinel $Li_{4/3}Ti_{5/3}O_4$ in terms of processing atmospheres and Li-insertion towards rock salt derived $Li_{7/3}Ti_{5/3}O_4$.

Table 5.1. Summary for the electronic and Li-ion conductivity of the undoped spinel $Li_{4/3}Ti_{5/3}O_4$ and the $Li_{4/3+x}Ti_{5/3}O_4$ at room temperature

Synthesis (processing atmosphere)	Li insertion towards rock salt derived $Li_{7/3}Ti_{5/3}O_4$
In air $\sigma_{el} < 10^{-9}$ S/cm $\sigma_{ion} \sim 10^{-7}$ S/cm	$\sigma_{el} \sim 10^{-3\sim4}$ S/cm σ_{ion} increased (measured qualitatively)
In reducing atmosphere $\sigma_{el} \sim 10^{-2}$ S/cm σ_{ion} not measured	$\sigma_{el} > 10^{-2}$ S/cm σ_{ion} not measured

For higher electronic conductivities, the introduction of Ti^{3+} or/and free electrons in the lithium titanates is essential. The Ti^{3+} or/and free electrons were introduced by the oxygen vacancies created through the process in reducing atmosphere or by the Li insertion. The best conductivity without doping was achieved for the sample processed in reducing atmosphere, followed by the Li insertion. This result suggests that both the process in reducing atmosphere and the Li insertion contribute to electronic conductivity. However, the oxygen vacancies created by the process in reducing atmosphere were proven to be essential for the high electronic conduction; the Li insertion into the spinel $Li_{4/3}Ti_{5/3}O_4$ samples processed in air never achieved the electronic conductivity higher than that of the samples processed in reducing atmosphere.

The distinct difference in electronic conductivity between the samples prepared in reducing atmosphere and the samples in which Li was inserted is the degradation in air. Figure 5.7 compares the degradation of electronic conductivity with time in air. The electronic conductivity in both samples decreased with time in air, but the decrease was much faster in the Li inserted samples than in the samples processed in reducing atmosphere. This was also clear from the change in color of the samples. Figure 5.8 shows the color change with time in air for the samples processed in reducing atmosphere and the Li inserted samples. The powder

calcined in reducing atmosphere became grayish after 1 year in air, but the color change in the pellet sintered in reducing atmosphere was not noticeable with human eyes. The color of the Li inserted sample completely changed to white within 18 days. The decrease in electronic conductivity in air was assumed to be due to the oxygen diffusion for the samples processed in reducing atmosphere (equations 5.3 and 5.4) and the lithium diffusion for the Li inserted samples (equations 5.14 and 5.15). The faster decrease in electronic conductivity in the Li inserted sample suggests that the Li diffusion in the $Li_{4/3+x}Ti_{5/3}O_4$ would be much faster than the O diffusion in the spinel $Li_{4/3}Ti_{5/3}O_4$ sample processed in reducing atmosphere.
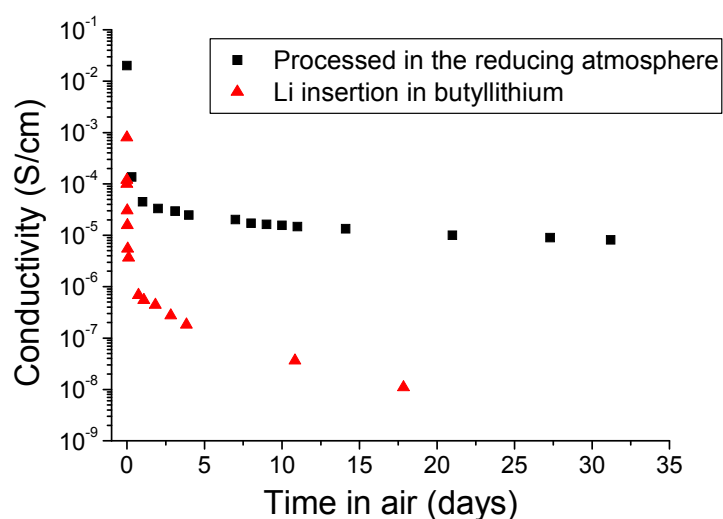
Figure 5.7. Electronic conductivity at room temperature as a function of time in air for the spinel $Li_{4/3}Ti_{5/3}O_4$ pellet processed in reducing atmosphere and the spinel spinel $Li_{4/3}Ti_{5/3}O_4$ pellet processed in air which was in butyllihium for 7 days targeted for x = 0.5 for $Li_{4/3+x}Ti_{5/3}O_4$

| (a) | (b) | (c) | (d) | (e) |
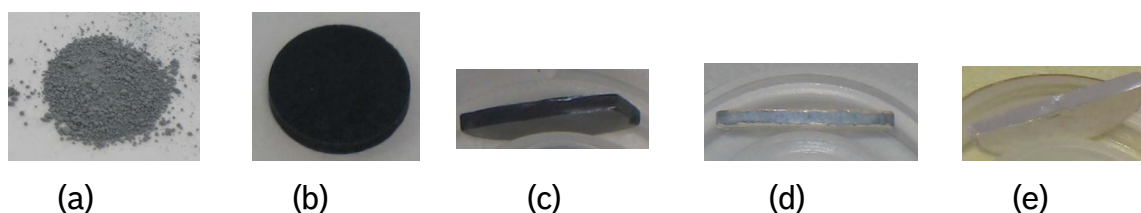
Figure 5.8. Pictures of pellets showing the color change over time in air. After 1 year in air for (a) the spinel $Li_{4/3}Ti_{5/3}O_4$ powder calcined in reducing atmosphere and (b) the spinel $Li_{4/3}Ti_{5/3}O_4$ pellet sintered in reducing atmosphere in air. After (c) 0 day (d) 3 days (e) 18days for the spinel spinel $Li_{4/3}Ti_{5/3}O_4$ pellet processed in air which was in butyllihium for 7 days targeted for x = 0.5 for $Li_{4/3+x}Ti_{5/3}O_4$

Doping of aliovalent ions was performed to possibly introduce Ti^{3+} in the spinel $Li_{4/3}Ti_{5/3}O_4$ and the ramsdellite $Li_2Ti_3O_7$ structure, but the conductivity did not change with the dopants, Mg, Nb, and Ta. This is contrary to the literature, which showed the increase in electronic conductivity with the dopants [Che03][Yi10]. This result again proves that the oxygen vacancies are essential for the high electronic conduction. Both in the spinel $Li_{4/3}Ti_{5/3}O_4$ and the ramsdellite $Li_2Ti_3O_7$, only Cu doping increased electronic conductivity further for samples processed in reducing atmosphere. The Cu ions may have been on the Li-sites and contributes to the increase in electronic conductivity as desired, but the existence of elemental Cu as a 2nd phase makes it difficult to conclude the reason for the increase in electronic conductivity (Section 5.1.2.1).

In order to possibly increase Li-ion conductivity in the spinel $Li_{4/3}Ti_{5/3}O_4$ and the ramsdellite $Li_2Ti_3O_7$, the lattice size was expanded by doping. The expansion of the lattice size, however, did not help to increase Li-ion conductivity both in the spinel $Li_{4/3}Ti_{5/3}O_4$ and the ramsdellite $Li_2Ti_3O_7$. This may be due to the fact that larger lattice parameters do not necessarily lead to expand the spaces for the Li-ion conduction in the structures.

The Li insertion into spinel $Li_{4/3}Ti_{5/3}O_4$ increased Li-ion conductivity. Only the qualitative measurement was conducted in this study, so it would be interesting to measure Li-ion conductivity quantitatively and understand the structure as a function of x for $Li_{4/3+x}Ti_{5/3}O_4$ for further study. The Li insertion also increased electronic conductivity, which makes the $Li_{4/3+x}Ti_{5/3}O_4$ attractive for the cathode purpose in Li-S battery. As explained in section 2.5, however, the $Li_{4/3+x}Ti_{5/3}O_4$ reacts with S within the cathode during open circuit until the poor conducting spinel $Li_{4/3}Ti_{5/3}O_4$ is obtained. In order to maintain the good conducting phase during Li-S battery operations, Fe doping was performed (section 4.4 and 5.5)

The Li insertion into ramsdellite $Li_2Ti_3O_7$ was not performed in this study. A deeper study on Li insertion into ramsdellite $Li_2Ti_3O_7$ may be interesting to see how the Li insertion changes the structure and the conduction property, although the Li insertion into ramsdellite $Li_2Ti_3O_7$ does not seem to increase Li-ion conductivity in literature [Gar96].

5.5 Fe doped spinel $Li_{4/3}Ti_{5/3}O_4$ ceramics

5.5.1 Structural Characterization

The samples with y = 0.115 and 0.25 for $Li_{4/3-y/3}Fe_yTi_{5/3-2y/3}O_4$ resulted in Fd-3m structure and $P4_332$ structure, respectively, when they were processed in air. The 2 different phases for the 2 different compositions are as expected [Sch97/2]. When the samples were processed in reducing atmosphere, both samples with y = 0.115 and 0.25 resulted in the spinel (i.e. Fd-3m) structure. The sampled processed in reducing atmosphere contained elemental Fe as a 2nd phase, which will reduce the amount of Fe in the lithium titanate. The less amount of Fe in the sample with y = 0.25 may have brought the sample to the region of the Fd-3m structure in the phase diagram (Figure 2.13)

5.5.2 Electrical characterization

The Fe doped sample processed in air increased the electronic conductivity, similar to the Cu doped sample. The value was measured by impedance spectroscopy, which may reflect Li-ion conductivity, but the activation energy measurement supports that the conductivity measured for the sample with y = 0.25 would be for electronic conductivity. Figure 5.9 and 5.10 show the conductivity as function of Fe dopant concentration and conductivity as a function of temperature for the Fe doped spinel $Li_{4/3-y/3}Fe_yTi_{5/3-2y/3}O_4$ samples, respectively. The conductivity for the sample with y = 0.25 for $Li_{4/3-y/3}Fe_yTi_{5/3-2y/3}O_4$ is higher than the sample with y = 0 or 0.115, and the activation energy for the sample with y = 0.25 (0.24 eV) is significantly different from the typical activation energies for Li-ion conductivity in the spinel $Li_{4/3}Ti_{5/3}O_4$ system (~ 0.5-0.6 eV). Therefore, the conductivity for the sample with y = 0.25, which increases with increasing temperature with the activation energy of 0.24 eV, can be considered as electronic conductivity.
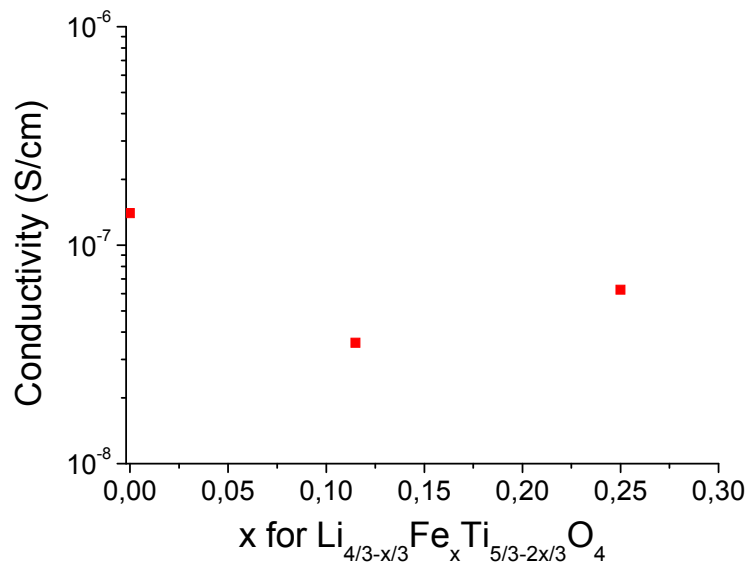
Figure 5.9. Electric conductivity at room temperature as a function of Fe dopant concentration for Fe doped spinel $Li_{4/3-y/3}Fe_yTi_{5/3-2y/3}O_4$ samples processed in air
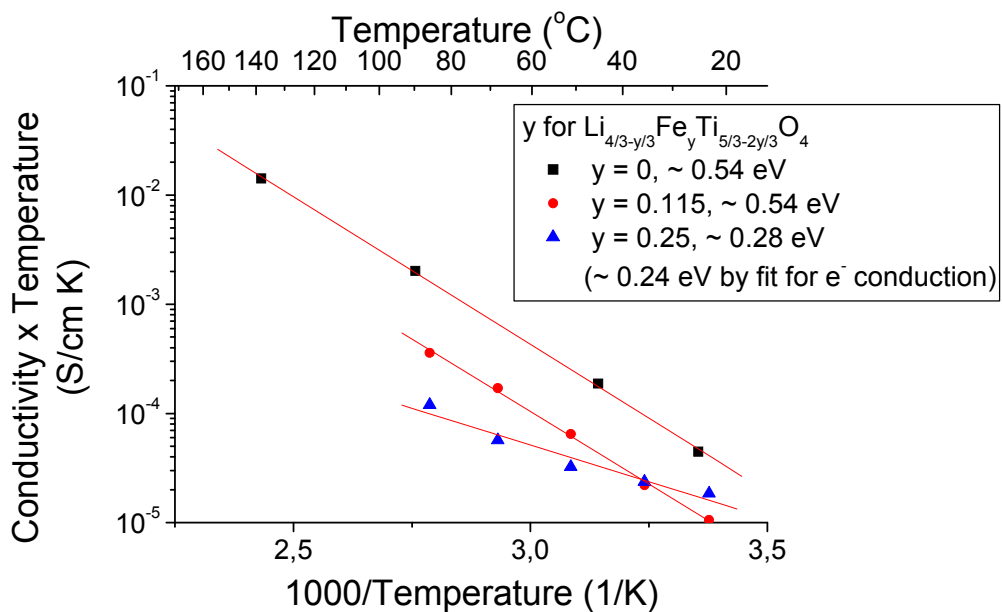
Figure 5.10. Conductivity multiplied by temperature as a function of temperature for Fe doped spinel $Li_{4/3-y/3}Fe_yTi_{5/3-2y/3}O_4$ samples. The solid lines are fitted to an Arrhenius model

For the Fe doped sample with y = 0.115, electronic conductivity could not be separated from Li-ion conductivity, probably since the Li-ion conductivity would be still bigger than the electronic conductivity or they are in the same range. The Fe doped samples processed in air did not show any elemental Fe as a second phase,

so Fe incorporated into spinel $Li_{4/3}Ti_{5/3}O_4$ should contribute to the increase in electronic conductivity.

The electronic conductivity did not increase with the Fe doping when the samples were processed in reducing atmosphere. This is different from the Cu doped samples processed in reducing atmosphere, which showed an increase in electronic conductivity. Elemental Fe was found in the samples, but elemental Fe seems not to contribute to increase electronic conductivity.

5.5.3 Electrochemical and chemical Li insertion

During electrochemical Li insertion, the Fe doped samples processed in air were not in equilibrium even after pauses for 71 hr (Figure 4.43 (a)). This would be the main cause for the difference between the voltage profiles of this study (Figure 4.44(a)) and of Scharner (Figure 2.14) [Sch97/1]; the voltages of the Fe doped samples were higher than the undoped sample, but the clear 2 step voltage behavior observed by Scharner was not observed. The long relaxation time would be due to the low conductivities observed with Li insertion into the Fe doped samples (Figure 4.46). Scharner had the similar test set-up configuration, but the samples were completely dipped in an electrolyte [Sch97/1], which may have led to the faster relaxation. Thinner samples would also help to shorten the relaxation time.

The samples processed in reducing atmosphere show a different electrochemical behavior from samples processed in air (Figure 4.43(b)). The electrochemical behavior looks similar to the behavior observed by Scharner (Figure 2.14) for the Fe doped sample, but Figure 4.43 (b) showed the 2 step voltage behavior even for the sample without Fe doping. The 2 step voltage behavior for the undoped sample processed in reducing atmosphere is different from the ~ 1.5 V flat voltage behavior observed for the sample processed in air in this study (Figure 4.25 (a)) and also in literature [Sch99]. There were no obvious differences between the Fe doped samples and the undoped sample processed in reducing atmosphere, suggesting that Fe^{3+} would have been reduced to Fe^{2+} or elemental Fe during the process in reducing atmosphere and that there would be no Fe^{3+} available to be reduced during the discharge process. This implies that the small shoulders observed at 1.6-2.2 V are not due to the Fe doping. All the samples processed in reducing atmosphere contained up to 7 wt% Li_2TiO_3. Li_2TiO_3 is known to have electrochemical activity at

1.7-1.8 V [Mor08], so the small shoulders at 1.6-2.2V may be due to the undesired Li$_2$TiO$_3$ phase.

The change in conductivity with the Li insertion into the Fe doped samples was monitored by the direct contact of Li-metal on the sintered pellets. The change in conductivity was different for the undoped and the Fe doped samples processed in air. Figure 5.11 compares the conductivity change for the undoped and the Fe doped samples. The slow increase in the Fe doped sample agrees with the slower color change of the Fe doped samples compared to the undoped sample (Figure 4.29 for the undoped sample and 4.45 for the Fe doped sample). The inconsistency for the lengths of lower voltage plateaus may be due to the difference in contact between Li metal and the pellets and thicknesses of the samples, which were not exactly identical among the samples. The slow increase in electronic conductivity from 10^{-8} S/cm to 10^{-7} ~ 10^{-6} S/cm observed for the chemical Li insertion in the Fe doped samples may correspond to the high voltage (~ 2.3 V) range associated with the change from Fe^{3+} to Fe^{2+} observed for the electrochemical Li insertion [Sch97/1]. The rapid increase in electronic conductivity after 750-1500 hr for the chemical Li insertion may correspond to the shift to the 1.5 V range for the electrochemical Li insertion (Figure 2.14). If this assignment is correct, the introduction of Fe^{2+} into the Fe doped spinel Li$_{4/3-y/3}$Fe$_y$Ti$_{5/3-2y/3}$O$_4$ by Li insertion does not contribute to increase electrical conductivity as much as the undoped spinel Li$_{4/3}$Ti$_{5/3}$O$_4$ with the introduction of Ti^{3+}. The slower species (i.e. either electronic or Li-ion conduction) limits the increase in the measured conductivity in this test set-up, implying that the introduction of Fe^{2+} does not help to increase electronic or/and Li-ion conductivity as much as the introduction of Ti^{3+}. The total conductivity values in the Fe doped samples after the rapid increases at 750 − 1500 hr are higher than the undoped sample, which makes the Fe doped samples with the Li insertion promising for the application in Li-S battery. To separate the electronic and ionic contributions to the conductivity, the measurement with the LiPON layer can be performed for example, but such measurements were not performed in this study.
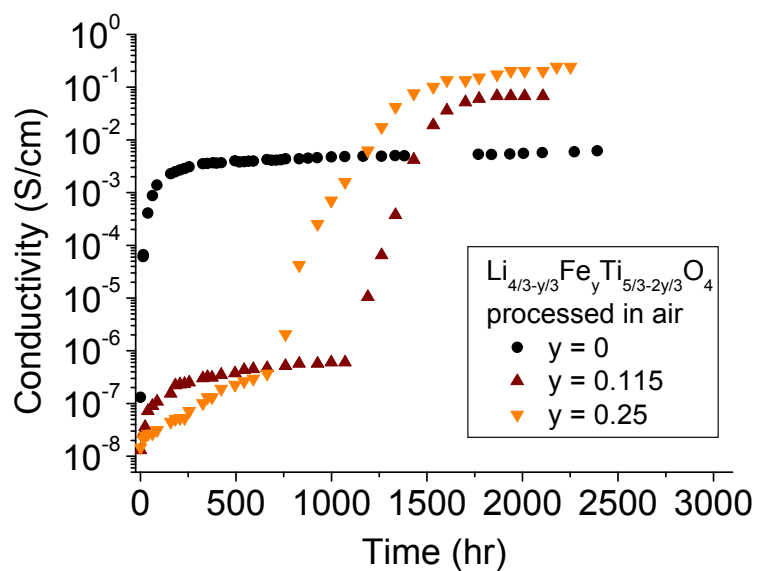
Figure 5.11. Electrical conductivity change in time by the contact with Li-metal for the undoped and Fe doped samples, $Li_{4/3-y/3}Fe_yTi_{5/3-2y/3}O_4$

Chapter 6: Summary

A mixed (i.e. Li-ion and electron) conducting ceramic material was investigated to replace the use of C in the cathode part of Li-S battery, in order to improve the structural stability during battery cycling. The mixed conductor is required to possess the following properties to achieve the desired battery performance.

1. High electronic conductivity (Target conductivity at room temperature ~ 5 x 10^{-2} S/cm)

2. High Li-ion conductivity (Target conductivity at room temperature ~ 5 x 10^{-2} S/cm)

3. Good structural stability during operation of battery

4. Smaller electrochemical potential vs. Li/Li$^+$ than that of sulfur (~2.1 V)

To develop the mixed conductor satisfying the 4 requirements, lithium titanate ceramic system was investigated. Materials in the lithium titanate system are attractive for the cathode structure purpose for the following reasons;

- Wide variety of phases in the system to be investigated

- High cycle stability of Li-ion batteries with lithium titanate materials as anode

- Electrochemical potential vs. Li/Li$^+$ at about 1.5V for some phases

With the high structural stability and electrochemical properties of the phases in the lithium titanate system, the focus of the study was narrowed down to investigate and develop phases with high Li-ion and electronic conductivities in the lithium titanate system to achieve the target values of 5 x 10^{-2} S/cm. Spinel $Li_{4/3}Ti_{5/3}O_4$, ramsdellite $Li_2Ti_3O_7$, and spinel - rock salt derived $Li_{4/3+x}Ti_{5/3}O_4$ were investigated. Improvement of Li-ion and electronic conductivities was attempted through controlling processing atmosphere, doping of aliovalent ions on either Li or Ti site, and Li insertion into spinel $Li_{4/3}Ti_{5/3}O_4$.

In both spinel $Li_{4/3}Ti_{5/3}O_4$ and ramsdellite $Li_2Ti_3O_7$, processing in controlled reducing atmosphere increased electronic conductivity up to about the target value and Cu doping improved the conductivity further. Li insertion into spinel $Li_{4/3}Ti_{5/3}O_4$ also resulted in an increase in electronic conductivity. The conduction mechanism responsible for the improved electronic conductivity was analyzed through electric characterization. The dominant effect on the increase would come from Ti^{3+} or/and free electrons introduced by oxygen vacancies through the process in reducing atmosphere. The thermally activated conduction supports the contribution of the Ti^{3+} to the conductivity through electron hopping mechanism or the contribution of the free electrons through the band conduction mechanism in the extrinsic range for the

sample processed in reducing atmosphere. The thermally activated conduction was also observed for the Li-inserted sample, suggesting that the Ti^{3+} introduced by the inserted Li contributes to the increase in electronic conductivity.

In terms of Li-ion conductivity, doping spinel $Li_{4/3}Ti_{5/3}O_4$ and ramsdellite $Li_2Ti_3O_7$ was attempted to increase lattice size with the assumption that larger spaces in the structure make Li-ion movement easier, which would result in an increase in Li-ion conductivity. However, Li-ion conductivity did not increase with doping, even though the lattice size increased with the doping as desired.

Li insertion into spinel $Li_{4/3}Ti_{5/3}O_4$, i.e. $Li_{4/3+x}Ti_{5/3}O_4$, was studied to investigate if the Li insertion contributes to increase Li-ion conductivity. The Li insertion was confirmed to increase Li-ion conductivity qualitatively by the measurement with the LiPON layers as electronically blocking electrodes. Further study on the quantitative measurement of Li-ion conductivity as a function of x for $Li_{4/3+x}Ti_{5/3}O_4$ would be of interest.

The $Li_{4/3+x}Ti_{5/3}O_4$ ceramic may possess the desired electronic and Li-ion conductivities. There is, however, a potential problem during open circuit with the $Li_{4/3+x}Ti_{5/3}O_4$ ceramic in the cathode matrix in Li-S battery: The cathode of S with the Li inserted spinel $Li_{4/3}Ti_{5/3}O_4$ would suffer from self discharge, since electrochemical potential vs. Li/Li^+ of sulfur is higher than that of the $Li_{4/3+x}Ti_{5/3}O_4$. The self discharge leads to a loss of capacity and inferior battery performance due to the spinel $Li_{4/3}Ti_{5/3}O_4$ phase with inferior Li-ion and electronic conductivities. Fe doping could be a solution to overcome the problem; the 2 step voltage behavior, ~2.3V and ~1.5V, during Li insertion into the Fe doped spinel $Li_{4/3-y/3}Fe_yTi_{5/3-2y/3}O_4$ may stabilize the phase with good Li-ion and electronic conductivities. The Li insertion into the Fe doped samples, y = 0.115 and 0.25 for $Li_{4/3-y/3}Fe_yTi_{5/3-2y/3}O_4$ by the contact with Li-metal showed that the total conductivity increased with time. The separation of the conductivity into electronic and Li-ion contributions and optimization of x and y values for $Li_{4/3-y/3+x}Fe_yTi_{5/3-2y/3}O_4$ would lead to realize the desired ceramic material with sufficient electronic and Li-ion conductivities for the cathode purpose in Li-S battery.

References

[Adl74]   Adler, D. "Electrical Transport: General Concepts," in *Electrical Conductivity in Ceramics and Glass, Part A*, N. M. Tallan, Ed., (Marcel Dekker, Inc. New York, 1974).

[Akr04]   Akridge, J.R., Y. V. Mikhaylik, and N. White, "Li/S fundamental chemistry and application to high-performance rechargeable batteries," Solid State Ionics **175** 243-245 (2004).

[Arm08]   Armand, M. and J. Tarascon, "Building Better Batteries," Nature **451** 652-657 (2008).

[Arr97]   Arroyo y de Dompablo, M. E., E. Moran, A. Varez, and F. Garcia-Alvarado, "Electrochemical Lithium Intercalation in $Li_2Ti_3O_7$-Ramsdellite Structure," Materials Research Bulletin **32** [8] 993-1001 (1997).

[Arr00]   Arroyo y de Dompablo, M. E., A. Varez, and F. Garcia-Alvarado, "Structural Study of Electrochemically Obtained $Li_{2+x}Ti_3O_7$," Journal of Solid State Chemistry **153** 132-139 (2000).

[Boy79]   Boyce, J. B. and J. C. Mikkelsen Jr., "Anisotropic Conductivity in a Channel-Structured Superionic Conductor: $Li_2Ti_3O_7$," Solid State Communications **31** 741-745 (1979).

[Che01]   Chen, C.H., J. T. Vaughey, A. N. Jansen, D. W. Dees, A. J. Kahaian, T. Goacher, and M. M. Thackeray, "Studies of Mg-substituted $Li_{4-x}Mg_xTi_5O_{12}$ Spinel Electrodes ($0 \le x \le 1$) for Lithium Batteries," Journal of the Electrochemical Society **148** [1] A102-A104 (2001).

[Che03/1]   Cheon, S, K. Ko, J. Cho, S. Kim, E. Chin, and H. Kim, "Rechargeable Lithium Sulfur Battery. I. Structural Change of Sulfur Cathode during Discharge and Charge," Journal of the Electrochemical Society **150** 796-799 (2003).

References

[Che03/2] Cheon, S, K. Ko, J. Cho, S. Kim, E. Chin, and H. Kim, "Rechargeable Lithium Sulfur Battery. II. Rate Capability and Cycle Characteristics," Journal of the Electrochemical Society **150** 800-805 (2003).

[Cul01] Cullity, B. D. and S. R. Stock, *Elements of X-Ray Diffraction* (Prentice-Hall, New Jersey, 2001).

[Dis95] Dissanayake, M. A. K. L., R. P. Gunawardane, H. H. Sumathipala, and A. R. West, "New Solid Electrolytes and Mixed Conductors: $Li_{3+x}Cr_{1-x}M_xO_4$: M = Ge, Ti," Solid State Ionics **76** 215-220 (1995).

[Eis09] Eisele, U., M. Königsmann, G. Deromelaere, B. Schumann, and R. Aumayer, "Lithium-Sulfur Cell and Method for Manufacturing", Patent DE102009055223.

[Eis10] Eisele, U. and L. Schwegler, "Lithiumzelle mit verbesserter Kathodenstruktur und Herstellungsverfahren hierfür", Patent DE102010001632.

[Gar96] Garnier, S., C. Bohnke, O. Bohnke, and J. L. Fourquet, "Electrochemical Intercalation of Lithium into the Ramsdellite-Type Structure of $Li_2Ti_3O_7$," Solid State Ionics **83** 323 - 332 (1996).

[Goo07] Goodenough, J. B., H.D. Abruna, and M.V. Buchanan, *Basic Research Needs for Electrical Energy Storage* (Office of Basic Energy Sciences, U.S. Department of Energy, Washington D.C., 2007).

[Goo11] Goodenough, J. B. and Y. Kim, "Challenges for Rechargeable Batteries," Journal of Power Sources **196** 6688-6694 (2011).

[Gov98] Gover, R. K. B. and J. T. S. Irvine, "A New Solid Solution Series Linking $LiTi_2O_4$ and $Li_2Ti_3O_7$ Ramsdellites: A Combined X-Ray and Neutron Study," Journal of Solid State Chemistry **141** 365-372 (1998).

104

[Gov99]   Gover, R. K. B., J. R. Tolchard, H. Tukamoto, T. Murai, and J. T. S. Irvine, "Investigation of Ramsdellite Titanates as Possible New Negative Electrode Materials for Li Batteries," Journal of the Electrochemical Society **146** [12] 4348-4353 (1999).

[Ham06]   Hamon, Y., A. Douard, F. Sabary, C. Marcel, P. Vinatier, B. Pecquenard, and A. Levasseur, "Influence of sputtering conditions on ionic conductivity of LiPON thin films," Solid State Ionics **177** [3-4] 257-261 (2006).

[Hay94]   Hayashi, S. and H. Hatano, "Ionic Conduction of $Li_2Ti_3O_7$ and $Li_4Ti_5O_{12}$," Journal of the Ceramic Society of Japan **102** 379-383 (1994).

[Hua04]   Huang, S., Z. Wen, X. Zhu, and Z. Gu, "Preparation and Electrochemical Performance of Ag Doped $Li_4Ti_5O_{12}$," Electrochemistry Communications **6** 1093-1097 (2004).

[Hug02]   Huggins, R. A., "Simple Method to Determine Electronic and Ionic Components of the Conductivity in Mixed Conductors: A Review," Ionics **8** 300-313 (2002).

[FIZ11]   FIZ Karlsruhe GmbH, *Inorganic Crystal Structure Database, FindIt version 1.7.2* (2011).

[Izq80]   Izquierdo, G. and A. R. West, "Phase Equilibria in the System Li_2O-TiO_2," Materials Research Bulletin **15** 1655-1660 (1980).

[Joh76]   Johnston, D.C., "Superconducting and Normal State Properties of $Li_{1+x}Ti_{2-x}O_4$ Spinel Compounds. I. Preparation, Crystallography, Superconducting Properties, Electrical Resistivity, Dielectric Behavior, and Magnetic Susceptibility," Journal of Low Temperature Physics **25** [1/2] 145-175 (1976).

[Kin76]   Kingery, W. D., H. K. Bowen, and D. R. Uhlmann, *Introduction to Ceramics* (John Wiley & Sons, New York, 1976).

References

[Kit05]   Kittel, C., *Introduction to Solid State Physics* (John Wiley & Sons, New York, 2005).

[Köh09]   Private communication with Dr. Thomas Köhler, CR/ARA2, Robert Bosch GmbH (2009).

[Kos08]   Kosugi, S., H. Inagaki, and N. Takami, "Newly Developed SCiB$_{TM}$ High-Safety Rechargeable Battery," Toshiba review **63** [2] 54-57 (http://www.scib.jp/index.htm) (2008).

[Krö56]   Kröger, F. A. and V. J. Vink, "Relations between the Concetrations of Imperfections in Crystalline Solids," *Solid State Physics*, Vol. 3, 307-435 F. Seizt and D. Turnbull, Eds. (Academic Press, Inc., New York, 1956).

[Krö64]   Kröger, F. A., *The Chemistry of Imperfect Crystals* (North-Holland Publishing Company, Amsterdam, 1964).

[Lu07]   Lu, W., I. Belharouak, J. Liu, and K. Amine, "Electrochemical and Thermal Investigation of $Li_{4/3}Ti_{5/3}O_4$ spinel," Journal of the Electrochemical Society **154**[2] A114 - A118 (2007).

[Mik80]   Mikkelsen, J. C. Jr., "Pseudobinary Phase Relations of $Li_2Ti_3O_7$," Journal of the American Ceramic Society **63** [5-6] 331-335 (1980).

[Mik04]   Mikhaylik, Y. V. and J. R. Akridge, "Polysulfide Shuttle Study in the Li/S Battery System," Journal of the Electrochemical Society **151** 1969-1976 (2004).

[Mit11]   Mitsubishi Motors Corporation, "What is "I MiEV"?," http://www.mitsubishi-motors.com/special/ev/whatis/index.html (2011).

[Mor79]   Morosin, B. and J. C. Mikkelsen, "Crystal Structure of the Li^+ Ion Conductor Dilithium Trititanate, $Li_2Ti_3O_7$," Acta Crystallographica, Section B (Structural Crystallography and Crystal Chemistry) **B35** 798-800(1979).

[Mor08]   Morales, J., J. Santos-Pena, R. Trocoli, and S. Franger, "Electrochemical Activity of Rock-Salt-Structured $LiFeO_2$ / $Li_{4/3}Ti_{2/3}O_2$ nanocomposites in lithium cells," Journal of Nanoparticle Research **10** 217 - 226 (2008).

[Mou03]   Moulson, A. J. and J. M. Herbert, *Electroceramics: Materials, Properties, Applications*, 2nd ed (Wiley, England, 2003).

[Nak05]   Nakayama, M. and M. Wakihara, "Materials Design for High Lithium Ionic Conductor," Netsu Sokutei **32** [4] 186-194 (2005).

[Nis11]   Nissan North America, Inc, "Nissan LEAF^{TM}," http://www.nissanusa.com/leaf-electric-car/index#/leaf-electric-car/index (2011).

[Ohz95]   Ohzuku, T., A. Ueda, and N. Yamamoto, "Zero-Strain Insertion Material of $Li[Li_{1/3}Ti_{5/3}]O_4$ for Rechargeable Lithium Cells," Journal of the Electrochemical Society **142** [5] 1431-1435 (1995).

[Ogi12]   Ogihara, H., J. Kasemchainan, I. Kerkamm, and U. Eisele, "Eisendotiertes Lithiumtitanate als Kathodenmaterial", Patent DE102012200080, filed on January 4th, 2012.

[Ore09]   Orera, A., M. T. Azcondo, F. Garcia-Alvarado, J. Sanz, I. Sobrados, J. Rodriguez-Carvajal, and U. Amador, "Insight into Ramsdellite $Li_2Ti_3O_7$ and Its Proton-Exchange Derivative," Inorganic Chemistry **48** 7659-7666 (2009).

[Sch97/1]   Scharner, S., *Untersuchungen zur Struktur, Elektrochemie und Farbe von substituirten Lithiumtitanaten für mögliche Anwendungen in der Elektrochromie,* Ph.D Thesis, Technische Fakultät der Christian-Albrechts-Universität zu Kiel (1997).

[Sch97/2]   Scharner, S., W. Weppner, and P. Schmid-Beurmann, "Cation Distribution in Ordered Spinels of the Li_2O-TiO_2-Fe_2O_3 System," Journal of Solid State Chemistry **134** 170-181 (1997).

References

[Sch99]   Scharner, S., W. Weppner, and P. Schmid-Beurmann, "Evidence of Two-Phase Formation upon Lithium Insertion into the $Li_{1.33}Ti_{1.67}O_4$ Spinel," Journal of the Electrochemical Society **146** [3] 857-861 (1999).

[Scr10]   Scrosati, B. and J. Garche, "Lithium Batteries: Status, Prospects and Future," Journal of Power Sources **195** 2419 - 2430 (2010).

[Sha76]   Shannon, R. D., "Revised Effective Ionic Radii and Systematic Studies of Interatomic Distances in Halides and Chalcogenides," Acta Crystallographica A **32** 751-767 (1976).

[Sic99]   Sickafus, K. E., J. M. Wills, and N. W. Grimes, "Structure of Spinel," Journal of the American Ceramic Society 82 [12] 3279-3292 (1999).

[Sio10]   Sion Power Corporation, "Sion Power Recieves ARPA-E Grant to Develop Batteries for Electric Vehicles," http://sionpower.com/pdf/articles/ARPA-E%20Grant%20Press%20Release.04-30-2010.pdf (2010).

[Sio11]   Sion Power Coroperation, "Technology Overview," http://www.sionpower.com/technology.html (2011).

[Smy00]   Smyth, D.M, *The Defect Chemistry of Metal Oxides* (Oxford University Press, New York, 2000).

[Sol03]   Solymer, L. and D. Walsh, *Electrical Properties of Materials* (Oxford University Press, New York, 2003).

[Ste93]   Steiner, H.J., P. H. Middleton, and B. C. H. Steele, "Ternary Titanates as Anode Materials for Solid Oxide Fuel Cells," Journal of Alloys and Compounds **190** 279-285 (1993).

[Tar01]   Tarascon, J. and M. Armand, "Issues and Challenges Facing Rechargeable lithium batteries," Nature **414** 359-67 (2001).

[Tes11]   Tesla motors, Inc. "Roadster," http://www.teslamotors.com/roadster (2011).

[Veg21]   Vegard, L., "Die Konstitution der Mischkristalle und die Raumfullung der Atome," Zeitschrift fur Physik **5** [1] 17-26 (1921).

[Vij09]   Vijayakumar, M., S. Kerisit, Z. Yang, G. L. Graff, J. Liu, J. A. Sears, S. D. Burton, K. M. Rosso, and J. Hu, "Combined ^{6,7}Li NMR and Molecular Dynamics Study of Li Diffusion in Li_2TiO_3," The Journal of Physical Chemistry C **113** [46] 20108-20116 (2009).

[Vit02]   Vitins, G., G. Kizane, A. Lusis, and J. Tiliks, "Electrical Conductivity Studies in the System Li_2TiO_3-$Li_{1.33}Ti_{1.67}O_4$," Journal of Solid State Electrochemistry **6** 311-319 (2002).

[Wag06]   Wagemaker, M., D. Simon, E. Kelder, J. Schoonman, C. Ringpfeil, U. Haake, D. Lützenkirchen-Hecht, R. Frahm, and F. Mulder, "A Kinetic Two-Phase and Equilibrium Solid Solution in Spinel $Li_{4+x}Ti_5O_{12}$," Advanced Materials **18** 3169-3173 (2006).

[Wep77]   Weppner, W. and R. A. Huggins, "Determination of the Kinetic Parameters of Mixed-Conducting Electrodes and Application to the System Li_8Sb," Journal of the Electrochemical Society **124** [10] 1569-1578 (1977).

[Whi04]   Whittingham, M. S., "Lithium batteries and cathode materials," Chemical Reviews **104** 4271-4301 (2004).

[Wil07/1]   Wilkening, M., R. Amade, W. Iwaniak, and P. Heitjans, "Ultraslow Li Diffusion in Spinel-type Structured $Li_4Ti_5O_{12}$ - A Comparison of Results from Solid State NMR and Impedance Spectroscopy," Physical Chemistry Chemical Physics **9** 1239-1246 (2007).

References

[Wil07/2]   Wilkening, M., W. Iwaniak, J. Heine, V. Epp, A. Kleinert, M. Behrens, G. Nuspl, W. Bensch, and P. Heitjans, "Microscopic Li Self-Diffusion Parameters in the Lithiated Anode Material $Li_{4+x}Ti_5O_{12}$ $(0 \leq x \leq 3)$ Measured by ^7Li Solid State NMR," Physical Chemistry Chemical Physics **9** 6199-6202 (2007).

[Wol06]   Wolfenstine, J., U. Lee, and J. L. Allen, "Electrical Conductivity and Rate-Capability of $Li_4Ti_5O_{12}$ as a Function of Heat-Treatment Atmosphere," Journal of Power Sources **154** 287-289 (2006).

[Wol08]   Wolfenstine, J. and J. L. Allen, "Electrical Conductivity and Charge Compensation in Ta doped $Li_4Ti_5O_{12}$," Journal of Power Sources **180** 582-585 (2008).

[Yi10]   Yi, T., L. Jiang, J. Shu, C. Yue, R. Zhu, and H. Qiao, "Recent Development and Application of $Li_4Ti_5O_{12}$ as Anode Material of Lithium Ion Battery," Journal of Physics and Chemistry of Solids **71** 1236-1242 (2010).

[Yos09]   Yoshio, M., R. J. Brodd, A. Kozawa, Eds., *Lithium-Ion Batteries - Science and Technologies* (Springer, New York, 2009)